Photonic crystal-adaptive optical devices

Buss, Thomas; Kristensen, Anders; Smith, Cameron

Publication date:
2013

Document Version
Publisher's PDF, also known as Version of record

DTU Nanotech
Department of Micro- and Nanotechnology

Ph.D. Thesis

Photonic crystal-adaptive optical devices

Thomas Buß

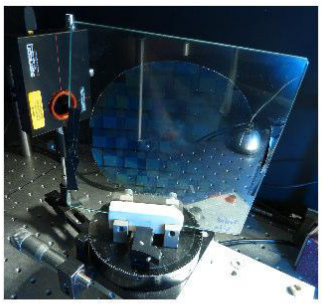
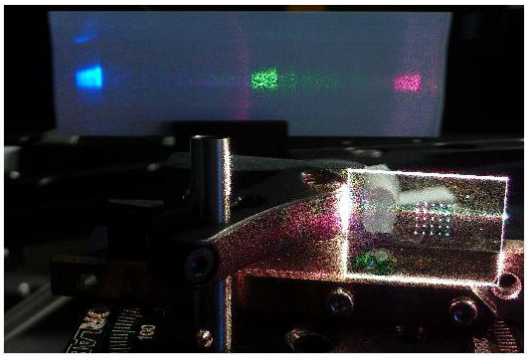
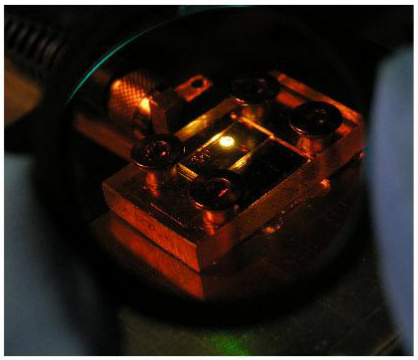
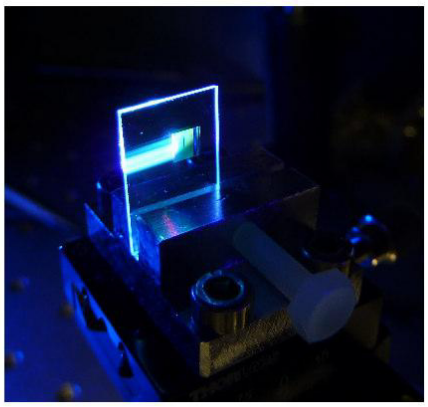

Supervisor: Anders Kristensen
Co-supervisor: Cameron L. C. Smith

Department of Micro- and Nanotechnology
Technical University of Denmark

November 14th, 2012

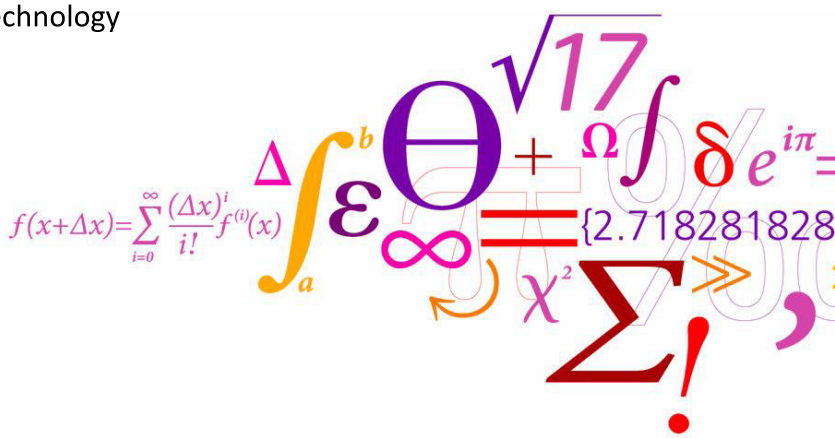

Abstract

This Ph.D. thesis presents methods for enhancing the optical functionality of transparent glass panes by introduction of invisible nanoscale surface structures, such as gratings and planar photonic crystals. In this way the primary functionality of the glass - transparency - may be enhanced with new properties, turning window glasses or glass surfaces of hand-held electronics into multifunctional devices. Common to all examples discussed, gratings and photonic crystals are used to engineer the optical dispersion and selectively modify the direction of guided light and transfer free-space light into guided modes and vice-versa. This is done in a way such that the interaction of guided light inside the glass and transmitted light through the glass is minimized. The relevant physical background for these processes is discussed and four practical devices which demonstrate the principle have been designed, fabricated and analyzed. First a solar harvesting method, based on nanoscale gratings which are imprinted in a thin-film which is deposited on the window pane is discussed. Free-space light which is incident onto a window is coupled to guided modes in the thin-film or the substrate and guided towards the edge, while transparency of the glass is preserved. Solar cells could be attached to the edges to generate electricity. More complex structures than single-period gratings are investigated in gratings used for daylighting, i.e. optimizing the way how natural sunlight is transmitted through windows into the room. It is shown that gratings with disorder introduced to the period effectively modify the diffraction characteristics from distinct sharp and wavelength dependent orders into a broad distributions over large angular range and with sufficient mixing such that color effects are minimized, thus allowing a homogeneous, glare-free, white-light daylighting into the room.Even more functionality can be achieved when the optical effects are tunable or reconfigurable. This is investigated with photonic crystal dye lasers. These lasers combine a photonic crystal resonator with a dye-doped liquid crystal gain medium for the realization of cheap and compact optically pumped, electrically tunable lasers. Finally, a transparent projection display is presented which uses sub-wavelength gratings for redirection of light guided inside a waveguide and facilitates electro-optic switching by means of liquid crystals. The study presents a working proof-of-principle for a transparent projection display and furthermore allows for a detailed study of the interaction between guided light and the voltage-dependent molecular alignment of liquid crystal molecules.The influence of TE/TM polarization is investigated and switching times and driving voltages are competitive with existing non-projection liquid crystal displays. The principle has been investigated for use in projection displays but may also be applied to other applications such as cell manipulation in lab-on-a-chip systems and reconfigurable optical switches in multilayer photonic circuits and optical interconnects.

Resumé (Danish abstract)

Denne Ph.D.-afhandling præsenterer metoder til at forbedre den optiske funktionalitet af gennemsigtige ruder ved introduktion af usynlige overfladestrukturer i nano-størrelse, såsom optiske gitre og fotoniske krystaller. På denne måde kan den primære funktionalitet af glasset - gennemsigtighed - forøges med nye egenskaber og omdanner vinduesruder eller glasoverflader på håndholdte elektroniske apparater til multifunktionelle anordninger. Fælles for alle diskuterede eksempler er at optiske gitre og fotoniske krystaller benyttes til at ændre den optiske dispersion, og selektivt modificere retningen af guidet lys, samt at overføre free-space lys til guidede tilstande og omvendt. Dette gøres på en sådan måde, at interaktionen af guidet lys inde i glasset og transmitteret lys gennem glasset minimeres. Den relevante fysiske baggrund for disse processer diskuteres og fire praktiske anordninger, som viser princippet er blevet designet, fabrikeret og analyseret. Først diskuteres en solfanger-metode, baseret på nanoskala gitre, der er præget i en tynd-film, som er deponeret på vinduesruden. Sollys, som er indfaldene på et vindue kobles til en optisk bølgeleder i en tyndfilm eller i substratet og ledes ud mod kanten, mens gennemsigtigheden af glasset bevares. Solceller kan sluttes til kanterne for at generere elektricitet. Mere komplekse strukturer end enkelt-periodiske gitre er undersøgt i form af gitre der kan anvendes til en bedre fordeling af dagslyset inde i bygninger, ved at optimere den måde hvormed naturligt sollys skinner gennem vinduerne ind i bygningens lokaler. Det bliver vist, at gitre med uorden i gitterets periode effektivt kan modificere diffraktions-egenskaber, fra skarpe og bølgelængdeafhængige ordner, til en bred fordeling over et stort vinkelområde og med tilstrækkelig blanding til at farveeffekter minimeres og et homogent, blændfrit, hvidt dagslys skinner ind i lokalet. Endnu mere funktionalitet kan opnås, når de optiske effekter kan tunes eller er omkonfigurérbare. Dette undersøges med farvestoflasere, baseret på fotoniske krystaller. Disse lasere kombinerer fotoniske krystal-resonatorer med et gain-medium af farvestofdotterede flydende krystaller, til at fremstille billige, kompakte, optisk pumpede og elektrisk justerbare lasere. Endelig præsenteres et transparent projektions-apparat, som anvender sub-bølgelængde gitre til omdirigering af lys som ledes inde i en bølgeleder. Elektro-optisk udkobling på definerede positioner realiseres ved hjælp af flydende krystaller. Undersøgelsen viser et proof-of-principle for et transparent projektions-display og tillader endvidere et detaljeret studie af interaktionen mellem guidet lys og en spændingsafhængig rotation af flydende krystal-molekyler. Indflydelsen fra TE / TM polarisering undersøges og reaktionstid og tærskelspænding er på samme niveau som eksisterende flydende krystal-displays. Princippet er blevet undersøgt til brug i projektionsskærme, men kan også anvendes til andre applikationer såsom cellemanipulation i lab-on-a-chip systemer og omkonfigurerbare optiske kopler i flerlags fotoniske kredsløb og optiske interconnects.

Preface

This thesis is submitted in partial fulfillment of the requirements for obtaining the Philosophiae Doctor (Ph.D.) degree at the Technical University of Denmark (DTU). The work presented here has been carried out from November 15^{th}, 2009 until November 14^{th}, 2012 at the Department of Micro- and Nanotechnology in the Optofluidics research group and in the DTU Danchip cleanroom. The project was supervised by Prof. Anders Kristensen whom I thank for his continuous support and invaluable advice during the last years. Furthermore, I gratefully thank my co-supervisor, Postdoc Cameron L. C. Smith, for the many good meetings, fruitful discussions and the nice time working together. In particular, I acknowledge the effort of supervising my work even while he has been at the most remote places of the planet (i.e. in Australia and in Jylland).

I also enjoyed the very good working environment in the Optofluidics group, and working with the many nice people with their very diverse competences and expertise. This also includes the former group members Mads Brøkner Christiansen and Morten Bo Mikkelsen who taught me cleanroom fabrication of dye lasers, skiing, sol-gel processing, principles of daylighting and sailing (with variable success). I also thank the staff in the Danchip cleanroom for maintaining a fantastic facility and for support and training on the machines, in particular Peixiong Shi who was always ready to start an e-beam exposure. This reminds me that I should thank Anders not only for his scientific advice, but also for his efforts to make sure that we have funding available to work with this type of world-class equipment.

I gratefully acknowledge the funding of my Ph.D. project from the EC project NaPaNIL (Contract No. 214249) and the financial support from the Otto Mønsteds Fond, the Incubic/Milton Chang Travel Award and the Ing. Alexandre Haynman og Hustru Nina Haynmans Fond which allowed me to present my work at various international conferences.

I also thank DTU, the state and the people of Denmark who have warmly welcomed me here five years ago. Finally, I thank my family and my girlfriend Anne for her support, especially during the last months of thesis writing. Without you, this work would not have been possible.

Thomas Buß

November 14th, 2012

Contents

List of abbreviations

Abbreviation	Meaning
AFM	Atomic Force Microscope
CCD	Charge coupled device
DFB	Distributed Feedback
EBL	E-beam lithography
FWHM	Full Width at Half Maximum
ITO	Indium Tin Oxide
LC	Liquid crystal
MPB	MIT Photonic Bands
NIL	Nano-Imprint Lithography
PhC	Photonic Crystal
RIE	Reactive Ion Etch
SEM	Scanning Electron Microscope
TEC	Thermo-electric cooler
TIR	Total internal reflection
TIR	Total internal reflection
TE	Transverse Electric
TM	Transverse Magnetic
UV	Ultra-Violet
YAG	Yttrium Aluminum Garnet

List of symbols

Symbol	Meaning
n	refractive index
n_{eff}	effective refractive index
$\vec{n}$	liquid crystal director
Λ	Grating period
λ	wavelength
m	Diffraction order
M	Grating disorder (periods)
ξ	Grating disorder (percentage)
θ	beam angle
θ_{in}	incident beam angle
θ_{out}	outgoing beam angle
η	Efficiency
η_{redir}	Redirection efficiency
V_{th}	Threshold voltage
t_{rise}	Signal rise time
t_{fall}	Signal fall time

1 Introduction

This thesis is based on the hypothesis that the optical functionality of windows and other glass panes can be enhanced beyond simple transparency by use of optically functional nanostructures. The application of sub-wavelength gratings and photonic crystals allows the creation of complex photonic systems inside or on top of the glass surface, based on guiding and redirection of light. If these photonic systems are combined with transparent electronics, new functionality can be envisioned with wide-ranging possibilities: Even simple systems, like window panes with tunable gratings could perform complex tasks like controlling the amount and direction of sunlight which enters a room - adjustable to the current position of the sun and personal preferences of the users. By additional integration of external laser light sources even more advanced functions are possible. Projection displays could be integrated into *any* transparent object, ranging from window panes to small hand-held electronic devices where the projected image size can by far extend the size of the device itself. In this regard, projectors could be integrated into the front glass of mobile phones, without distracting the view onto the typical display and without increasing of device dimensions.

In order to investigate the feasibility of this hypothesis, this thesis discusses the relevant physical background, technological requirements and limitations. In this context it is investigated which optical functionality can be achieved with nanostructures and a special focus is put on *transparent* devices made of glass or polymers. A drawback of the omnipresence of electronic devices is the increased global energy consumption, reaching 19 PWh and CO_2 emissions of 29.8 billion tons in 2009.[1] Therefore methods for reduction of energy consumption and generation of electricity from renewable sources like solar energy are important to decelerate global warning and also to enable electricity-autonomous devices. Two such methods - based on nanostructured glasses - are discussed. The fabrication of sub-wavelength structures is done by means of nanoimprint, such that there is a realistic opportunity for high volume, cost-effective production of the devices.

In order to present the concept of transparent and adaptive optical devices, four examples of increasing complexity have been realized, all with the common properties that light is guided and redirected inside an otherwise transparent device. The following figure presents the outline of the presentation of these devices in this thesis:

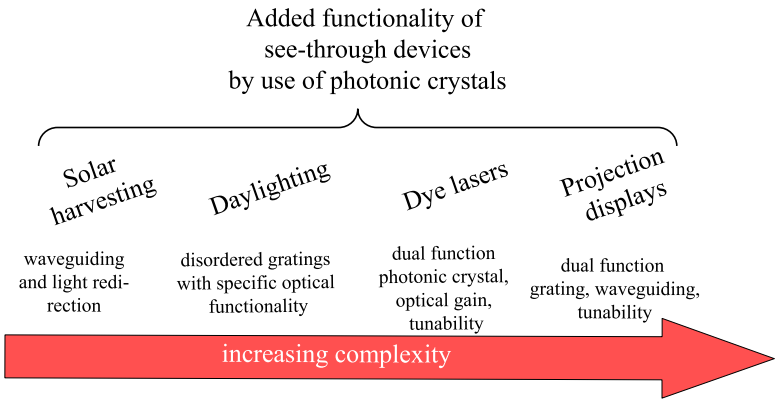

First, a non-tunable, single-period grating for solar harvesting applications is discussed. As a next step, more complex gratings with multiple superimposed and disordered periods are investigated for optimized light transmission through daylighting windows. The next level of complexity is a photonic crystal dye laser, where liquid crystals are used to tune the laser wavelength. Finally a transparent projection display, based on light guided in the glass and locally outcoupled by means of liquid crystal-actuated gratings is presented.
In order provide the context for development and improvement of these systems, an overview of already existing systems with their strengths and limitations, is given in the following.

1.1 Building integrated solar harvesting

In the recent years extensive research has been conducted to harvest sunlight for the generation of electricity. Silicon solar cells are widely used but large areas are required for reasonable total power generation, resulting in high costs and the requirement for large sunlight-exposed areas. Thin-film solar cells[2] and organic solar cells[3] offer lower costs per Watt but require even larger areas due to lower efficiencies. Another alternative is the use of solar concentrators which collect sunlight on large areas and focus the light onto smaller, high efficiency solar cells.[4] These concentrators are bulky constructions with metallic mirrors and mainly used in large area solar parks at remote places. It is however much more attractive to generate the electricity directly at the point of use and alternative areas for solar harvesting are building façades. These provide large areas which are exposed to sunlight but typically not used for solar harvesting. In the ideal case, solar harvesting devices could be incorporated into the façade without changing the architectural design of the building and without perturbing vision through the windows. Especially in areas where buildings heat up significantly during summer, such that climatisation is required, solar harvesting may reduce the energy consumption considerably. Some approaches exist to use these huge areas which are potentially available for solar harvesting and a few shall be presented in the following.

One example is the main train station in Berlin, Berlin Hauptbahnhof. Here solar cells are placed on the glass roof with a coverage of around 50%, see figure 1.1(a). The electricity generation is about 160 MWh per year.[5] Another example is the use of polymer solar cells[3] are cheaper to fabricate and both absorption bands and thickness may be chosen such that the foil is translucent. One drawback, however, is that the transmittance is low and red-colored as shown in fig. 1.1(b). A third example of building-integrated photovoltaics is the Co-operative Insurance Tower (CIS Tower) in Manchester, shown in figure 1.1(c) (left tower). The façades of the service tower are covered by standard non-transparent silicon solar cells, providing real-life electricity generation values of *vertically mounted* solar cells. The building uses 4898 modules, specified for 80 W electricity generation under ideal conditions (total 391 kW). Due to the typically cloudy weather in Manchester, the average electricity production is only 21 kW or 183 MWh per year.[6]

A forth method has been presented by the company Pythagoras Solar, which uses

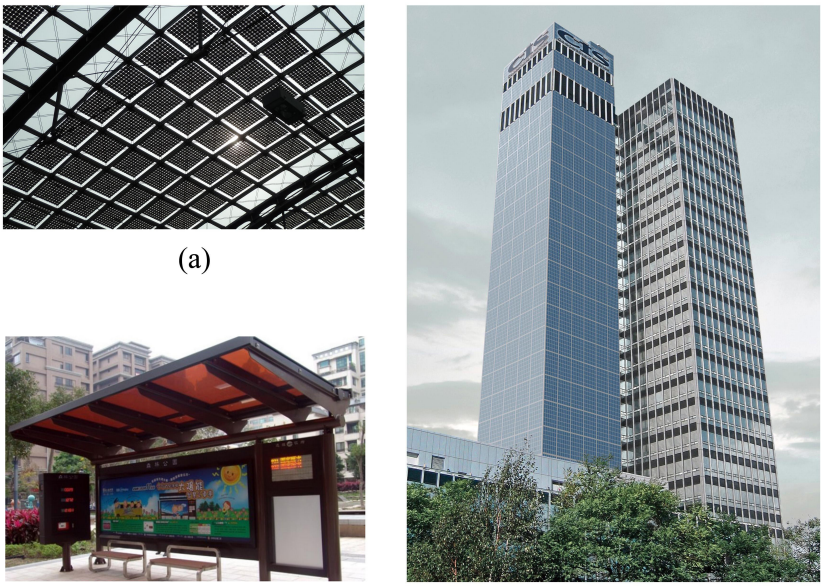

Figure 1.1: Solar cells integrated into buildings. (a) Silicon solar cells on the roof allow partial transmission of light. (b) Translucent polymer solar cells on the roof of a bus stop. Figure from ref.[7] (c) The left tower, support tower to the actual building, is covered with (non-transparent) silicon solar cells. Figure from ref.[8]

.

many thin stripes of solar cells, directly horizontally integrated into a window pane, combined with optical elements which redirect light onto the cells. To the best of the author's knowledge no peer-reviewed articles exist about this technology. Figure 1.2 shows a drawing of the principle and a photograph of a demonstration window. Clearly, the integrated solar cells cause significant distortion of the view through the window. Furthermore the concept appears to be

difficult to manufacture. These examples demonstrate that solar cells mounted on

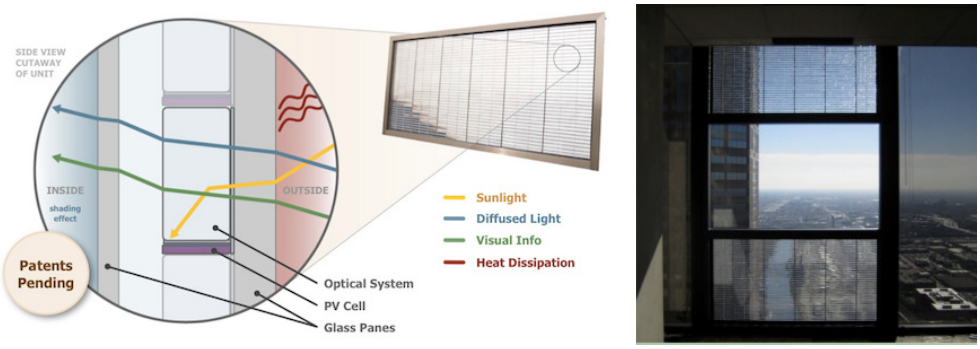

(a) (b)

Figure 1.2: Window integrated solar cells by Pythagoras Solar. Figures from ref.[9] (a) Drawing of operation principle. (b) Photograph of demonstration unit. The solar cells are integrated into the upper and lower part of the window.

building façades may be beneficial, even in non-optimum conditions like cloudy weather and the fact that the orientation of the solar cells can not be oriented towards the sun. Many of today's office buildings have a majority of their facades covered with windows and a method to generate electricity from these areas would be beneficial. One way to harvest solar energy from window panes are luminescent solar concentrators.[10] In these systems luminescent dyes are implanted into the glass which absorb light and isotropically re-emit Stokes-shifted light, see fig. 1.3(a). A fraction of the re-emitted light will be guided inside the glass due to total internal reflection and solar cells which are placed at the side of the pane convert generate electricity. The reported redirection efficiency (light guided to the edge / incident light) is 5.2%. Tunability of such systems is feasible if anisotropic dyes are combined with liquid crystals in a guest-host scheme.[11] The transparency

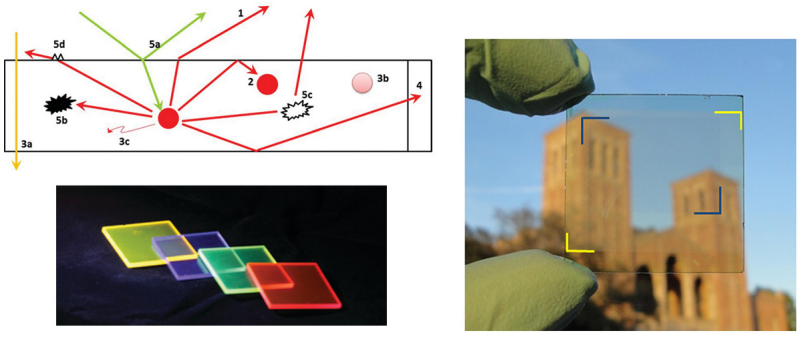

(a) (b)

Figure 1.3: (a) Photograph of luminescent solar concentrator and a drawing of light paths and loss mechanisms. Figure from ref.[12] (b) A polymer solar cell, optimized for IR light absorption and visible light transparency. Figure from ref.[13]

of polymer solar cells can be improved by combining materials which absorb near infrared light but are transparent to visible light, together with transparent silver nano-wire electrodes. A demonstration of such a sample is shown in fig. 1.3(b). The maximum transmission is 66% at 550 nm and the power conversion efficiency amounts to 4%.
In addition to building integrated solar cells, transparent solar cells may also be useful at a much smaller scale, such as in portable electronic devices. While this has been used for many years for watches, modern electronics like mobile phones or cameras rarely use solar cells. Only a few devices exists and some are shown in figure 1.4. The mobile phone and laptop both use the backside for the solar cell, but with solar harvesters as described above also the screen area could be used. For digital cameras the screen area is typically the only free area which is available. Some of these devices like cameras and mobile phones are only used actively a few minutes per day and could replenish their batteries during the rest of the time when they are exposed to daylight.

In the course of this thesis it is investigated if and how nanoscale gratings and

(a) (b) (c) (d)

Figure 1.4: Consumer electronics with integrated solar cells. Images from refs.[14–17] (a) Wrist watch with solar cells integrated into the dial. (b) Mobile phone with solar cell battery cover. (c) Notebook computer with solar cells on the cover. (d) Digital camera *without* solar cells. The only feasible area for solar harvesting is the display.

photonic crystals, which redirect incident sunlight into the window pane can be used as an alternative solar concentration technique. In this case, light is guided by total internal reflection inside the glass pane towards the edge where high efficiency solar cells may be installed. Possible advantages are low cost, high transparency, no distortion or coloration of the glass and no modification of the architectural design required. Similar investigations were done by de Jong *et al.* (2011,[18]), see fig. 1.5, but not characterized in terms of redirection efficiency and without discussion of the transparency. In this thesis a special focus is put on maintaining the transparency of the window. De Jong *et al.* use periods of 590 nm in their investigation, which is significantly larger than the period used for gratings in this thesis (355 nm), possibly causing the gratings to be visible to the naked eye under certain conditions.

Using surface grating couplers for solar harvesters also has the possibility for tuning the effect, which is important for two reasons. First, when the weather is cloudy and light is redirected to the side, this light is lost for lighting

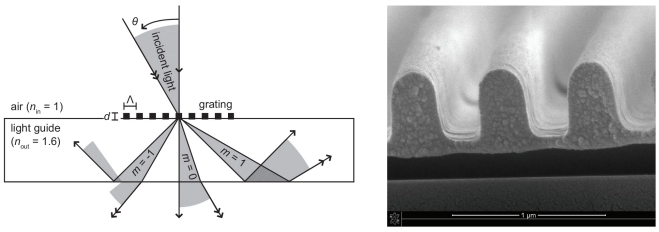

(a) (b)

Figure 1.5: Grating couplers for solar concentrators. Figures from ref.[18] (a) Drawing of the device. (b) SEM image of the holographically fabricated grating with period of 590 nm.

inside the room and electrical lights need to be switched on. Due to non-unity efficiency of solar cells, electrical transformation and light bulbs, additional energy consumption is thereby required. In order to circumvent this, window-integrated solar harvesters must be tunable, i.e. it must be possible to switch them off in cloudy weather conditions, and make the window fully transparent. This would be feasible with the devices presented in this thesis. The second reason is of psychological type: people are used to clear windows and acceptance for colored, opaque, iridescent or otherwise distracting windows is likely to be low.

1.2 Daylighting through windows

In addition to generation of electricity from renewable energy sources like solar power, the reduction of energy consumption is a primary countermeasure against global warming. One of the recent efforts in this regard is the phase-out of incandescent light bulbs in the European Union[19] and similar planned or established laws in a number of other countries.[20] However, the most common replacement, fluorescent light bulbs, suffer from low acceptance among customers.[21] An alternative way to reduce the electricity consumption is to make use of light which is ubiquitously available - natural sunlight. The technique to use sunlight for interior lighting is called daylighting[22] and apart from the fact that sunlight generates neither cost nor carbon emission, there are a number of additional advantages. Sunlight is perceived as comfortable illumination[23] and also supports the human circadian rhythm.[24] Of course sunlight may not always be available such that additional lighting is required during morning and evening hours, but often there is actually more sunlight available than is used for interior lighting. The problem is illustrated in figure 1.6(a)-(b) which shows the typical situation in an office at DTU Nanotech. Clearly, there is plenty of sunlight available, which is however blocked by the blinds in order to reduce glare into the room. Consequently, electrical lighting is used to achieve sufficient illumination. Figure 1.6(c) depicts the same situation on the south-facing façade of the DTU Photonics building with the majority of the blinds being closed and probably electrical lighting used inside. These few examples show that in order

(a) (b) (c)

Figure 1.6: (a) Photograph of a typical office at DTU during daytime with lights off. Blinds are closed to block glare onto computer screens. (b) Because the sunlight is too bright, electrical lighting has to be used. (c) A photograph of the south façade of the DTU Photonics building, taken on March 21st. Most of the blinds are closed and probably electrical lighting is used inside. All windows seen belong to offices.

to make viable use of daylighting to reduce energy consumption, it is necessary to reduce the disturbing glare.[25] Such daylighting functionality can be obtained in many different ways,[26] but for practical and architectural reasons, it is convenient to integrate the functionality directly on the glass of the window. A simple solution to would be to make the window diffusely scattering. In this way glare is effectively reduced, but illumination close to the window will be much brighter than further inside the room. The requirement for the ideal daylighting system is therefore a glare-free, homogeneous illumination of the room with a spectrum that resembles the sun. This may be achieved by directing part of the transmitted light towards the ceiling where it may undergo diffuse scattering for illumination of the whole room. This concept is shown in figure 1.7. On the other hand, clear vision through

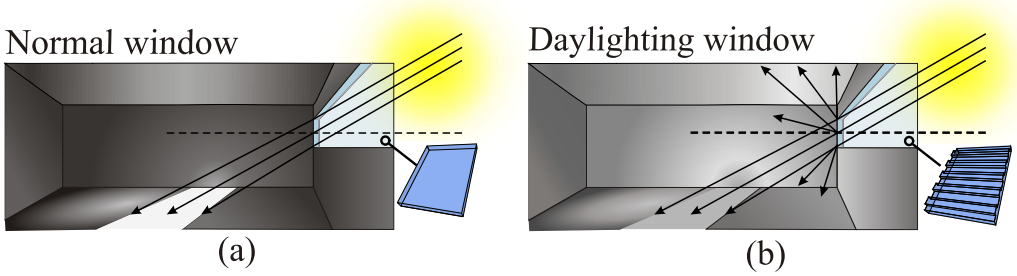

Figure 1.7: (a) Illustration of light distribution inside a room with regular, unstructured windows. (b) Daylighting windows comprising optical light redirection structures on the window pane cause the light to spread more homogeneously throughout the room and towards the ceiling. Figure adapted from.[27]

a window is a major comfort factor,[23] such that many of the existing daylighting systems,[26] which rely on macroscopic optical elements, are not a preferred method. Figure 1.8 shows a demonstration of such a system,[28] which effectively redirects the light but inhibits vision to the outside. Daylighting windows which are optically

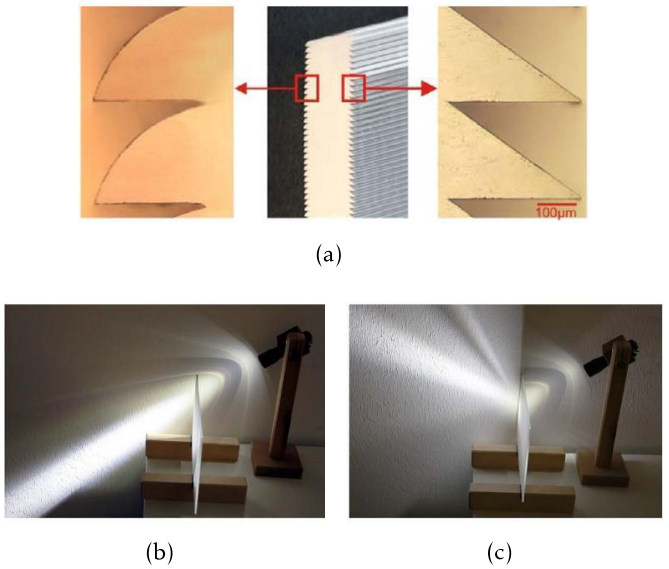

(a)

(b) (c)

Figure 1.8: A daylighting window based on sub-millimeter scale prisms and curved surfaces. The system achieves redirection without color effects, but inhibits vision through the window. Figures from ref.[28] (a) Photograph and micrograph of the optical element. (b) Experiment without optical element in the light path. (c) Experiment with optical element in the light path, redirection of light upwards is observed.

transparent need to be based on microscopic structures and a number of reports of gratings used for daylighting exist.[29,30] The use of diffractive gratings leads however to another problem: diffraction causes separation of the colors when light passes through the window, causing a "rainbow" effect. Some investigations with gratings of different periods have been conducted in the aforementioned reports, however, the results are only vaguely documented. Another method to reduce color dispersion is the introduction of disorder into the grating periods. In this thesis such sub-micron scale gratings, with various degrees of disorder, fabricated by nanoimprint lithography directly on glass panes are investigated and are shown to provide a favorable combination of transparency, reduction of color dispersion, simplicity and daylighting efficiency.

1.3 Tunable microchip dye lasers

Lab-on-a-chip systems[31,32] are miniaturized analysis systems which have recently gained wide-ranging scientific attention. An imaginary lab-on-a-chip system is shown in figure 1.9, comprising fluid supply systems and various analysis methods.

Optofluidic lasers[33,34] are promising devices for affordable integration of light sources in such systems and often it is desirable to have a means of tuning the laser wavelength for optical sensing applications, either to compensate variations of the wavelength or to scan the wavelength over a broad range and monitor the response of the sample. One requirement for such lasers is the feasibility of fabrication by micro- and nanotechnology processes and minimal size. There are

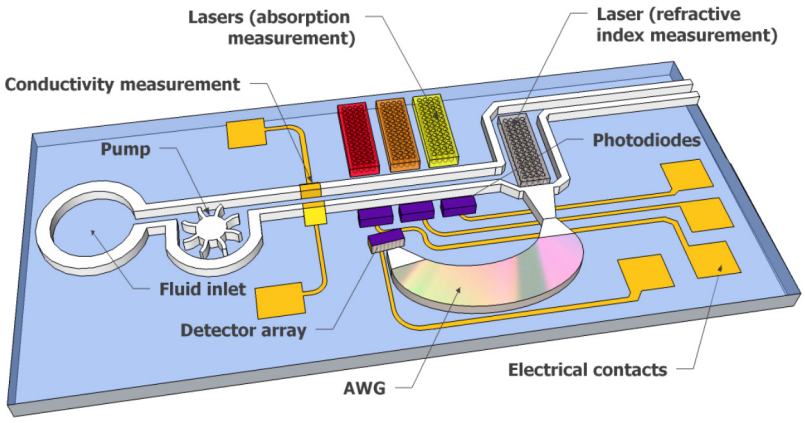

Figure 1.9: An imaginary lab-on-a-chip system, drawn by the author.

several demonstrations of tuning microfluidic dye lasers by means of changing the dye concentration[35] or mixing different dyes.[36] However, these microfluidic systems suffer from complex fluid supply networks and slow time responses. These issues are circumvented by using a more direct, electrical tuning mechanism and one candidate for this are liquid crystals (LCs). LCs provide the largest known electro-optic effect[37] and also the technology is mature in terms of production engineering, being used in most of today's electronic displays. For applications in lasers, dyes may be dissolved in the LC to allow optical gain. One such liquid crystal laser has been presented using holographic excitation to form a DFB cavity,[38] however the pumping scheme with two interfering laser beams needs precise alignment. The wavelength can be tuned from about 600 nm to 630 nm by orientation of the liquid crystal molecules via an applied voltage, see figure 1.10. Note that the laser becomes multimode at larger voltages when the refractive index in the waveguide increases. Instead of an interference-induced DFB cavity, fixed nanostructure are preferred to define a resonator because this simplifies alignment of the laser chip with the pump beam. Such a device, based on an imprinted Bragg grating in a polymer layer has been presented.[39] Figure 1.11 shows a drawing and emission spectra of this laser, which offers a tuning range from 689 to 699 nm. Compared to these 1D periodic resonators, photonic crystals offer much greater control of light by engineering their dispersion in 2 or 3 dimensions.[40] Accordingly, a 2D photonic crystal is used in this thesis for realization of an electrically tunable

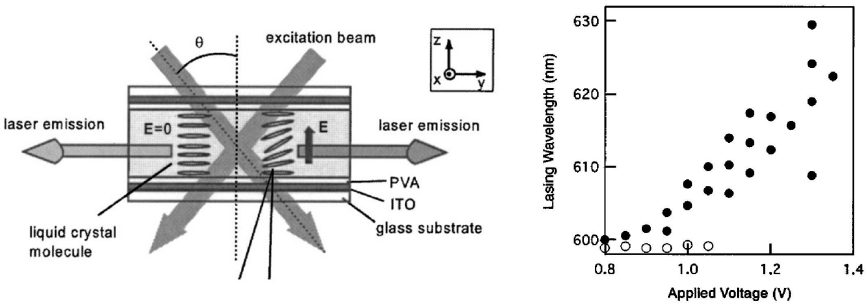

(a) (b)

Figure 1.10: A holographically pumped liquid crystal laser. Figures from ref.[38] (a) Device drawing. (b) Measurement of laser wavelength vs. applied voltage. Open circles indicate a laser mode which is not tuned upon application of a voltage and closed circles mark modes which are shifted by the voltage.

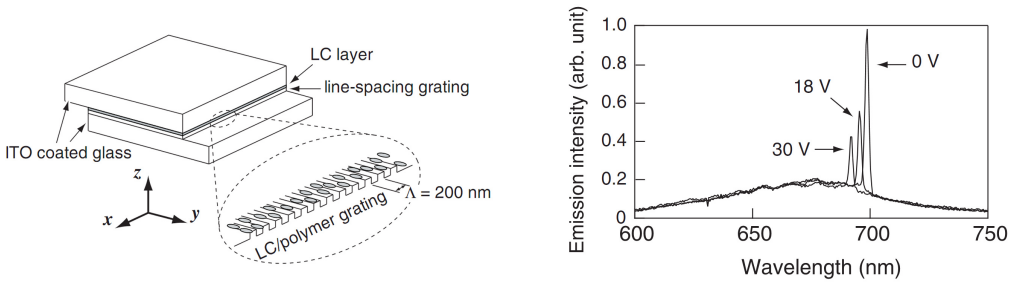

Figure 1.11: A DFB laser using liquid crystals for tuning. Figures from ref.[39]

laser together with a multifunctional photonic crystal resonator.[41] Transparency may be an important feature of lab-on-a-chip systems if a number of internal and external optical sensing methods are implemented.[42] The tunable laser being presented here is transparent, apart from inevitable coloration of the laser dye.

1.4 Transparent projection displays

Today's information-based society has a high demand for display technologies capable of conveying dynamic and interactive data with added functionality. The utility of the human-machine interface must meet progressively challenging requirements for both the adaptation to novel settings and general ease of use. In particular, the increasing prevalence of integrated and embedded electronics has generated a distinct motive for display devices to appear directly and unobtrusively on transparent surfaces to enable a user's seamless acquisition of desired information; i.e. heads-up-displays (HUDs), automotive driver displays and hand-held electronics. To this end, significant research efforts have been performed on transparent electronics,[43] batteries,[44] and loudspeakers.[45]

Transparent displays, based on organic light emitting diodes[46] or polymer dispersed liquid crystals[47] have also been studied in this regard and images of these demonstrations are shown in figure 1.12. However, the miniaturization of

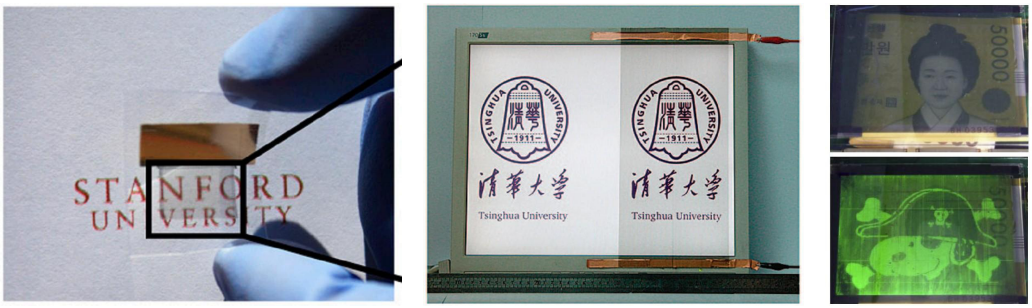

(a) (b) (c)

Figure 1.12: Transparent electronics. Figures from[44–46] (a) Transparent lithium battery. (b) Transparent loudspeaker based on thin carbon nanotube strings. (c) Transparent active matrix organic light emitting diode display.

modern electronics has reached a point where the required display area becomes the limiting factor for further reduction of device dimensions. One way to solve this limitation is via the use of projection displays that occupy a small area on the device and project information onto a larger screen. The aforementioned types of transparent displays do not permit projection without additional optics, which would increase device dimensions and inhibit transparency. Another type, based on an external display and redirection of the image through a series of gratings in a glass plate, has also been presented.[48,49] Such a device is shown in figure 1.13, but the concept requires an external display and does not provide the advantages of coherent laser projection, e.g. the ability to project onto curved surfaces without focusing.

In this thesis a transparent projection display, based on sub-wavelength gratings and liquid crystals is presented, which does not require polarizers or lenses. The sub-wavelength gratings are used for light redirection, i.e. the projection of light guided along the display plane outwards from the device onto a screen. Modulation of the outcoupling process is achieved by means of an applied electric field causing molecular reorientation within a thin liquid crystal (LC) layer that is in contact with the optical grating. As mentioned before, LCs are a mature technology providing the advantages of large electro-optic response, relatively fast switching times, low-cost fabrication and low power consumption.

1.5 Thesis outline

The thesis is structured as follows: First in chapter 2 the relevant theory is presented. Chapter 3 outlines fabrication processes which have been used for making the aforementioned demonstrations of transparent optical waveguiding samples. In order to characterize the devices, an optical setup was designed and

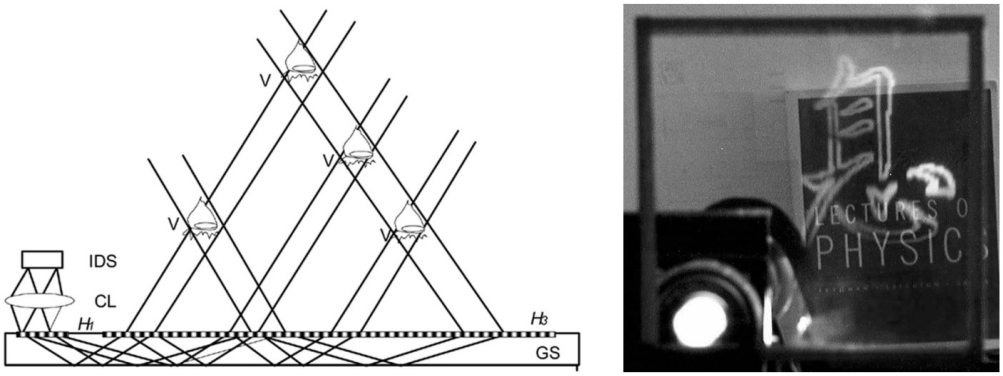

(a) (b)

Figure 1.13: Transparent projection display. Figures from ref.[48] (a) Drawing of beam paths in the device (IDS: input display source, CL: collimating lens, H_1: input coupling grating, H_3: output decoupling grating, GS: glass substrate, V: viewer) (b) Photograph of the projection display. The image of a logo is incoupled at the lower left corner and a projected onto a book in the background.

build, which is documented in 4. Chapters 5 to 8 discuss in detail solar harvesting by nanostructured window panes, daylighting windows based on disordered gratings, tunable dyelasers for lab-on-a-chip applications and finally transparent projection displays. The thesis is concluded with an outlook on possible further research and a summary of the achieved results in chapter 10. Software code and fabrication recipes are collected in the appendix.

2 Theory

2.1 Optical waveguides

Most of the devices presented in this thesis use the principle of optical waveguiding. A waveguide is a geometry which guides light, meaning that the light is confined to a certain region and will ideally travel lossless through that region. Many different kinds of waveguides exist, but here the focus is placed onto planar slab waveguides as shown in figure 2.1. In such a waveguide the light is confined to a core with higher refractive index than its surrounding regions core, surrounded by lower refractive index regions. In many cases for example the core layer is a polymer with highest refractive index of the system n_2, surrounded by air (n_1) and a glass substrate (n_3). In order to analyze devices based on waveguiding, it is important to know the light distribution in the waveguide, and often it is sufficient to consider the approximation of the real waveguide as a one-dimensional slab waveguide (an infinite sheet of high index material surrounded by two lower index materials). This has the advantage that there is an analytical solution for the mode profile, in contrast to the case of a 2D which requires numerical methods to be employed.
In the following the solution for a 1D waveguide is outlined, following the description given in ref.[50] The optical modes of a waveguide are separated into transverse electric (TE) and transverse magnetic (TM) modes and their energy distribution within the waveguide is slightly different. Here TE modes are defined as modes for which the time-averaged electric field varies parallel to the substrate and TM modes with the E-field oscillating perpendicular to the substrate and propagating in the $+z$ direction. Such an electromagnetic wave propagating in a homogeneous medium is described by Maxwell's wave equations:

$$\nabla^2\vec{E} - \frac{n^2}{c^2}\frac{\partial^2}{\partial t^2}\vec{E} = 0$$
$$\nabla^2\vec{H} - \frac{n^2}{c^2}\frac{\partial^2}{\partial t^2}\vec{H} = 0$$

For a TE mode the time-independent wave equation for each of the three regions becomes

$$\frac{\partial^2 H_z^{(1,2,3)}}{\partial x^2} + \left[\left(\frac{\omega n_{1,2,3}}{c}\right)^2 - \beta^2\right] \cdot H_z^{(1,2,3)} = 0$$

The mode profile is obtained by treating the three regions separately and considering that a guided mode must have its energy localized in the center core region. In the cladding the mode must evanescently decay to zero. Finally, the solutions of all three sections must have the same value of the propagation constant

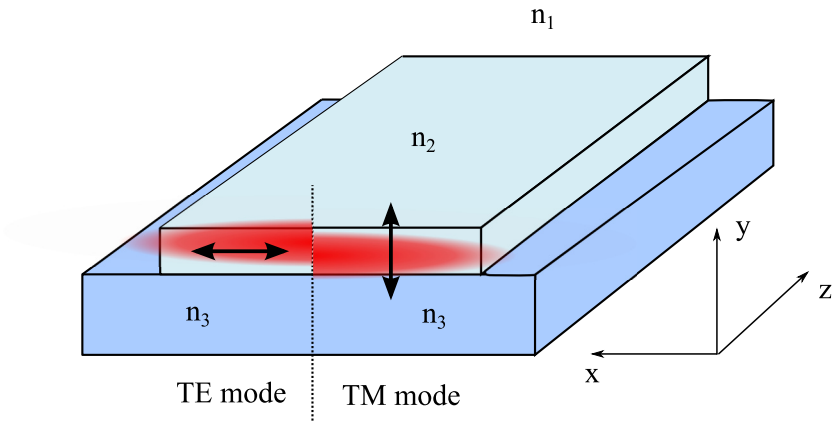

Figure 2.1: Waveguide geometry with TE or TM mode illustrated. The TE mode has larger overlap with the core layer and superstrate, while the TM mode has larger overlap with the substrate. The polarization direction of the E-field is indicated by arrows.

β. The effective refractive index of a mode, given by $\beta \cdot c/\omega$ is unique to each mode and is the analog to the refractive index n, but taking the fact into account that the mode is propagating in a waveguide instead of a bulk material. Therefore n_{eff} does not only depend on the refractive indices of the waveguide layers but also on their thickness and the wavelength. For a guided mode the relation $n_{1,3} < n_{eff} < n_2$ must hold. The solutions to the three sections of the waveguide are given by

$$
\begin{aligned}
H_z^{(1)} &= A_1 \cdot e^{h(x+d/2)} \\
H_z^{(3)} &= B_3 \cdot e^{-h(x-d/2)} \\
H_z^{(2)} &= A_2 \cdot \cos(kx) + B_2 \cdot \sin(kx), k = (\omega n_2/c)^2 - \beta^2
\end{aligned}
$$

where d is the thickness of the slab. By application of boundary conditions (continuity of the field at the interface) the unknown constants can be determined and a transcendental equation is found which allows calculation of the effective refractive indices for the modes (separated for TE and TM modes) at a given wavelength and waveguide thickness. A diagram which plots the effective refractive index of the TE modes vs. waveguide thickness is shown in figure 2.2(a). When using 600 nm light, that example waveguide would be single mode for a thickness smaller than 800 nm. Panel (b) of figure 2.2 shows the normalized power of the guided modes for waveguides of 1 µm and 500 nm thickness. The difference between the effective refractive index of TE and TM modes is usually low, but may still be important for processes which are highly dependent on the effective refractive index or on the overlap of the mode profile with cladding layers.

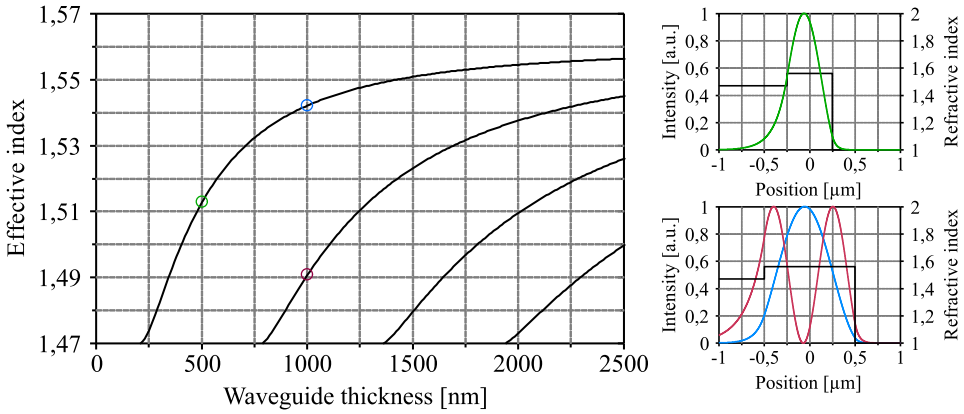

Figure 2.2: Modes of a slab waveguide. Calculated for $n_{cladding} = 1$, $n_{core} = 1.56$, $n_{substrate} = 1.47$ and $\lambda = 600$ nm. (a) TE Mode effective indices as function of thickness for a slab waveguide. (b) Top: mode profile for a 1 µm waveguide. Bottom: The same waveguide reduced to a thickness of 500 nm.

2.2 Photonic crystals

Photonic crystals (PhC) are a generalized concept to describe optical properties of multiple-periodic structures. Figure 2.3 shows photonic crystals of different

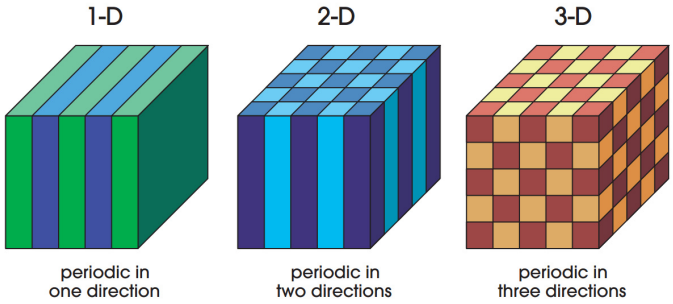

Figure 2.3: Photonic crystals of different dimensions from 1D to 3D. Figure from ref.[40]

dimensionality, starting from a Bragg grating, which is periodic in one dimension, over 2D-periodic structures to 3D crystals. The interaction between light and photonic crystals may, through the periodic structure, be significantly different from that of the bulk material of the PhC. Reference[40] contains a comprehensive overview of the physics of photonic crystals and the following discussion is mainly based on this source. Derivations of equations will be omitted but instead the most remarkable results for the understanding of photonic crystals are presented.
Starting from Maxwell's equations, the "master equation" is derived which describes the magnetic field for a structure with position-dependent dielectric

constant $\varepsilon(\vec{r})$:

$$\nabla \times \left(\frac{1}{\varepsilon(\vec{r})} \nabla \times \vec{H}(\vec{r}) \right) = \frac{\omega^2}{c^2} \cdot \vec{H}(\vec{r}) \tag{2.1}$$

$\vec{H}(\vec{r})$ is the magnetic vector field, ω the frequency and c the speed of light. Once the magnetic field is known, the electric field can then be found by application of

$$\vec{E}(\vec{r}) = \frac{i}{\omega \varepsilon_0 \varepsilon(\vec{r})} \nabla \times \vec{H}(\vec{r}) \tag{2.2}$$

Eqn. 2.1 is actually an eigenvalue equation of the type

$$\hat{\Theta} \vec{H}(\vec{r}) = \frac{\omega^2}{c^2} \vec{H}(\vec{r})$$

where $\hat{\Theta}$ is a linear hermitian operator acting on $\vec{H}(\vec{r})$. This implies that the solutions must be orthogonal. In order to find the solutions, numerical methods are available to solve discretized eigenvalue problems[51] and simulations of this kind will be presented later using geometries from actual devices.
Another practical result is that the master equation is scale-invariant. This means that the solutions are also valid for scaled structures $\varepsilon(\vec{r}) \rightarrow \varepsilon(s \cdot \vec{r})$. Therefore the frequencies of the modes of the master equation are often conveniently expressed relative to c/a where a is the period of a unit cell.
In order to understand the effects in photonic crystals it is required to look at possible solutions to the master equation and the general solution is, according to Bloch's theorem, given by

$$\vec{H}_k(\vec{r}) = e^{i(\vec{k} \cdot \vec{r} - \omega t)} \cdot \vec{u}_k(\vec{r}) \tag{2.3}$$

$$\vec{H}\left(\vec{r}\right) = \sum_k \vec{H}_k\left(\vec{r}\right) \tag{2.4}$$

where $\vec{u}_k(\vec{r})$ is a function with the same periodicity as $\varepsilon(\vec{r})$. One mode is given by a plane waves times the periodic function and the actual field is the superposition of all individual modes. For many cases it is very practical that the solutions obtained in this way are separated into individual modes as this allows to consider only the modes which are relevant to the given application. A mode of the form of eqn. 2.3 is called a Bloch state and due to symmetry it is sufficient to consider only $\varepsilon(\vec{k})$ vectors that lie inside the irreducible Brillouin zone. The Brillouin zone is a unit cell in the reciprocal crystal lattice which is the counterpart to the real lattice in Fourier space. Depending on the symmetries present in the crystal, only the section named the irreducible Brillouin zone is unique in terms of $\vec{k}$ vectors resulting in the same Bloch state.
Figure 2.4 shows an example of a real space lattice in panel (a) and the corresponding reciprocal lattice with the irreducible Brillouin zone highlighted in panel (b). When the frequency is determined for all relevant $\vec{k}$ vectors, the

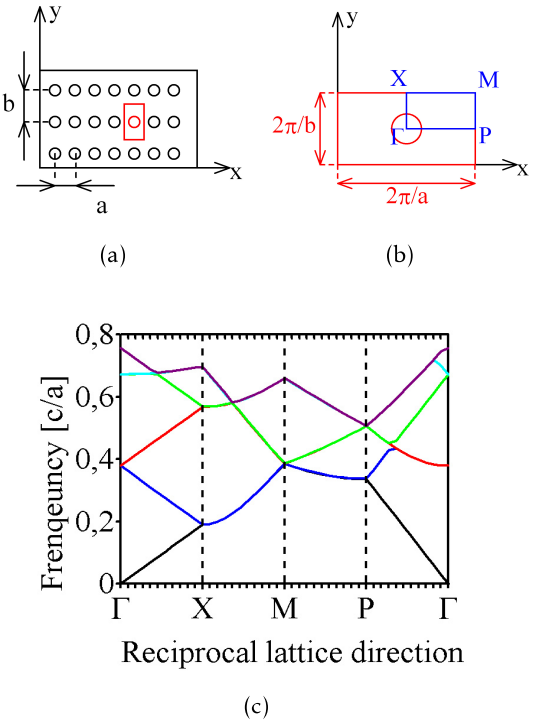

Figure 2.4: (a) Unit cell of a rectangular lattice PhC in real space. (b) The same PhC in reciprocal space with the Brillouin zone marked. (c) Dispersion relation for the PhC in (a).

dispersion relation (also termed the band diagram) of the photonic crystal can be plotted. This describes which frequencies are allowed for a given reciprocal lattice direction. These can then be translated to the properties of practical interest, usually the supported wavelengths for different light propagation directions in the crystal. For a laser also the group velocity of the mode will be important which is given by the slope of the dispersion relation $v_g = \frac{d\omega}{dk}$. An example plot is shown in figure 2.4(c). Each Bloch state leads to a band in the dispersion relation and the five lowest order bands are depicted in the diagram in different colors.
By application of a variational principle it can be shown that the modes have their lowest energy state if they are concentrated in high refractive index areas. This, together with the requirement that higher order modes must be orthogonal to lower order modes, can be used to get an insight into the field distributions in photonic crystals. Figure 2.5 shows the displacement field for the first eight TM bands. As can be seen, the lowest mode concentrates its D-field outside the circles, where the refractive index is higher. The higher order modes must be orthogonal and still try to remain out of the circles which requires solutions of higher frequencies.

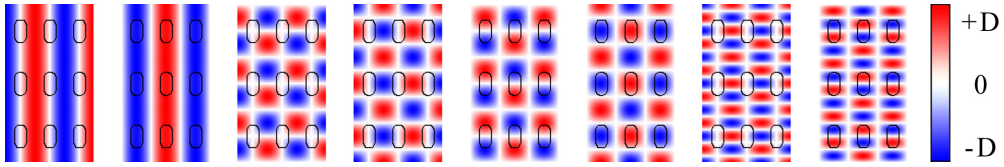

Figure 2.5: Displacement field for the eight first TM bands in a rectangular lattice PhC with circles (holes) of lower refractive index than the surrounding region.

2.2.1 Modelling of photonic crystals

The detailed quantitative analysis of photonic crystals requires the three-dimensional solution of Maxwell's equations. As described in the previous section this can be done by formulation as an eigenvalue problem and here the software program *MIT Photonic Bands* (MPB)[51] is used in order to simulate the dye lasers discussed in chapter 7. The method can be briefly described as formulations of Maxwell's equations as an eigenvalue problem which is then discretized on a finite difference grid and solved using matrix operations to determine the eigenvalue for each mode. From this eigenvalue the corresponding E, H and D field can be constructed. The computational effort can be significantly reduced when the structure has inversion symmetry. In that case only 1/4 of a unit cell needs to be calculated to reconstruct the full field.
Since MPB uses a frequency domain method to solve the eigenvalue equation, only periodic structures can be simulated. Therefore the real finite size photonic crystals slabs are approximated as two-dimensional structures which extend periodically in the plane and infinitely in height. In order to account for the fact that light is confined in the photonic crystal slab like in a waveguide, the refractive index values of the holes and the periphery are modified in the simulation. Instead of using the bulk refractive indices, effective refractive index values of slab waveguides representing the holes and surrounding regions.[52]

2.3 Gratings

Gratings are a special case of the general photonic crystal as a one-dimensional structure. In this thesis only transmission phase gratings are considered, which generate a diffraction pattern in the transmitted light. In most cases it is of interest where diffraction orders are existing for an incident beam. The angles of the diffraction orders are calculated from the relation

$$n_{clad}\frac{2\pi}{\lambda}\cdot\sin(\theta_{in})+m\frac{2\pi}{\Lambda}=n_{grating}\frac{2\pi}{\lambda}\cdot\sin(\theta_{out}). \tag{2.5}$$

Here θ_{in} and θ_{out} are the angles of the incident and out-going beams, m is the diffraction order and n_{clad} and $n_{grating}$ are the refractive indices of the cladding and the grating, respectively. The diffraction efficiency can be calculated analytically only for very simple gratings, and for more complex situations numerical solutions are required. A common technique is the rigorous coupled wave analysis[53] which

solve Maxwell's equations exactly in Fourier space to yield the intensity of reflected and transmitted diffraction orders.

2.4 Modeling of complex photonic systems

Often a photonic device will consists of several of the building blocks described here, e.g. a combination of waveguides, photonic crystals and gratings. In this case modeling of the complete system is not feasible with the methods described above since they are specialized to their particular application, e.g. MPB allows only simulation of periodic structures, unless large supercells are used which result in long simulation times and large memory requirements. A method is required which can simulate the propagation of waves in any structure, which can be achieved with the finite difference in time domain (FDTD) approach.[54] In this thesis this method is used with the MEEP software implementation[55] and is applied to simulate light redirection and guiding by surface grating couplers in chapter 5. The method is based on the discretization of the dielectric structure and the electromagnetic fields on a grid. Maxwell's equations are solved for each grid point and the evolution the fields is calculated as time progresses. The advantage of the method is that there are hardly any limitations on the geometry and the method is very intuitive, since the results can be animated for each time step. However, the resolution of the time steps is linked to the spatial resolution of the grid, such that the simulations are often computationally intensive. Figure 2.6 shows an example of a wave propagating in a waveguide, simulated for two different thicknesses of 250 nm and 1 µm. The thin waveguide is single-moded and the thicker waveguide is multi-moded. One limitation of this method is that it does not yield information about the individual modes which comprise the simulated field. Furthermore it is often a problem that the source also radiates light outside the desired direction, which may interfere with the actual signal. This problem can however typically be avoided by increasing the simulation domain and by using attenuating dummy structures.

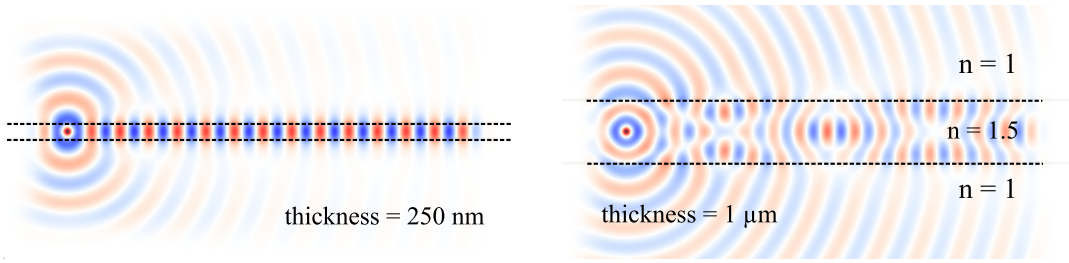

Figure 2.6: Simulation of a a TE mode propagation in a waveguide. The colors indicate the amplitude of the electric field (red: positive, blue: negative) at a certain instant in time. The free-space wavelength is 600 nm.

2.5 Liquid crystals

Liquid crystals (LC) are a phase of matter with properties intermediate between solid crystals with perfect order and isotropic disordered fluids. There are two different classes of liquid crystals, discotic LCs where the degree of crystalinity depends on the concentration and nematic LCs where the degree of crystalline properties depends on the temperature. In this thesis only nematic liquid crystals are discussed, the type that is also used in liquid crystal displays.
The word *nematic* originates from Greek and means 'thread', which reflects the long chains that typically occur in nematic liquid crystals. The liquid crystal that is used in this thesis is 4'- Pentyl- biphenyl- 4-carbonitrile, commonly named 5CB. Figure 2.7(a) shows a drawing of three 5CB molecules, also indicating their size, with a length of approximately 18 Å and a length to width ratio of approximately 3-7. The properties of these materials strongly depend on their phase. At low temperature the material is a frozen solid, a phase which is rather impractical as it does not allow any modification or interaction. At higher temperatures, the molecules change to the nematic phase which is characterized by a short range orientational order, but no positional order. At even higher temperatures, in the isotropic phase, the molecules are randomly distributed as in a usual liquid. The ordering of LC molecules in nematic phase and isotropic phase is illustrated in figure 2.7(b)-(c) as a simplified representation, where the molecules are drawn as ellipses. In the nematic phase the local orientation of the molecules is indicated by the director $\vec{n}$. Nematic liquid crystals in bulk form are comprised of randomly

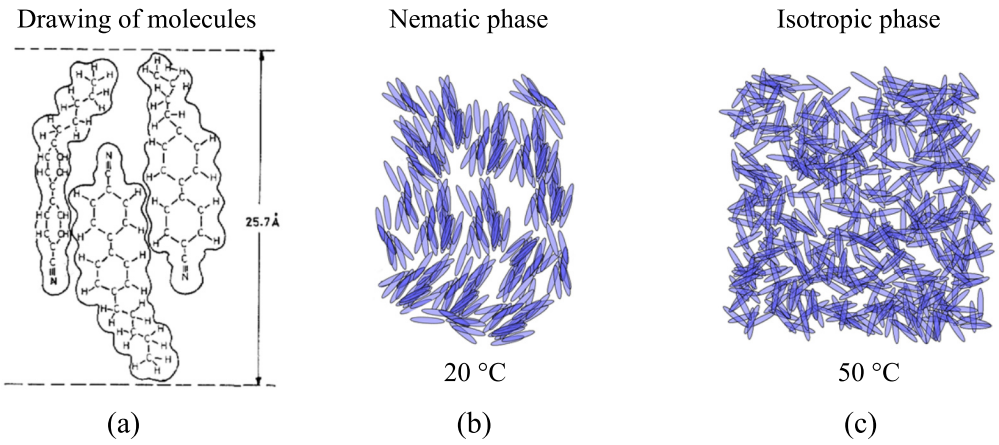

Figure 2.7: (a) Drawing of 5CB liquid crystal molecules (figure from ref.[56]). (b) Liquid crystal molecules in nematic phase, the molecules exhibit a short range orientational order. (c) Molecules in the isotropic phase at elevated temperatures, the molecules show no orientational order and behave like an isotropic liquid.

oriented local domains of ordered crystals and the finite viscosity will not allow re-alignment to lower energy states. However, from a macroscopic point of view the sample is still disordered and the cell appears milky due to scattering of light.

2.5.1 Molecular orientation

Nematic liquid crystals in bulk form appear as a diffusely scattering liquid due to the lack of order over longer ranges. To apply these liquid crystals in optical applications it is required to increase the order to reduce scattering and to exploit the anisotropic properties. This can be achieved by placing the LC between two interfaces which induce ordering, either by topographical structures or by chemical properties.

2.5.1.1 Molecular orientation via surface chemistry

One way to achieve a permanent and homogeneous alignment of the LCs is to modify the surface energy, which causes the molecules to align perpendicular to the surface. Such an alignment, known as homeotropic alignment, can be achieved by deposition of an FDTS (perflourodecyltrichlorosilane) monolayer coating, which has teflon-like properties. The effect of an FDTS coating on different material surfaces is investigated experimentally in figure 2.8. The figure compares the formation of water droplets on coated and untreated surfaces, where the contact angle for Borofloat glass is increased from 46° to 115°, indicating a change of the surface chemistry from hydrophobic to hydrophilic. For SU-8 and PMMA the method is largely effective, but for Ormocore a similar effect as for glass can be achieved. This is explained by the fact that a plasma cleaning step is part of the deposition process, which calcinates a thin surface layer of the Ormocore into porous SiO_2, to which the FDTS molecules can bind. Observation of LC cells fabricated with FDTS coated glass, when placed between crossed polarizers confirms the homeotropic alignment.

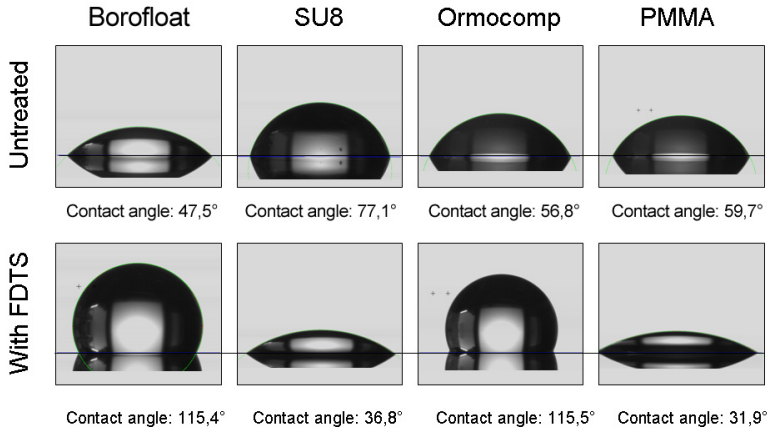

Figure 2.8: Effect of FDTS monolayer deposition on surface chemistry, tested with a water droplet.

2.5.1.2 Molecular orientation via surface topography

In addition to surface chemistry, surface topography may also have a significant influence on the alignment of liquid crystals. This is based on the properties that the molecules are fluid and tend to align themselves in such a way that the total mechanical deformation energy of the molecules is reduced. The lowest energy state corresponds to parallel ordering of the molecules with a homogeneous director orientation throughout the material since any bending of the long molecular chains would increase their energy.
If there is a regular surface topography, such as a grating or scratches on the boundary surface of the liquid crystal cell, the lowest energy state of the molecules is to align parallel to the grooves of the grating. With a layer of nearly perfect alignment at the boundary this also dictates the alignment of the other molecules in the cell. This effect even works if the grooves of the grating are much larger than the dimensions of the molecules.[57] A plot of the anchoring energy of the molecules to a grating structured surface with different grating depths is shown in figure 2.9. However, these alignment layers are fabricated by rubbing a layer of polyamide[58] and it has been argued by other authors that the alignment effect may not be caused by the topography, but instead by reorientation of the polyamide molecules during the rubbing process.[59] As of today, the interdependence of grating dimensions and material onto the LC alignment is not fully investigated. It has however been shown that gratings, embossed by a nanoimprint process, cause alignment of LC molecules, and in such a fabrication process the modification of the polyamide molecules is expected to be less. Imprinted gratings in other materials have also been investigated[60,61] where LC alignment is observed, pointing towards the contribution of surface topography to the alignment.
In order to achieve homeotropic alignment by a surface structure, black silicon

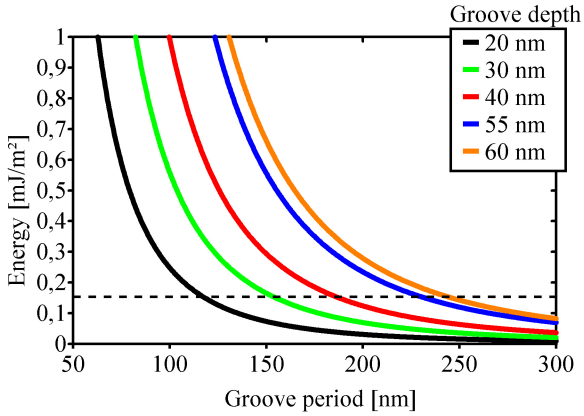

Figure 2.9: Plot of the alignment strength versus alignment grating period for various grating depths. The dashed line indicates an experimentally found value of the anchoring energy that can result in good alignment. Data from ref.[57]

transferred into an Ormocore film is investigated. Black silicon is a surface

structure of sharp spikes which can be created on a silicon wafer by controlling the interplay between etching and passivation in a reactive ion etch process.[62] Since the sharp pyramids effectively cause a gradual increase of the refractive index from 1 (air) to 4 (silicon at visible wavelengths), the Fresnel reflection at the interface is largely inhibited and incident light is absorbed in the bulk. Therefore the material looks black, as opposed to the typical gray-reflective appearance of silicon, hence the name "black silicon". Such a black silicon structure is transformed into Ormocore by a double-replication step. The resulting Ormocore layer is about 50 µm thick and is sandwiched between two FDTS coated glass slides, as shown in figure 2.10 (a). The uncovered section at the left is used as reference. Panel (b) shows the sample between crossed polarizers in the microscope. In the uncovered region the FTDS coated glass leads to a homeotropic alignment and the sample appears black. The Ormocore however does not cause alignment and the disordered crystal domains cause colorful patterns due to interference. This concludes that black silicon shaped nanopatterns are not suitable for alignment of nematic liquid crystals.

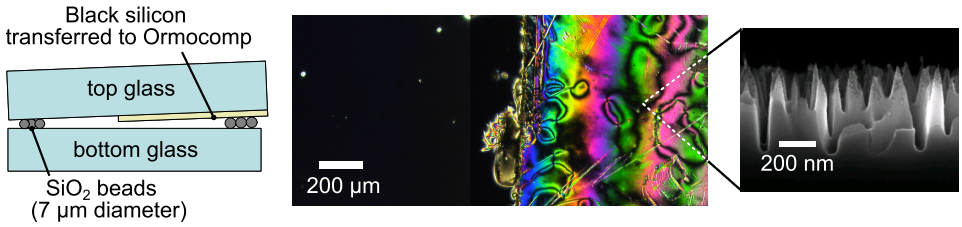

Figure 2.10: (a) Sample geometry. The glass is FDTS coated. (b) Microscope transmission image, sample between crossed polarizers. (c) Side view SEM image of black silicon on the silicon master. SEM image and Ormocomp replication are done by Alexander Bruun Christiansen, DTU.

2.5.1.3 Molecular orientation via electric fields

Alignment of nematic liquid crystals is also controlled dynamically via the application of an electric field. Even though the liquid crystal molecules do not have a permanent dipole moment, such a moment can be induced by an electric field. Positive and negative charge carriers are separated and accumulate at the ends of the long molecules, such that the molecules align parallel to the electric field.[63] As the molecules themselves are non-polar, the orientation is independent of the polarity of the electric field. Therefore relaxation into the ground state occurs only due to the elastic restoring force which minimizes the mechanical deformation energy. Consequently, the molecules can be switched between two stable orientations if an alignment via surface anchoring is established as shown in fig. 2.11. In the off-state, the molecules are aligned by the surface topography of the grating and if an electric field is applied the molecules are polarized to align parallel to the field lines. However, due to the different nature of the on- and off switching process, the response times can be substantially different. The

electrically induced on-switching depends on the electric field strength and can easily happen within a few microseconds. The mechanical relaxation is much slower and typically occurs on the order of 10 ms or longer. It should be noted that even though the polarity of the voltage does not affect the orientation of the molecules, it is still necessary to use a bipolar square wave voltage to prevent electrolytic effects which otherwise degenerate the LC molecules.[64]

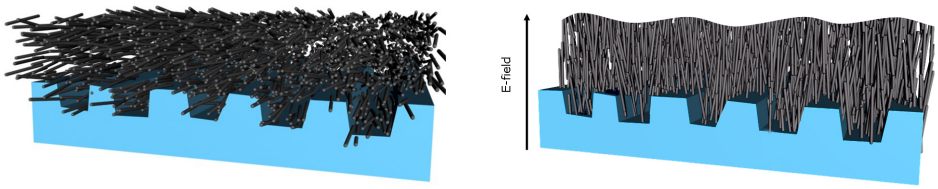

(a) (b)

Figure 2.11: Liquid crystal molecules aligned by a grating and re-oriented by an electric field. (a) $V = 0$, molecules align parallel to the grating. (b) $V > V_{th}$, molecules align parallel to the electric field lines, i.e. perpendicular to the grating.

2.5.2 Optical properties

The long chain character of the molecules leads to anisotropic optical behavior, where the material acts as a uniaxial crystal described by two principle refractive indices: the ordinary refractive index along the short axis and the extraordinary refractive index along the long axis.[63] The difference between these, the birefringence Δn, can be as high as 0.3 for some liquid crystals. If the LC orientation is modulated by an applied voltage, the refractive index can effectively be tuned between $n_\perp$ and $n_\parallel$. This makes liquid crystals interesting for many optical application, since no other material has such a pronounced electro-optic response. The temperature- and wavelength-dependence of 5CB are shown in figure 2.12. With increasing temperature the birefringence reduces, until it completely vanishes abruptly when the phase transition to the isotropic phase occurs. A typical method to characterize the ordering of liquid crystal thin films is via observation in a transmission optical microscope, where the sample is placed between crossed polarizers. One polarizer is used to polarize the incident light and the second polarizer, commonly called the "analyzer", is used to investigate how the polarization of the light changes upon transmission through the sample. Typical situations are shown in figure 2.13 and along these examples it is outlined how the typical colorful textures originate which are seen in unordered LC films. In the two leftmost cases the LC has homeotropic orientation and independent of the polarizer rotation the light transmitted through the sample is blocked by the analyzer. In the third case light is incident under an angle of 45° with respect to the LC molecules. Here the LC molecules cause re-polarization of the light, such that some light is transmitted even though the polarizer and analyzer are crossed. The fourth case considers an additional effect with unpolarized light.

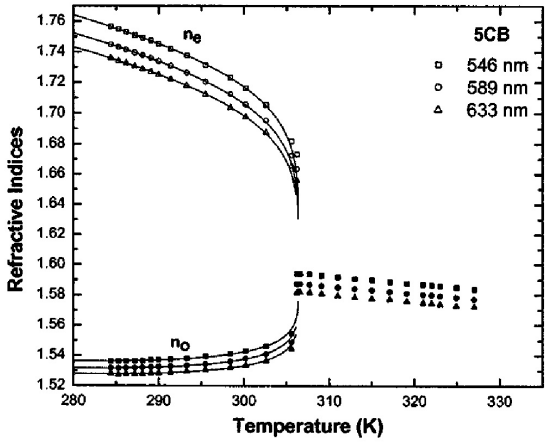

(a)

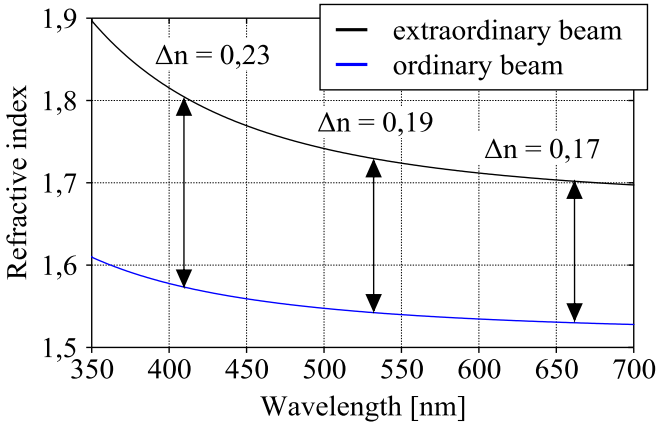

(b)

Figure 2.12: Refractive indices for the liquid crystal 5CB. (a) Temperature dependence . At about 33.5 °C the phase transition from the nematic to the isotropic phase occurs. Figure from ref.[65] (b) Wavelength dependence (temperature 25 °C). Data from ref.[66]

Due to the birefringence the two polarizations have different optical path lengths and one polarization is delayed with respect to the other one. The transmitted light still appears bright since the LC is ordered. If however the LC molecules are unordered, the interplay of re-polarization and different optical path lengths causes interference of the different wavelength constituents of the white light, such that a colorful pattern is observed.

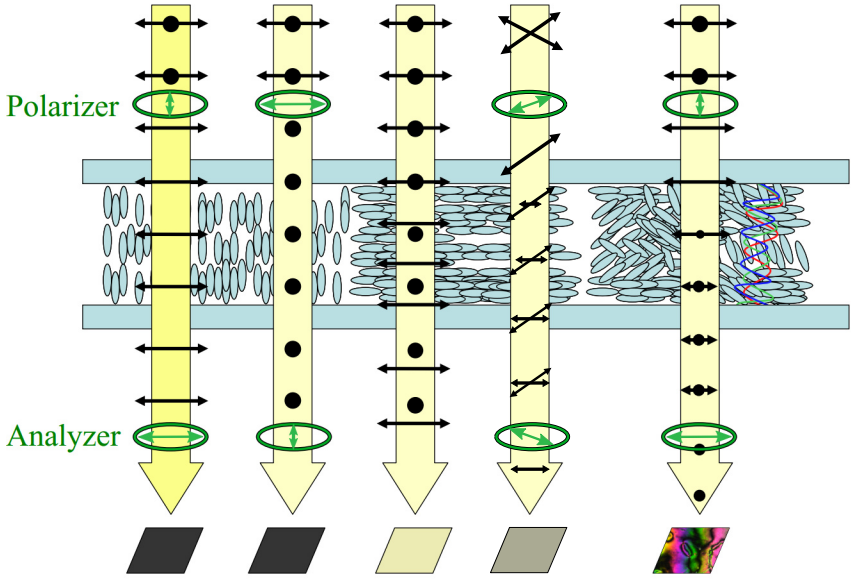

Figure 2.13: Typical cases of liquid crystal films in polarizing microscope. Black arrows and round spots indicate the orientation of the electric field. Green symbols indicate the orientation of the polarizer and analyzer

2.6 Basic laser physics

A laser amplifies light, such that an intense and coherent light beam is generated. This section outlines the theory behind lasers in general with a focus on aspects concerning dye lasers.

2.6.1 Laser basics

The principal components of a laser are a gain medium and a laser resonator. Optical amplification is achieved in the gain medium by stimulated emission. Figure 2.14 illustrates this process, together with the related processes of spontaneous emission and (stimulated) absorption. If a photon passes by an atom (or a molecule) it may be absorbed and transfer its energy $E = h\nu$ to the atom such that it is elevated to an exited state. After some time the atom will spontaneously decay back into a lower energy state and release the energy, possibly by emission of a photon. The energy of the photon corresponds to the difference of the two energy levels. Stimulated emission is a similar process, however, the emission of a photon does not happen spontaneously, but is induced by another incident photon. The special property of this process is the fact that the stimulated photon has the same wavelength, direction, polarization and phase as the incident photon. Stimulated emission requires that there are more photons in the excited state than in the lower laser level. This is called population inversion as the situation is inverted in the sense that usually more atoms will be in the lower energy levels. Therefore a means

to invert the population is required and possible methods to pump energy to the atoms are flash lamps, electric current, chemical processes or another laser.
If the amplification process happens inside a resonator, where the stimulated emission is reflected back and forth several times across the gain medium, then a manifold of photons, all traveling in the same direction with equal properties can be generated. An important prerequisite is that the reflections occur with constructive interference, so only wavelengths which yield constructive interference in a given resonator will be amplified. Different types of resonators

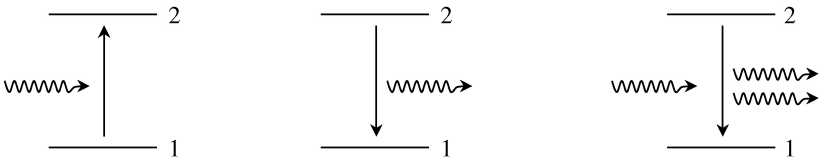

(a) Absorption (b) Spontaneous emission (c) Stimulated emission

Figure 2.14: Atomic absorption and emission processes.

are shown in figure 2.15. Panel (a) shows a classical linear resonator, where the gain medium is located between two mirrors with high reflectivity of e.g. 99.9% and 90%. Part of the photon flux inside the cavity is outcoupled through the lower reflectivity mirror as the useful laser light. This concept is used for many solid state and gas lasers, but is not very suitable to fabricate lasers in micro-scales by planar lithography processes. Panel (b) shows an alternative resonator concept. Here instead of two high reflectivity mirrors, many hundreds of small reflections are used to reduce the group velocity of guided photons and thereby effectively increase their lifetime inside the resonator while promoting stimulated emission.

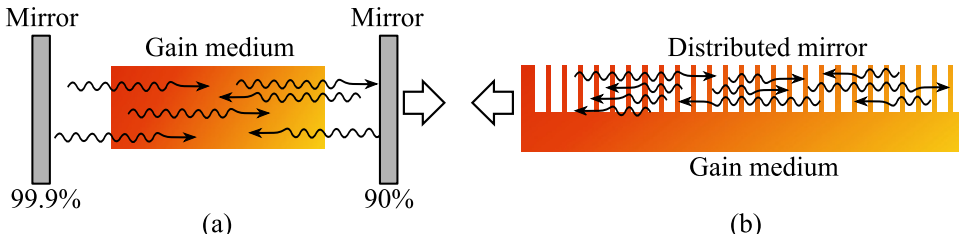

Figure 2.15: (a) A linear laser resonator with two plane-parallel high reflectivity mirrors. (b) A distributed feedback laser resonator with many low reflectivity mirrors.

2.6.2 Dye lasers

A dye laser uses organic dyes, dissolved in a liquid or embedded in a solid matrix, as gain medium. The laser dye used in this thesis is Pyrromethene 597, see figure 2.16(a) for absorption and emission spectrum. Amplification is possible in the

region where the curves do not overlap, i.e. approximately from 570 nm to 700 nm. Figure 2.16 shows the chemical structure of the dye molecule. A typical

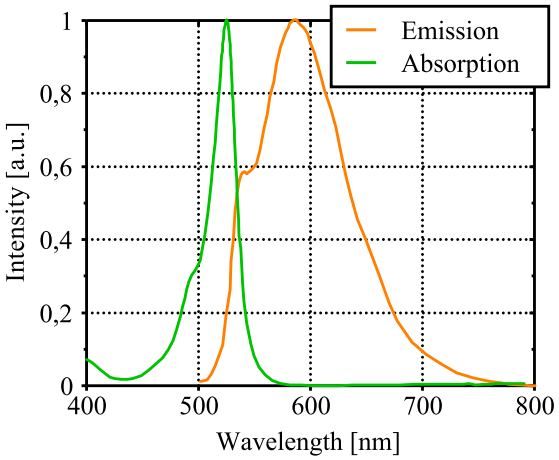

(a)

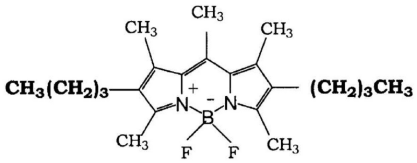

(b)

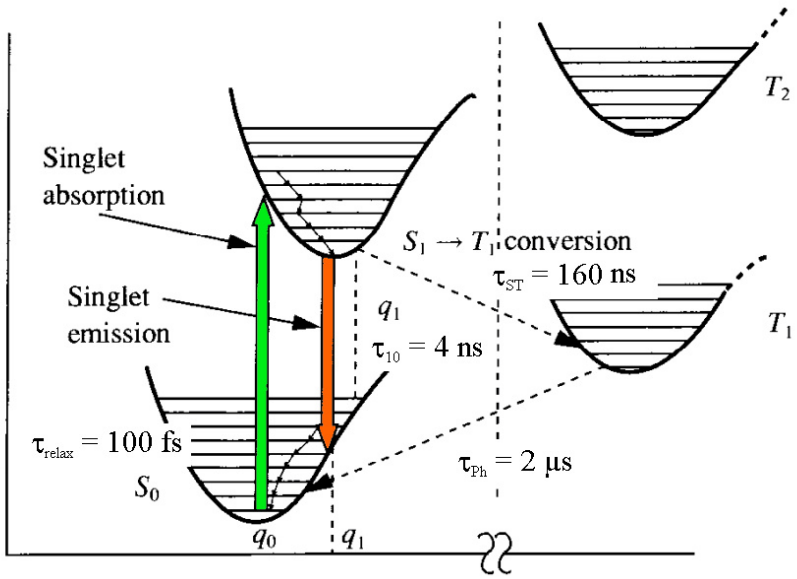

(c)

Figure 2.16: (a) Absorption and emission spectrum of Pyrromethene 597 dissolved in ethanol. Data from.[67] (b) Chemical structure of Pyrromethene 597 (from ref.[68]). (c) Simplified energy level diagram of a typical laser dye (drawing from ref.[50] , numbers are given for Rhodamine 6G, which is a laser dye with similar performance to Pyrromethene 597.[69,70]

energy level diagram of a laser dye molecule is shown in figure 2.16(c). This will be used to outline some specialties of dye lasers. The energy levels shown to the left are the singlet states and the parabolic shapes indicate the occupation

probability for these states. Pumping happens from the lowest level of the S_0 state to an upper level of the S_1 state. From here the molecules decay to the bottom of the S_1 state from where the Stokes shifted lasing transition takes place to the S_0 state. In order to achieve population inversion a laser dye should decay quickly to the bottom level of the S_1 state and have a long lifetime in this state. Also the decay back into the lowest level of the S_0 state should be fast, such that the molecule is available for pumping again. In such a four-level system the pumping populations are independent from the populations in the lasing levels and it is easier to achieve population inversion. As indicated in figure 2.16(c) the relaxation times within the S_0 and S_1 states are much shorter than the lasing transition as desired. However, transitions to the triplet state T_1 are possible, with very long decay times in the order of microseconds, without contribution to lasing. Due to these long times dye lasers are typically pumped by a pulsed source to use high pulse energies for lasing while giving the system time to relax to the ground state.

2.7 Solar irradiation on earth

Two of the devices presented in this thesis rely on sunlight for operation. Therefore the characteristics of solar irradiation on earth (insolation) are briefly discussed in this section. The sun's light is attenuated in the earth's atmosphere due to absorption and scattering. The spectrum of the solar radiation in space and on earth is shown in figure 2.17. The attenuation is empirically described by the air

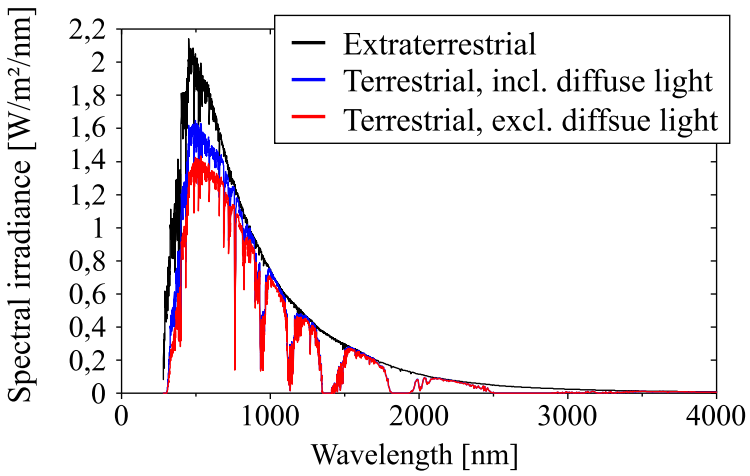

Figure 2.17: Solar spectrum extraterrestrial (black), direct solar radiation (red) and direct solar radiation including diffusely scattered light (blue). Data from.[71]

mass factor as stated in eqn. 2.6:[72]

$$AM = \frac{1}{\cos\theta + 0,50572(96,07995 - \theta)^{-1,6364}} \tag{2.6}$$

The absorption of the atmosphere can then be calculated by eqn. 2.7.[73] I_D is the *direct* intensity which arrives at the earth's surface without scattering. The *global* intensity, which includes also contributions from scattered light is typically about 10% higher, the exact value of course being very dependent on weather conditions.

$$\begin{aligned} I_D &= 1,353 \cdot 0,7^{(AM^{0,678})} \\ I_G &= I_D \cdot 1,1 \end{aligned} \tag{2.7}$$

Figure 2.18 shows the angle definitions which are used to describe the position of the sun relative to the earth. In panel (a) the angles are shown in relation to the earth's surface and in panel (b) as seen through a southwards facing window. The two most convenient angles to describe the position of the sun are the solar altitude α_s and the solar azimuth γ_s. α_s measures the elevation of the sun from the horizon and γ_s the rotation, with 0° defined as pointing southwards.

The trajectory of the sun in Copenhagen is shown in figure 2.19(a), over the course

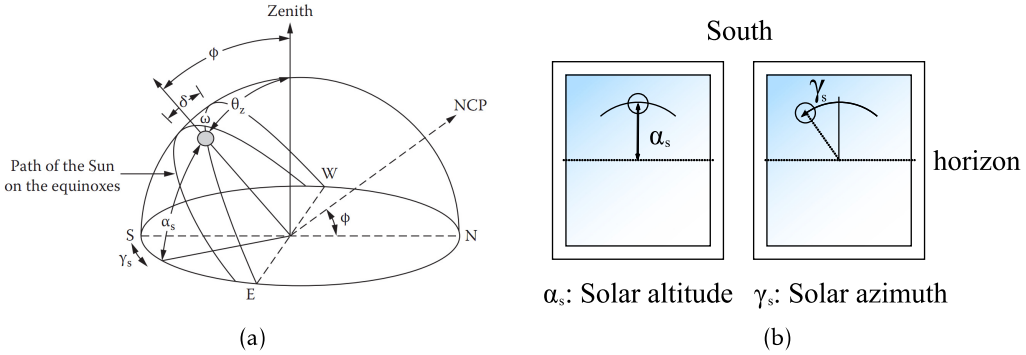

Figure 2.18: Solar angles in different reference systems. (a) Solar angles as seen from the earth's surface. Figure from.[74] (b) Solar angles as seen through a window. The combination of the two angles causes the sun to follow a curved trajectory.

of one year. The azimuth is constantly rotating with one revolution per day with the details not being visible on the compressed scale. Panel (b) shows for a more detailed view. The elevation angle is moving on an oscillating path with higher elevation angles in summer and lower angles during winter time.

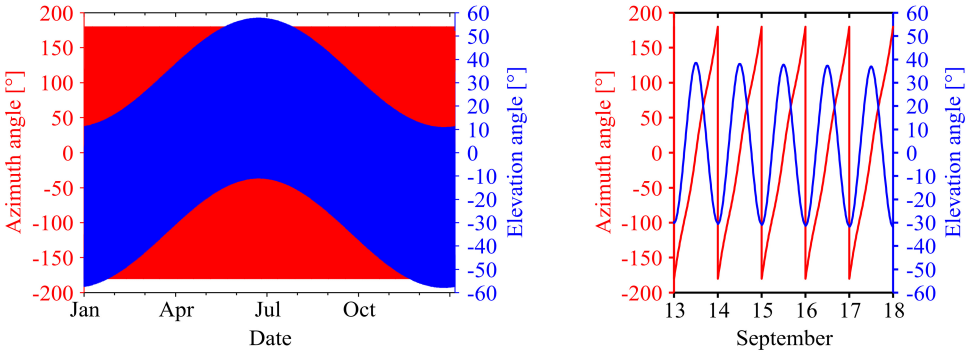

Figure 2.19: Path of the sun during, calculated for Copenhagen located 55° 40' North, 12° 34' 06" East) (a) Trajectory over the course of one year. (b) Trajectory over a five days.

3 Nanoscale fabrication methods

All samples presented in this thesis are based on sub-micron scale gratings or photonic crystals which are fabricated by means of micro- and nanotechnology. The most flexible techniques for fabrication of nanostructures are based on serial pattern writing, which is however very time-consuming. Therefore it is attractive to fabricate a master by e.g. electron beam lithography and then replicate this master in a relatively simple process. Here nanoimprint lithography (NIL) is used for replications, and in this way many replications can be fabricated from a single stamp, pointing to potential high volume fabrication of nanostructured devices.

3.1 Stamp fabrication

In the following the fabrication process for a NIL stamp is described. A typical material for NIL stamps is silicon due to it high strength and ease of fabrication with many established micro- and nanofabrication processes. However, since the imprint method which is used is based on a combination of mechanical deformation and UV-curing, a transparent substrate is chosen for the stamp. The fabrication is divided into e-beam lithography, UV-lithography and imprint preparation. In this section only the basic process steps are outlined, for the detailed parameters the reader is referred to the appendix.

3.1.1 Electron beam lithography

The starting substrate is a 10 cm diameter fused silica wafer of 1 mm thickness (Jinsol, Seoul, Korea). The wafer is stored in an oven at 250 °C over night in order to dehydrate the surface to promote adhesion of resist. The e-beam resist (ZEP520A diluted in anisole), is spin coated to a thickness of ≈ 150 nm. Next, a 15 nm layer of aluminum is deposited onto the resist layer as shown in figure 3.1, with the purpose to avoid charging of the non-conductive resist on a non-conductive substrate during e-beam lithography. It should be noted that thermal evaporation is used, because electron-beam evaporation, which is usually more common, would cause exposure of the resist. The e-beam pattern is written with a dose of 180-240 $\mu C/cm^2$, at 100 keV acceleration voltage and 1.34 nA current. The actual dose depends on the the coverage of structures because a significant fraction of the exposure is caused by backscattered electrons. For gratings, a dose of 180 $\mu C/cm^2$ is sufficient while photonic crystals need up to 240 $\mu C/cm^2$. After e-beam exposure the charge compensation layer is removed by wet chemistry (MF-322) in a petri dish. Following this, the resist is developed using the commercial

ZEP developer ZED-N50, under mild agitation by manually moving the dish. Figure 3.1 shows drawings of the wafer at this stage. The next step is to apply

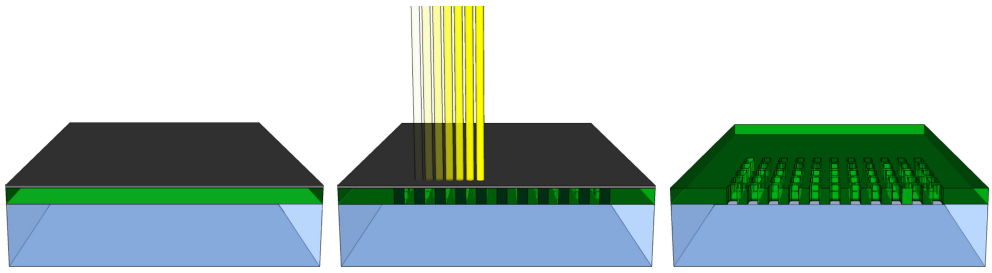

(a) Resist and Al coating (b) E-beam exposure (c) Development

Figure 3.1: E-beam lithography

an etch mask for the etching of the nanostructures. To do this another layer of aluminum is evaporated by electron-beam evaporation, with a thickness of 30 nm. Here it is recommended to use a machine which has large distance between wafer and crucible (Wordentec QCL800 at Danchip), such that a more directional evaporating is achieved where the sidewalls of the holes are not covered. This eases the following lift-off step of resist and aluminum on top of the resist in an ultrasonic bath. Now only the areas which were exposed by the e-beam are covered with aluminum (compare figure 3.2(a)-(b)). The next task is to etch the pattern

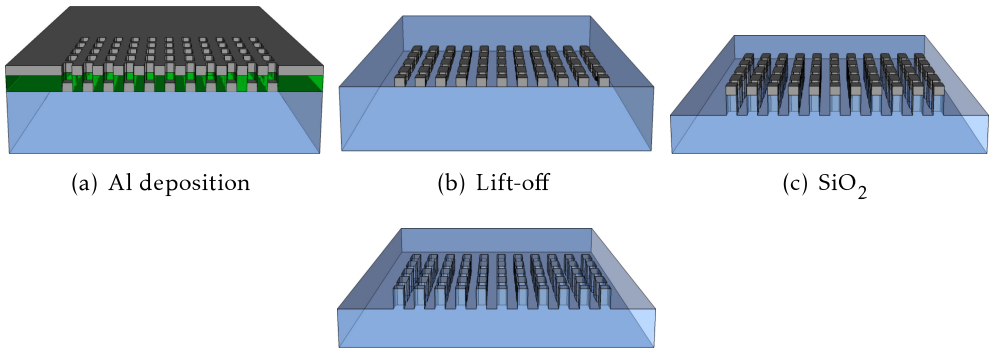

(a) Al deposition (b) Lift-off (c) SiO_2

(d) Aluminum etch

Figure 3.2: Lift-off and nanostructures etch

into the glass by reactive ion etching using a combination of CF_4 and CHF_3 gases. For most samples a depth of 120 nm is used, but values up to 300 nm are possible. Finally the nanolithography step is completed by removing the aluminum by wet-etching, see figure 3.2(d).

3.1.2 UV lithography

Often a combination of large and small patterns are required on a stamp and since e-beam writing is a very slow process it is often not feasible to write the entire pattern by e-beam exposure. Instead, the large patterns are defined by UV lithography. Because the large patterns will also be transferred different during the nanoimprint step, they are not directly etched into the glass like the nanostructures, but as a chromium mask which is planar with the bottom of the nanostructures. First adhesion promoter HMDS (hexamethyldisilazane) is applied

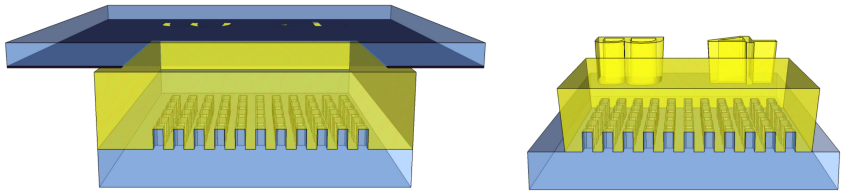

(a) UV exposure (b) Image reversal and development

Figure 3.3: UV lithography

to the wafer. Figure 3.3 shows the next step: the wafer is coated with UV sensitive photoresist (1.5 µm AZ5214B) and the area of the large patterns is exposed. In order to achieve negative sidewalls, image-reversal is used which means that the resist is exposed through a mask and baked on a hotplate at 120 °C. In this way crosslinking of the resist molecules happens in the exposed areas. A flood exposure on the whole wafer makes the non-crosslinked regions soluble in AZ 351B developer.
The next step, shown in figure 3.4, is another reactive ion etch in order to remove 100 nm of the fused silica. Subsequently the etched regions are filled with chromium by e-beam evaporation. Lift-off in an acetone bath with ultrasound is

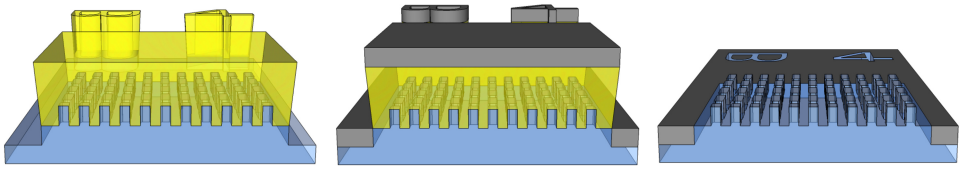

(a) SiO_2 etch (b) Cr deposition (c) Lift-off

Figure 3.4: Shadow mask deposition

used to dissolve the AZ resist and to remove the spare chromium. During the imprint process the chromium acts as shadow mask for UV curing.

3.1.3 Imprint preparation

An anti-stiction coating is required in order to prevent adhesion between stamp and substrate after imprinting and to reduce wear of the stamp. Before this,

the stamp is cleaned in 7-up (Sulfuric acid and ammonium peroxodisulfate at 80 °C) and by an oxygen plasma. An anti-adhesion coating is then applied as a self-assembled monolayer of (1H,1H,2H,2H-perflourodecyltrichlorosilane, FDTS) via chemical vapor deposition.

3.2 Nanoimprint lithography

Two general types of nanoimprint exist, thermal NIL and UV-NIL.[75] In thermal NIL the replication process is purely mechanical and the resist is heated to lower the viscosity during imprint. Problems are stamp bending if large structures are to be imprinted and longer process cycles due to the required heating and cooling. UV-NIL has the disadvantage that it requires a transparent stamp and optical effects like reflection and diffraction may compromise the resolution. Since fabrication processes in fused silica are established and resolution limitations are not observed, UV-NIL is used in this thesis for the majority of the imprint processes.

3.2.1 Substrate preparation

For imprinting materials SU-8,[76] Ormocore[77] and PMMA are used. PMMA is a thermoplastic for use in thermal NIL. SU-8 and Ormocore are both chemically amplified, UV-sensitive photoresists used for UV-NIL. The materials are deposited as thin-film between 400 nm and 3 µm thickness by spin-coating onto a glass wafer. Heating on a hotplate is used to evaporate the solvents and thus solidify the resist, with the exception of Ormocore which is only shortly baked and remains viscous. All of these resists are transparent at visible wavelengths and the refractive indices are shown in figure 3.5.

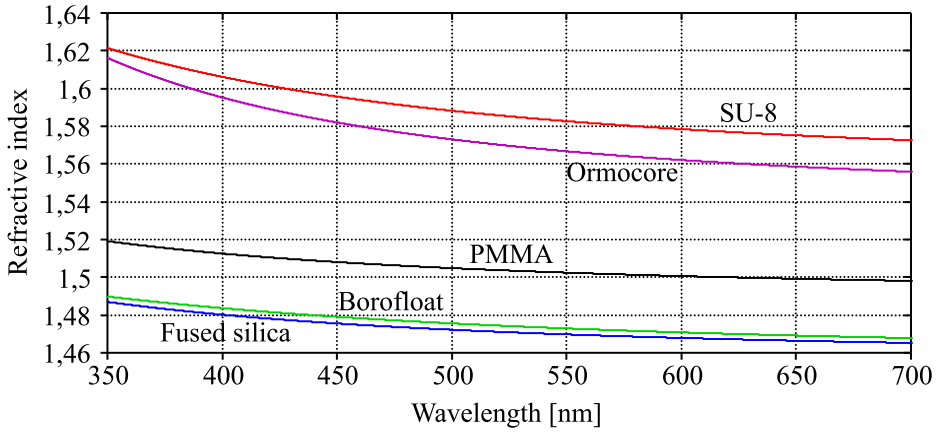

Figure 3.5: Optical dispersion of various substrate and resist materials.

3.2.2 Imprint process

For imprinting the stamp is placed onto the imprint template and carbon pads are placed on top and bottom which yields a more homogeneous pressure distribution. Imprinting of Ormocore is done at 10 kN and at room temperature. SU-8 is imprinted at 90 °C and PMMA at higher temperature around 160 °C. PMMA is separated from the stamp directly after imprinting and the process is finished at this point. Ormocore and SU-8 still need to be cross-linked, therefore stamp and imprint are kept in contact and are then exposed through the stamp with UV light. This generates precursors for cross-linking and by heating the imprint wafer (still in contact with the stamp), the cross-linking is finalized. After separation unexposed resist is dissolved in a chemical developer. The process is illustrated in fig. 3.6.

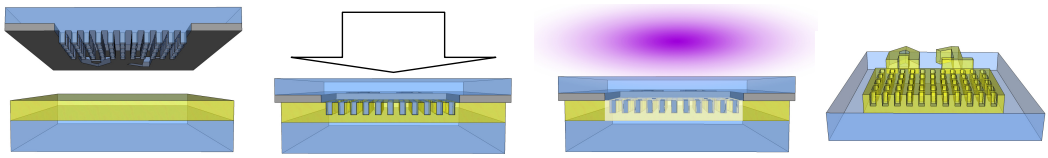

Figure 3.6: Illustration of the UV-NIL process. (a) Alignment of stamp and substrate. (b) Imprinting. (c) UV-light curing. (d) After demolding.

4 Measurement setup

For optical characterization of the fabricated samples an automated measurement setup is designed and build. In the following the requirements for this setup are specified, the design is discussed, different measurement possibilities are presented and the data processing procedures are outlined.

4.1 Functional specification

The setup is designed with the objective to measure angle-dependent optical properties of gratings and photonic crystals. Since this needs to be achieved for transmitted and reflected light and also for light redirected into waveguide modes in transparent samples, a high degree of versatility, both in the actual setup and the software is required. This approach has proven to be very successful and the setup is used in a number of other optics-related research projects in the Optofluidics group. The following rather broad requirements are defined:

- Spatially resolved measurement of two-dimensional diffraction patterns of gratings.
- Measurement of light redirection of photonic crystals and gratings, wavelength- and angle-dependence.
- Angle-dependent measurement of light reflection, absorption and scattering, for both monochromatic and white-light.

Not only are the types of measurement very diverse, but also sample types ranging from small and thin pieces of silicon to 6-inch sized, 3 mm thick glass panes are studied.
Typically a measurement involves a light source, some sort of mechanics which e.g. rotates the sample and a detector which records the change in light intensity or spectrum due to interaction of the light with the sample. In order to achieve the required flexibility to perform these different kinds of measurements the setup is constructed with a modular approach. The light sources and a basic sample stage are kept fixed, while additional equipment like detectors and sample holders for specific sample types can be inserted, depending on the requirements. In order to minimize alignment time, optical rails with common counterparts on all detectors, flip-mirrors and magnetic mounts are used. The following measurement schemes are possible with the available hardware and software:

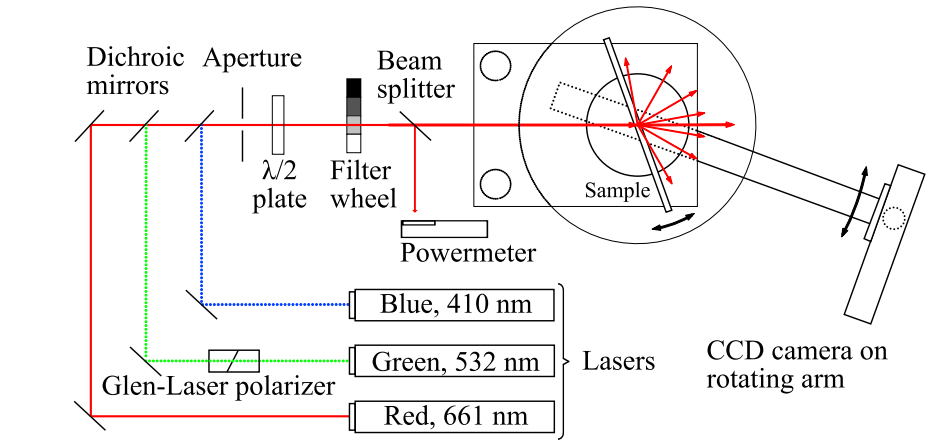

(a)

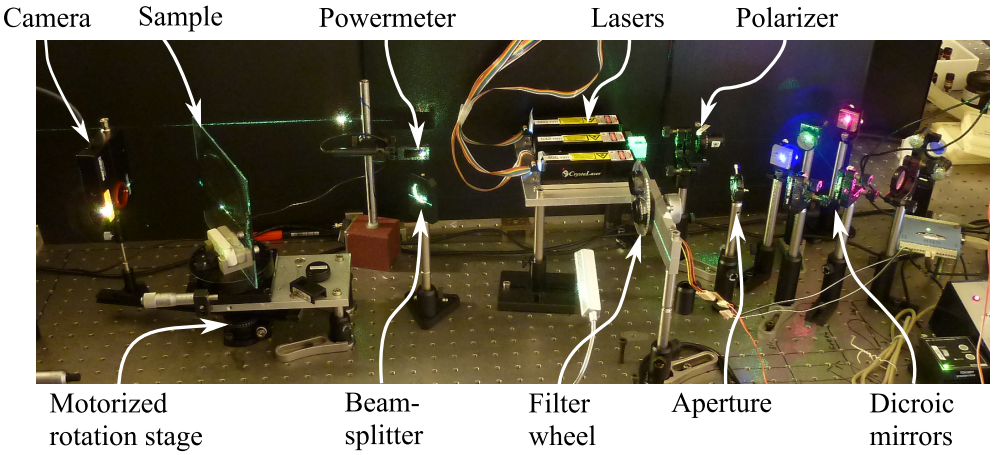

(b)

Figure 4.1: The measurement setup for optical characterization in configuration I (detector rotating around fixed sample) (a) Drawing of the setup. (b) Photograph of the setup.

I The sample angle is fixed with respect to the incident light and the detector rotates around the sample.

II The sample rotates and a fixed detector measures transmitted light.

III The sample rotates together with the detector to measure redirected light as function of incidence angle.

IV The sample rotates and the detector rotates with twice the sample angle to measure reflected light.

V The sample rotates and for each sample angle, the detector rotates around the sample.

Figure 4.1 shows a drawing (panel (a)) and photograph (panel (b)) of a typical configuration for a measurement of type I where a CCD camera rotates around the sample to record the transmitted diffraction pattern. The sample is positioned on an elevated stage, below which a rotation stage is placed which carries the detector, mounted on a long arm, such that it can rotate around the same

4.2 Choice of components and optical design

4.2.1 Light sources

Depending on the type of measurement, different light sources may be chosen:

- CW Lasers
- Xenon lamp
- OPO
- LEDs

For most measurements the CW lasers are the preferred choice. Since the optical diffraction and bandgap effects which occur in gratings and photonic crystals are usually very dependent on the wavelength, a narrow band light source gives the best insight into the physical processes involved. A set of three lasers with wavelengths of 410 nm, 532 nm and 661 nm (about 1 nm linewidth) is used to cover the borders and the center of the visible spectrum. See figure 4.2 for measured spectra of the three lasers. In addition to narrow wavelength the laser also offer

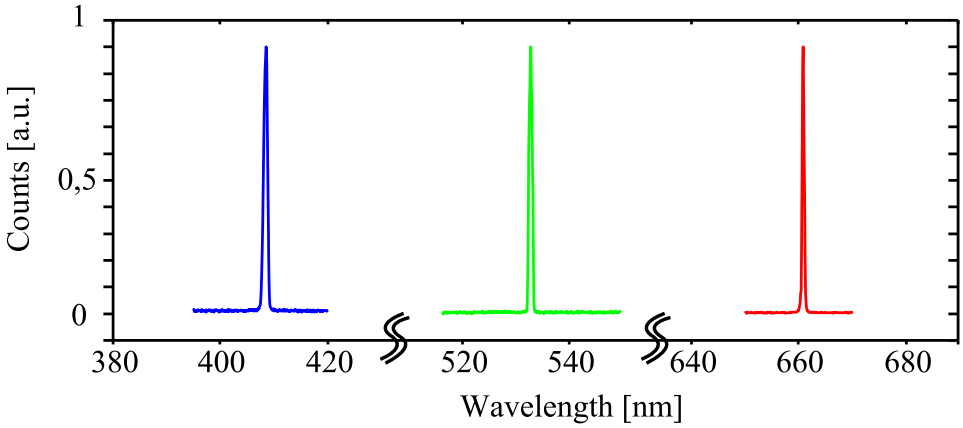

Figure 4.2: Measured spectra of the three lasers.

stable and adjustable output power and low divergence (2 mrad) and spot size (≈1 mm) make it possible to precisely probe small areas on the sample. A critical is the beam quality and especially the beam circularity. These are important for focusing the beam onto a small, round spot, but also to measure e.g. distortion of the beam pattern upon transmission through a grating. The green laser is a diode

pumped solid state laser (DPSSL) which inherently has a very round Gaussian mode profile. The red and blue lasers however are diode lasers and the the design of these lasers, typically ridge waveguide lasers with rectangular ridges, may easily cause higher order modes to oscillate. Round modes are only possible with narrow ridges, which however limit the available output power. Therefore low power lasers with maximum output power of 25 mW are chosen. Still, the beam profile of the diode lasers is superimposed with a non-circular background, which has rather weak intensity, but is still recorded in the measurements. In order to cut off these non-Gaussian parts of the intensity profile, an aperture is placed in the beam path and figure 4.3 shows a measurement of the beam profiles, after passage through the aperture. Finally, the polarization of the lasers needs to be considered. For the measurement of polarization dependent structures the lasers should be linearly polarized and a polarization ratio of 100:1 is considered sufficient. This is achieved by the diode lasers (blue and red), but not by the green DPSSL, which is therefore equipped with an external Glen-Laser polarizer (polarization ratio 1000:1).

Since many applications in this project are related to sunlight, a white light xenon

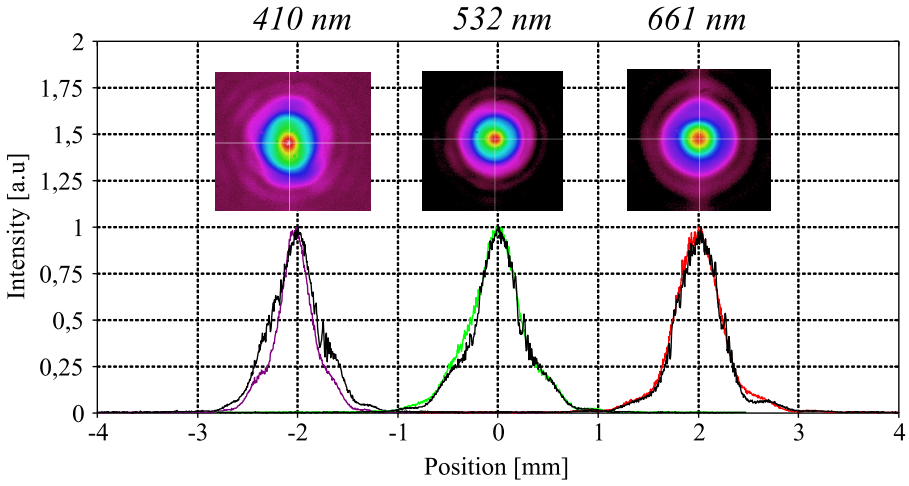

Figure 4.3: Measured beam profiles of the three lasers (colored trace: x-axis, black trace: y-axis).

lamp is also installed such that wavelength dependent devices can be characterized with light spectra similar to sunlight. The lamp is coupled to an optical fiber whose output beam needs collimation for efficient illumination of the typically only a few square millimeter large test areas. This is best achieved with an off-the shelf fiber collimator and an additional long focal length convex lens. Another disadvantage is the warm up time of about 30 minutes before the output power is stabilized. In comparison the white light source is more suitable when relative measurements at a few angles are required and the exact spectral response is of interest. In contrast, the lasers are more suitable when absolute measurements are required or measurements of the angular response are desired with the three fixed laser wavelengths being sufficient.

Another alternative is an optical parametric amplifier which is pumped by a Q-switched 355/532 nm laser. By rotation of the crystal any wavelength between 410 nm and 2600 nm can be selected. The available system however has a few disadvantages: Output power varies with wavelength, there is a large pulse to pulse energy deviation (up to a factor of 10) and the wavelength is not calibrated. Improving the pulse to pulse variation would enable measurements at selectable wavelengths throughout the visible and infrared spectrum which may be important for some applications.
Finally, red, green, blue and white light emitting diodes are available for measurements of spectral responses to non-coherent light.

4.2.2 Polarization and intensity control

For a number of measurements it is important to control the intensity and polarization of the probing light. The intensity of the lasers can be controlled within a range from about 20% to 100% of maximum power. If more reduction is needed (e.g. for measurement of the 0th diffraction order of a grating, which may be 1000 times brighter than the other orders), it may be necessary to use additional neutral density filters. to avoid saturation or damaging of detectors. Therefore a custom build filter wheel with four slots (open, blocked, ND3.0 and ND4.0) is included in the setup. In order to monitor the output power of the lasers a non-polarizing beamsplitter directs part of the beam to a powermeter (Ophir NovaII with PD300 head), which serves as reference of the power incident on the sample. For control of the polarization direction of the linearly polarized lasers a broadband half-wavelength plate (Thorlabs AHWP05M-600) is used.

4.2.3 Mechanics

Two rotation stages are used, one for rotation of the sample and the other for rotation of the detector around the sample. The important parameters for selection of a rotation stage are speed, maximum load, accuracy and ease of use. There are two velocities which are important: motion velocity and communication speed. If measurements are e.g. only performed at a few distinct angles in steps of 10°, the communication time is negligible and the motion speed limits the measurement time. However, if measurements are made with e.g. 1000 steps of 0.1° each, then the communication time may actually exceed the motion time. For this reason the speed specifications from the manufacturers may not be meaningful and it is recommended to do practical test e.g. with a loan device. For optimization of the communication time a careful look at the software is necessary: A typical sequence may for example be to set the motion angle, execute motion and wait until the motor is ready. If many steps with the same angle are used, the "set motion angle" command may be sent only once and then omitted, which significantly reduces the total time of the measurement. Another critical parameter is the maximum load. Typically only the load on the center axis is specified by the manufacturer, but not the torque exerted by an off-axis load of the arm and the detector. Again a practical test has to be conducted. The accuracy of most commercially available rotation

stages exceeds the minimum requirements of 0.01°. Another not obvious, but still important point is the ease of use. Even though the stages are typically computer controlled, it is often necessary to move them manually, e.g. for alignment purposes, and here a system which works independent of a computer with a joystick becomes very handy. The two stages used in the setup are a DC motor Thorlabs CR1 M-Z7 and an Owis DMT100 stepper motor. The Thorlabs stage is well suited as a rotation stage for the sample, since it is compact and has a manual controller for convenient sample alignment. The Owis stage is used for rotation of the detector which can be securely mounted on a long arm due to the large diameter of the stage. Furthermore, it provides short enough communication time (83 ms, 1000 steps of 0.01° = 84 s) and moves fast when traveling large distances (9.5°/s). Since it is a stepper motor, the position is always known exactly and reproducibility is guaranteed.
Also the mechanical stability of the detector which is placed on the extended arm must be considered. Rigid components and tight mounting should be used and even then the detector might vibrate slightly after movement. Therefore a small idle time after each motion step is recommended if camera images are recorded to make sure that the captured image is sharp. Otherwise the diffraction pattern will become blurry and the post- processing image registration (see section 4.3.2) will not work.

4.2.4 Detectors

Six different detectors are available for use in the setup and implemented in the software. Depending on the chosen light source and purpose of the measurement, a suitable detector has to be chosen.

Laser beam profiler CCD camera

When a high resolution, 2D measurement of the diffraction pattern on the full 180° half circle around a grating is required, a CCD camera is used, see fig. 4.4(a). In order to achieve accurate measurements, the Spiricon SP620U, a scientific quality laser beam profiler camera is used. It has a resolution of 1600 x 1200 pixels, high dynamic range (62 dB) and linearity of ±1%. The sensor area has a size of 7 x 5 mm, such that the final measurement has to be stitched from many individual measurements.

CCD array

If a larger vertical extent needs to be scanned, a CCD array may be used as shown in fig. 4.4(b)-(c). The sensor is an ILX553A device and electronics is delivered by Spectronic Devices. With 5150 pixels of 7 x 7 µm size, the sensor has a length of 36 mm. The small width of the pixels makes it necessary to scan the sensor at equally small steps which leads to much longer measurement times compared to the CCD camera. On the other hand, the sensor can be mounted horizontally to make quick 1D measurements with only a few measurements required to cover a

full 180° range.

Photodiode and optical powermeter

Often instead of an image, only a one-dimensional scan is required which significantly reduces measurement time and amount of data storage. For fast and calibrated absolute power values, ranging from 0.1 nW to 30 mW, a commercial photodiode, connected to an optical powermeter is used (Ophir NovaII with PD300 head). However, such detectors are typically built into rather bulky heads. When a more compact solution is needed, e.g. if the sensor should be placed directly against the side of a glass piece, it is more practical to use a photodiode (Osram BPW21 or Thorlabs FDS1010) connected to a high accuracy multimeter (Keithley 2000). The drawback of this method is that the photocurrent needs to be calibrated against an optical powermeter.

Fiber coupled spectrometer

When spectrally resolved measurements are required, a fiber coupled spectrometer is used. The dynamic range is significantly lower compared to photodiodes, such that it may be necessary to adjust the integration time during the measurement or use external attenuation filters. With this it is not possible to measure absolute power values unless a calibrated integrating sphere is used. Even the measurement of relative values (e.g. redirected light / incident light) is often not possible because the small fiber only collects a fraction of the light (see fig. 4.4(d).

Color camera and pocket microscope camera

Finally a compact CMOS color camera (LogiLink Webcam) and/or a microscope camera (Delock Penscope) may be used for observation of the sample during measurement.

4.3 Measurement software

The measurement software is designed as a two-stage approach. First, control of the measurement devices and data acquisition is done with a Labview program. This program saves measurement data in compact form, with corresponding header information. Afterwards the data is processed by a Matlab script which handles analysis and plotting of the results. This division of the measurement process is motivated by the advantages of Labview in controlling physical devices on the one hand and better support of mathematical and graphical functionality in Matlab on the other hand.

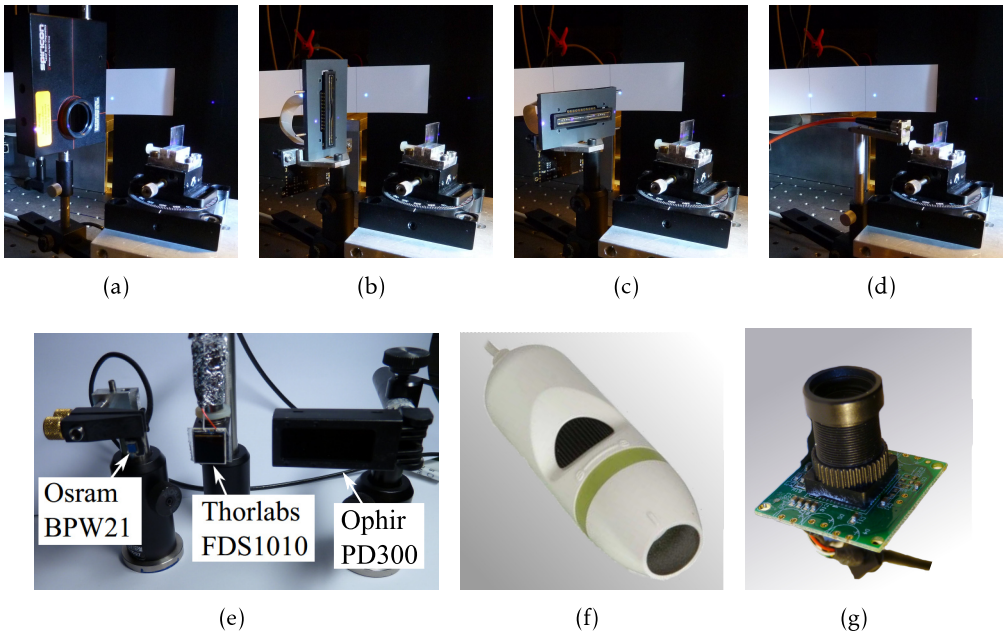

Figure 4.4: Available detectors (a) CCD camera. (b) CCD array, vertical mounting. (c) CCD array, horizontal mounting. (d) Spectrometer, fiber coupled. (e) Photodiodes. (f) Microscope camera. (g) Compact color camera.

4.3.1 Labview data acquisition

All components of the setup are controlled with Labview to allow for automated measurements. The requirement is that the measurements should be run automatically, except sample exchange and alignment. The program is prepared to perform a vast variety of automated measurement sequences directly through the user interface without additional programming. A picture of the user interface is shown in figure 4.5. A common task would be for example to measure optical power or spectrum of reflected/transmitted light for a series of sample angles. Many combinations of "inputs" (set points) and "outputs" (measurements) are possible and table 4.1 lists the available instruments. A flow chart which outlines the operating of the Labview program is included in the appendix A.4.1.

4.3.2 Matlab data post-processing

Often measurements of large-area light intensity patterns are required, which are much larger than the detectors. Therefore the detector is mechanically moved and the final measurement is comprised of many individual measurements which need to be stitched together. Due to inaccuracies in the alignment and mechanical quality of the components, it is not possible to adjust the rotation angle of the detector such that the individual frames are aligned perfectly side-by-side. Instead, the rotation angle is deliberately chosen such that an overlap of approximately 10% between each frame is achieved. After the measurement

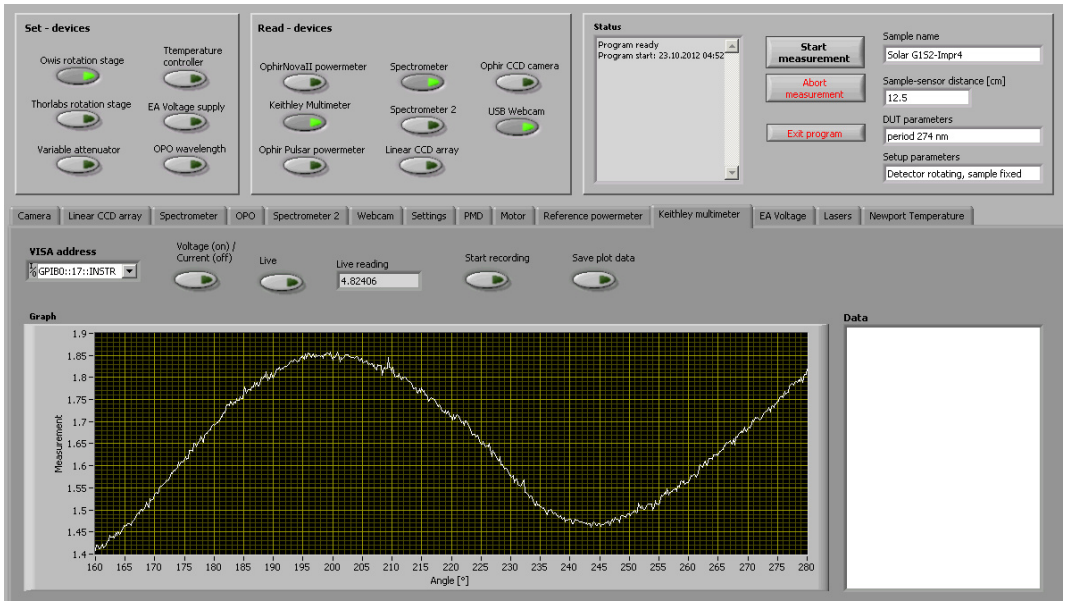

Figure 4.5: Screen capture of the user interface of the Labview program. In the upper panels the used devices are selected and sample information can be stored. For each instrument there is a separate tab where settings are entered and data is displayed.

the collected data is processed by a Matlab program which calculates the overlap from the images. Addressing this problem is called "image registration" in digital image processing.[78] A typical measurement of two adjacent images from a grating measurement is shown in figure 4.6(a). The overlapping regions are detected by comparing sections of the adjacent side of the images by means of a cross-correlation based approach.[79] In order to reduce the calculation time, the area which is used for cross-correlation is determined automatically determined. In the horizontal direction, the area is adaptively changed based on successful results of the previous frames, as it can be expected that the overlap is roughly constant. Horizontally the cross-correlation is limited to the high intensity region in the center and the dark regions, usually present at the edges are omitted. See figure 4.6(b) for a closeup of the overlap area. The normalized cross correlation is calculated according to to eqn. 4.1.

$$C(u,v) = \frac{\sum_{x,y}\left[f(x,y) - \bar{f}_{u,v}\right]\cdot\left[t(x-u,y-v) - \bar{t}\right]}{\sqrt{\sum_{x,y}\left[f(x,y) - \bar{f}_{u,v}\right]^2 \cdot \sum_{x,y}\left[t(x-u,y-v) - \bar{t}\right]^2}} \tag{4.1}$$

This can be calculated in spatial or frequency domain, where frequency domain calculations by means of the numerical fast Fourier transform may be an order of magnitude faster, depending on the size of pattern and template.[80] Matlab estimates the fastest method before the calculation and chooses spatial- or frequency domain accordingly.[81] Figure 4.6(c) shows the normalized cross

Inputs	**Specifications**
Rotation stage 1 (Thorlabs)	360° cont., 0.01° res.
Rotation stage 2 (Owis)	360° cont., 0.05° res.
Voltage/Current source	0-200V, 0-5A
OPO wavelength	410 nm - 2630 nm
Temperature controller	-20°C - 80°C
Function generator (Agilent 33250A)	Arb. waveform, max. amplitude 10V
Laser power	0-25 mW, manual or automatic
Laser wavelength	≈ 1 nm, (thermal tuning of Linos Nano250 lasers)
Time (e.g. 1 measurement per second)	Manually triggered or automatic
Outputs	**Specifications**
CCD camera	1600 x 1200 pixel
CCD array	51550 x 1 pixel
Spectrometer 1 (Jazz)	225-986 nm, res. 350 pm
Spectrometer 2 (HR2000 VIS)	510-705 nm, res. 150 pm
Spectrometer 3 (HR4000 UV)	340-550 nm, res. 35 pm
Spectrometer 4 (HR4000 VIS)	550-620 nm, res. 35 pm
Optical powermeter	Accuracy ± 3%, res. 10 pW
Color camera	640 x 480 pixel
Multimeter (Keithley 2000)	res. 10 nA / 0.1 µV
Oscilloscope	4 CH, 100 MHz, 1.0 GS/s

Table 4.1: Summary of available instruments grouped as inputs or outputs in the Labview control program. A measurement may control 1-2 inputs and record any number of outputs.

correlation signal of the compared sections. At the maximum the best overlap between the two images is found.
There are two cases when the cross correlation does not provide a good estimate: either when the light intensity is very low and darkness or noise dominate the image or when the diffraction pattern is periodic, such that there is not a unique position of best overlap. In order to compensate these cases, first the best overlap for all frames is determined and finally results which significantly differ from the average overlap are replaced by that value. It is also important to select the overlap region appropriately since a large search region reduces the probability of encountering similar and periodic patterns. The quality of the method can best be evaluated when looking at one-dimensional data. In figure 4.6(b) the integrated intensity of the two adjacent images after determination and correction of the overlap is shown. This image registration process and correction of the overlap is applied on all images of the measurement. In addition to this also a hemispherical mapping is applied which corrects the fact that the diffraction pattern should be measured along a circle, but the camera sensor is actually flat. The intensity of the measurements is also corrected, based on the measurement of the reference

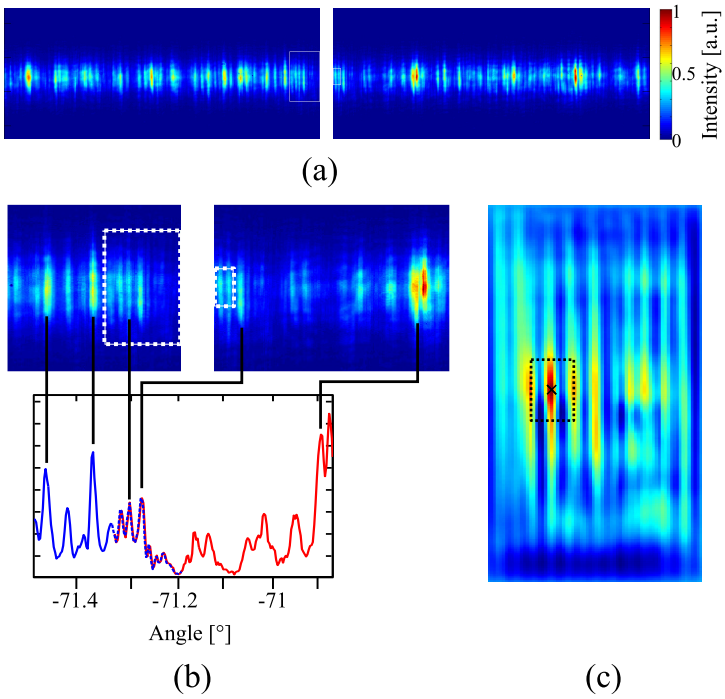

Figure 4.6: (a) Two adjacent images measured on a diffraction grating. (b) Close-up of the overlap region. The search areas which are used for determination of the overlap by cross correlation are marked with rectangles. The plot at the bottom shows the intensity profile after correction of the overlap. (c) The maximum of the normalized cross-correlation of the two search areas is used to determine the overlap. The correlation between template and pattern is 0.92.

detector to compensate intensity variations of the lasers. Finally the composed complete image is saved and 1D traces of the integrated intensity along the vertical axis are saved.

5 Solar harvesting via nanostructured glass panes

In this chapter, the concept, design, fabrication and characterization of a solar light harvesting device, which can be integrated into window panes, is described.

5.1 Physics and principle of operation

Building façades present a large surface area that is attractive for solar harvesting use. The area is otherwise unused and electricity can be generated directly at the point of use, as opposed to solar parks in remote locations. Since a significant fraction of modern office buildings' façades is covered with glass windows, it is therefore highly beneficial for a building to have solar harvesters integrated into its windows. In this way the architectural design of the building is not affected. If the incident sunlight could be partly redirected to the side of a window, only a small area would be required for solar cells. Considering a one square meter size window, with 1 cm wide solar cells on all four edges, the size of the solar cells is as small as 4% of the total window area. Consequently, such a system is considered to be a solar concentrator. As discussed in the introduction section, solar harvesting on transparent glass panes may also be interesting on a much smaller scale, such as in displays of portable electronic devices.
AN optimal solar harvesting window should comprise the following properties:

- Transparency of the window
- High optical efficiency
- Cost-effective fabrication
- Long-term durability

Transparency should be understood as the minimal combination of intensity loss due to redirection, which is desired and inevitable and distortion of the view through the window due to scattering, refraction and diffraction. Whether distortion is an issue and which of the mentioned processes dominates depends on the size of the features on the window. Intensity loss due to redirection in a perfect solar concentrator with 100% efficiency would convert all incident light into electricity, such that the window appears black, thus making the window superficial. Therefore a suitable compromise has to be found, which is however inherently determined by the optical efficiency. This is limited to about 10% for gratings of dimensions small enough to be invisible to the naked eye. Also a

cost-effective fabrication must be possible, preferably by a large scale replication process like roll-to-roll nanoimprint. For solar harvesters to be used in electronics displays this is feasible and optical structures for purposes like anti-reflection foils have been fabricated in this way.[82] For window panes, the areas are even larger and fabrication tools are yet to be developed. Replication-based fabrication also imposes restrictions on the optical design, limiting the structures to surface patterns without undercuts. Finally, the material has to be long-term stable to UV-light. For electronics, lifetimes of 5 years may be acceptable, but windows have to last more than 20 years, and are both constantly and directly exposed to sunlight. Some kinds of PMMA have been developed for long-term outdoor used, but ideally a material which is free of organic compounds, but still can be imprinted is used. Such a material will be discussed in chapter 6. Also mechanical stability is an issue and the nanostructures must withstand temperature variations, weather, cleaning, etc. This may be addressed by placing the nanostructures at the inside of a double-glazing.
In order to fulfill these requirements, the solar harvesting mechanism investigated here is based on sub-wavelength grating couplers which are applied into a thin-film on top of the glass. The grating couplers convert the incoming sunlight to guided waves inside the glass pane, directing the light to the edge of the glass where it can be harvested by small area, high efficiency multi-junction solar cells.[4] The grating period and depth are chosen small enough, such that the grating is invisible to the naked eye and vision through the window pane is not significantly distracted.

The preservation of transparency is seen in a photograph of a sample with a

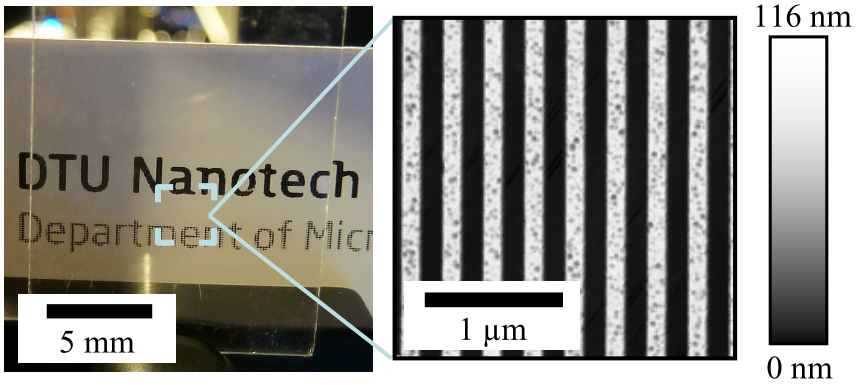

Figure 5.1: Photograph taken in ambient light, showing the transparency of the sample with the corners of the grating area marked. The right section shows an atomic force microscope (AFM) image of the grating.

grating, imprinted in a film of Ormocore on a glass substrate, see fig. 5.1. The grating has 355 nm period, a duty cycle of 50% and the lines are 120 nm deep. The possible beam paths for incident light on the gratings are illustrated in the drawing in fig. 5.2(a):

- light is guided in the glass substrate by total internal reflection (TIR)
- light is guided in the grating layer

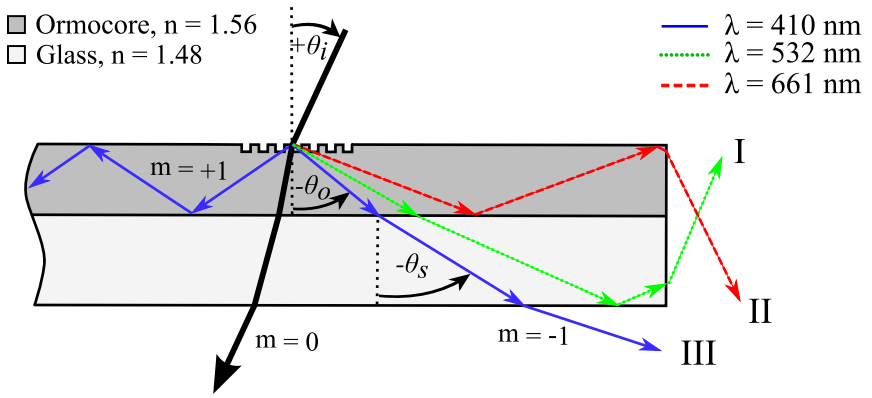

Figure 5.2: Illustration of the sample (not to scale) with beam paths for an incidence angle of 22°. λ = 410 nm is guided in the thin-film as +1 order, the -1 order is transmitted through the sample. λ = 532 nm is guided in the substrate (-1 order). λ = 661 nm is guided in the thin-film (-1 order).

- light is transmitted.

The first case occurs for incident light which is diffracted (by the grating) and refracted (at the thin-film - substrate interface) to greater angles than the angle of TIR for the *substrate*, causing the light to propagate almost lossless to the sample edge. The second case occurs when the angle of the diffracted light is large enough that TIR occurs at the *interface between thin-film and substrate*. The third case where the incident light is transmitted occurs for the 0^{th} diffraction order and for non-guided diffraction orders deflected by large angles.
Incident sunlight can be guided to the side by either of the two guiding modes, as shown in figure 5.3. Panel (a) illustrates the beam paths and panel (b) and (c) present a photograph of guided light in the glass. The two different guiding modes are clearly distinguished by the light which is seen from the side due to minor scattering on the glass surfaces and due to fluorescence of the thin-film. In the case of panel (b), the light is guided by total internal reflection (TIR) and the distance of the TIR spots can be used to deduce the propagation angle inside the glass. In the case of panel (c), the incidence angle and wavelength are phase matched with the grating period as a 2^{nd}-order Bragg grating[83] such that the light is guided as a waveguide mode in the thin-film which has higher refractive index than the substrate.
The conservation of momentum between the free space wave and the wave perturbed by the grating, causing redirection into guided modes, is expressed by the following equation which allows calculation of the propagation angles of the light.

$$n_{air} \cdot k \cdot \sin(\theta_{air}) + mK = n_{tf} \cdot k \cdot \sin\left(\theta_{tf}\right) \tag{5.1}$$

n_{tf} and n_{air} are the refractive index of thin-film and ambient medium respectively, θ_{air} the incident light angle, θ_{tf} the angle of the light in the thin-film, k the mode wavenumbers ($2\pi/\lambda_0$), K the grating wavenumber ($2\pi/d$, d is the period of the

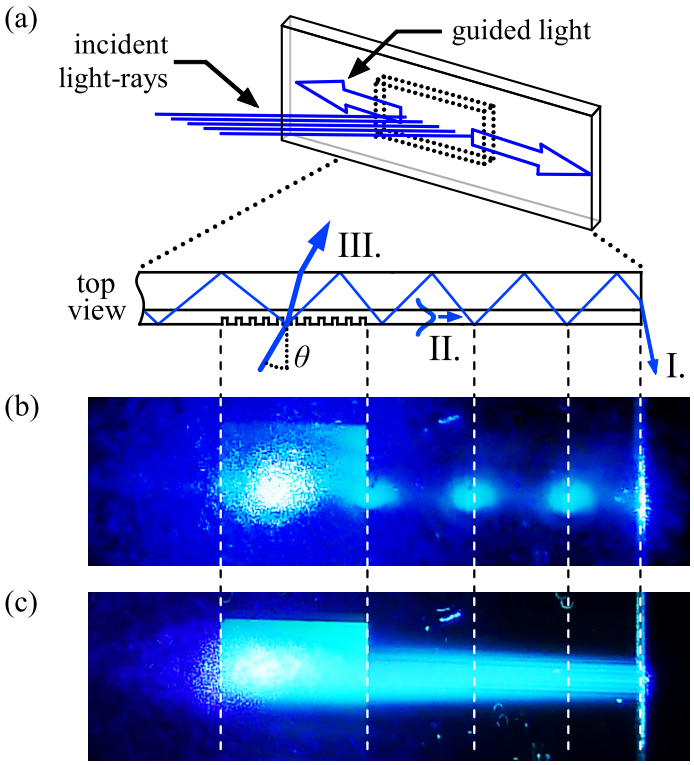

Figure 5.3: (a) Illustration of the operating principle and typical beam paths. (b) and (c) Photographs of a sample illuminated with a laser. The grating is visible in the center and guided light is visible as either (b) the scattering of TIR spots or (c) a waveguide mode guided in the Ormocore thin-film. Fluorescence in the Ormocore layer enables visualization of the 410 nm violet laser light which is partly upconverted to a blue-cyan color.

grating) and m the diffraction order number. Once the light is inside the thin-film the wave-nature can be omitted for a qualitative analysis and instead a simple ray-optics model can be used. The angle in the glass substrate is then given by Snell's law:

$$\frac{n_{tf}}{n_{sub}} \cdot \frac{\sin(\theta_{sub})}{\sin\left(\theta_{tf}\right)} \Leftrightarrow \theta_{sub} = \sin^{-1}\left[\frac{n_{tf}}{n_{sub}} \cdot \sin\left(\theta_{tf}\right)\right] \tag{5.2}$$

and the critical angle for guiding in the thin-film layer is given by

$$\theta_{tf,critical} = \sin^{-1}\left(n_{sub}/n_{tf}\right) \tag{5.3}$$

Using eqns. 5.1-5.3 and the Cauchy coefficients and refractive indices of thin-film and substrate shown in table 5.1, the range of incident angles which allow guiding in either the thin-film or the substrate are calculated. The values for guiding in the thin-film are obtained by setting θ_{tf} in eqn. 5.1 to -90° (see fig. 5.2 for sign definition of orders and angles) or to the critical angle for TIR between Ormocore and glass ($\approx 72°$). For guiding in the substrate, the critical TIR angle between glass

Material	Cauchy coefficients	$n_{410\ nm}$	$n_{532\ nm}$	$n_{661\ nm}$
Thin-film (Ormocore)	1.540, 0.0071 µm², $2.65 \cdot 10^{-4}$ µm^4	1.5917	1.5685	1.5577
Substrate (Borofloat)	1.495, 0.0045 µm², $-8.738 \cdot 10^{-5}$ µm^4	1.4826	1.4737	1.4688

Table 5.1: Cauchy coefficients and refractive indices for the three lasers used.

and air is -42.5°. Note that the values represent guiding to one side of the sample and that, due to mirror symmetry, guiding also occurs toward the other side with opposite sign of the angles. Within the ranges for thin-film guiding, light may couple to guided modes along the film. With a film thickness of 460 nm and TE polarized light, the waveguide is single-moded for visible wavelengths down to 400 nm (see e.g. Adams[84] eqn. 2.90). When the incident angle is aligned such that the diffracted angle is 90° (parallel to the waveguide surface), then light is coupled into a guided mode with effective refractive index n_{eff}. The incident angles which fulfill this condition are found by setting θ_o to 90° and n_{sub} to n_{eff} in eqn. 5.1.

Wavelength	Thin-film guiding range	Peak position	Substrate guiding range
410 nm -1 order	-25.9° … -19.1°	-23.8°	-19.1° … 8.9°
410 nm -2 order	45.9° … 55.8°	48.7°	55.8 … 90°
532 nm -1 order	-4° … 1.4°	-1.4°	1.4° … 29.9°
661 nm -1 order	17.7° … 23.2°	21.2°	23.2° … 59.5°

Table 5.2: Overview of incident angle ranges which support guiding in the substrate or thin-film and peak position of the guided mode.

5.2 Fabrication

Fabrication of the samples for experiments is done by nanoimprint lithography. Stamp and imprints fabrication procedures are outlined in detail in chapter 3.1 and 3.2. In brief, a stamp is fabricated by electron beam lithography and replication by imprinting is done with a transparent stamp into 460 nm thin films of Ormocore, spin-coated onto 0.5 mm thick Borofloat glass wafers. Finally, the wafer is cut into 15 x 15 mm^2 pieces with 3 x 3 mm^2 gratings located in the center.

5.3 Experiments

5.3.1 Measurement of redirection efficiency

The setup as described in chapter 4 is use to measure the light redirected to the edge of the glass as a function of the incident light angle. The sample is mounted on a motorized rotation stage and is probed by three laser beams with wavelengths of 410 nm, 532 nm and 661 nm, corresponding to the borders and center of the visible spectrum. The lasers are TE polarized, i.e. the E-field is parallel to the grating lines.
In order to measure the redirected light at the side of the sample, two detectors are available: A fiber, coupled to a spectrometer, is used for fast measurements of the intensity of the redirected light of the three wavelengths simultaneously, therefore suitable for development of a *qualitative* understanding of the coupling process. Alternatively a calibrated photodiode is used which has an active area of 10 mm^2, but is covered such that only a thin stripe of 0.5 mm width is exposed to the light and aligned in close contact to the glass edge. In this way all of the guided light is measured before it diverges out from the glass edge, but free-space reflections or diffracted orders are not measured. This method is suitable for *quantitative* measurement of the redirection efficiency as a percentage of the incident light ($\eta_{redir} = P_{redir}/P_{in}$, where P_{redir}/P_{in} is the redirected power to one side and P_{in} the incident power). Additionally, two cameras are installed which take color images of the glass edge and overview images of the sample. A drawing of the setup is presented in figure 5.4. The measurement, consisting of a plot of redirection

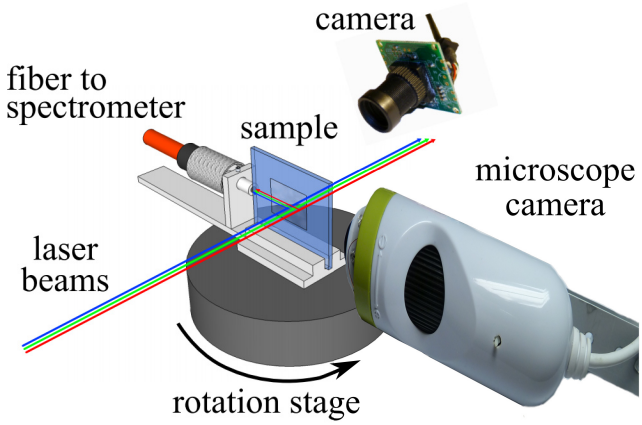

Figure 5.4: Drawing of the measurement setup used for the solar harvesting gratings.

efficiency vs. angle of incidence is shown in fig. 5.5. The different regimes illustrated in fig. 5.2 can be easily recognized and there is good agreement with the values in table 5.2. In the following the different guiding regimes are discussed for the example of the red laser (λ = 661 nm), shown in the upper curve of fig. 5.5. From 23° to 60° the maximum redirection efficiency is measured and this is due to

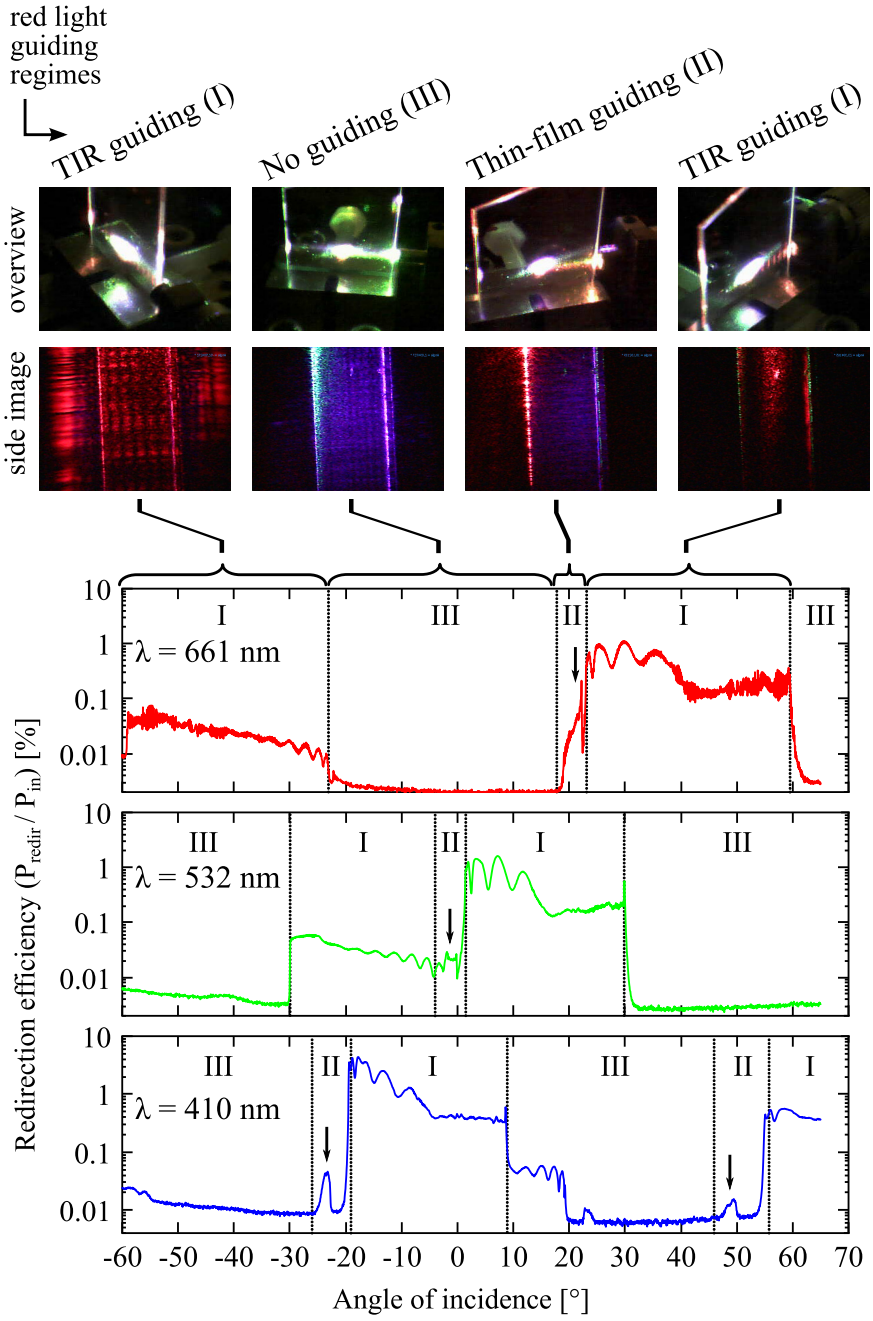

Figure 5.5: Measured intensities of light redirected to the sample edge. Images in the top row show pictures taken by a camera during measurement with the camera mounted behind the sample. The second row shows images recorded at the side of the sample by a microscope camera. The thin-film is located on the left side of the glass. The different guiding regimes are marked by roman letters I-III and the calculated positions of peaks due to thin-film guiding are marked by arrows.

substrate (TIR) guiding. The oscillations are a result of the TIR spot roving back and forth at the glass edge and varying the amount of intensity collected by the photodiode. Looking at the camera images, the right-most image of the overview camera shows red light redirected from the white spot in the center towards the right edge and multiple spots, originating from the reflections of the guided light at the surfaces can be seen. The image of the edge shows a spot of red light in the center of the glass. For incident angles larger than 60°, light does not couple into supported TIR modes and the collected signal drops substantially. Guiding in the thin-film is expected from 18° to 23° based on the ray-optics model. Since the waveguide is single-moded, coupling to a waveguided mode is only possible at an angle of 21°, clearly visible in the microscope image as a bright light in the region of the thin-film. Between 18 and -23 no red light is redirected, the microscope image shows TIR guiding of blue light and thin-film guiding of green light. Finally, for red light a broad range of redirection from -60° to -23° can be seen, which is light guided in the opposite direction of the detector and partially reflected back. Similar patterns are measured for green and blue light, each shifted by approximately 20° towards smaller angles where the shorter wavelength of blue light additionally allows the -2 diffraction order substrate guiding to appear at an angle of 54°. The thin-film guiding peak for green light is present at -1° but concealed by the light guided in the opposite direction in the substrate and backreflected. The peaks for blue light are clearly visible at -24° and 49° for the -1 and -2 diffraction orders, respectively and the peak positions correspond accurately to the calculated values which are marked by an arrow.
At large incident angles the curves (in particular the green curve) show increasing signal even though there is neither substrate nor thin-film guiding expected in these regions. This residual light is due to increased scattering as the size of the laser spot increases when the sample is rotated to larger angles. The shape of the curve is consistent with the expected increase in irradiated area, proportional to $1/cos(\theta)$.

5.3.2 Simulations

The ray-optics model which is used in order to determine the angles where redirection is possible cannot calculate a quantitative number for how much light is redirected. Therefore numerical simulations are conducted using the finite difference in time domain (FDTD) method. The 2D simulation consists of a TE polarized continuous wave normally incident on a grating in a thin-film with the same geometry as the fabricated devices. However, the substrate has a thickness reduced to only 10 µm in order to minimize the computational load. The results show the same three guiding regimes as observed in the experiments. Simulated detectors which integrate the propagating flux of electromagnetic energy are placed in the incident wave and at the left edge of the sample to determine the redirection efficiency. Direct comparison of the measured and simulated values is difficult due to scattering and diffraction causing a fraction of the narrow simulated wave to be incident at oblique angles on the grating. The simulated efficiencies (P_{redir}/P_{in}) of 0.01%, 0.2% and 0.6% for red, green and blue light, respectively, are

larger than to the experimentally measured values of 0.002%, 0.03% and 0.45%. While the agreement is good for TIR guided blue light, the simulated values for green light, being guided in the thin-film, and red light are significantly larger than in the experiment. The reason is expected to be light, that is originating form the interface between grating and plane glass, which radiates towards the detector (clearly visible in fig. 5.6(b)). The effect from this discontinuity is more pronounced in the simulations because here the area of the grating is much smaller than in the experiment.

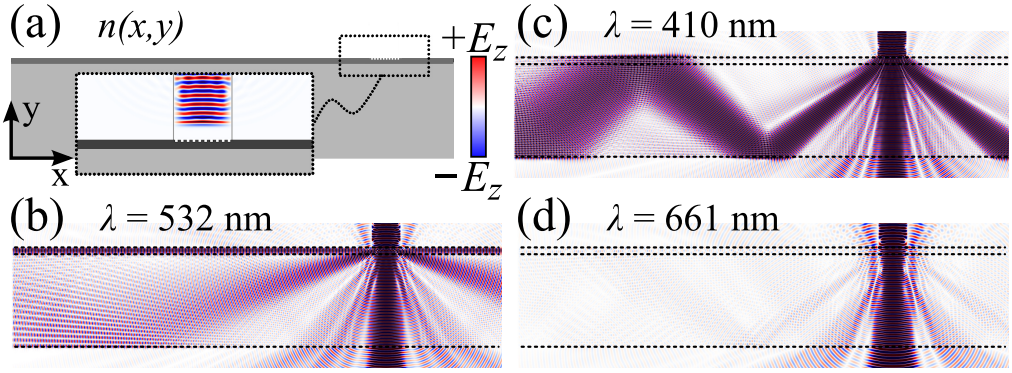

Figure 5.6: FDTD simulations of a TE polarized wave incident on the grating (355 nm period, 460 nm layer thickness, protrusion depth 120 nm), showing diffraction and propagation of the electric field amplitude. (a) Refractive index profile and the simulated wave just before impinging on the grating. (b) λ = 410 nm, light is guided in the glass substrate by TIR. (c) λ = 532 nm, light is guided in the thin-film layer. (d) λ = 661 nm, light is diffracted by the grating with almost zero guidance in the substrate and thin-film.

5.3.3 Re-outcoupling of guided light

From the time-reversal symmetry of Maxwell's equations it is clear that the grating coupler will also out-couple guided light. This situation is outlined in figure 5.7. The propagation angle of a TIR guided beam in the substrate is on average 58°, and

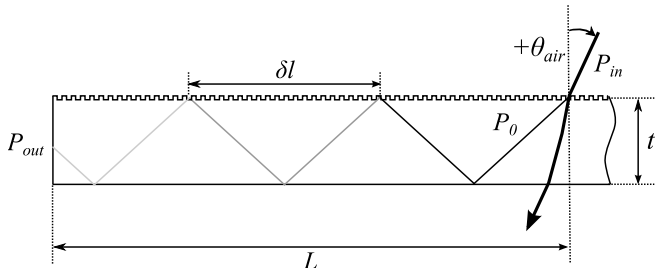

Figure 5.7: Simplified drawing of the light path, considering multiple interactions with the grating.

assuming a glass thickness of 5 mm, the beam will impinge on the grating every

16 mm. Each time the beam is incident onto the grating a fraction of its power is outcoupled and thus an exponential decay according to

$$P_0 = P_{in} \cdot \eta \tag{5.4}$$

$$\alpha = \eta / \delta l \tag{5.5}$$

$$P_{out} = P_0 \cdot e^{-\alpha \cdot L} \tag{5.6}$$

is expected. Here P_0 is the incoupled power, α is the loss per unit length and P_{out} is the output power. By using typical values of L = 500 mm (for a beam, incident in the center of a 1 m wide window), P_{in} = 100 W and assuming a diffraction efficiency η = 0.05 into the first order, the output power is 1.04 W, i.e. the loss during propagation after redirection is about 80%. This relation is also investigated experimentally by varying the position of a laser spot on a 10 mm long, 400 nm period grating and measuring the intensity of redirected 532 nm light. The result is plotted in figure 5.8 and verifies the expected exponential decay of guided light. Furthermore, the decay rate is clearly related to the incoupling angle and thereby the propagation angle inside the glass. Since the redirection efficiency depends on

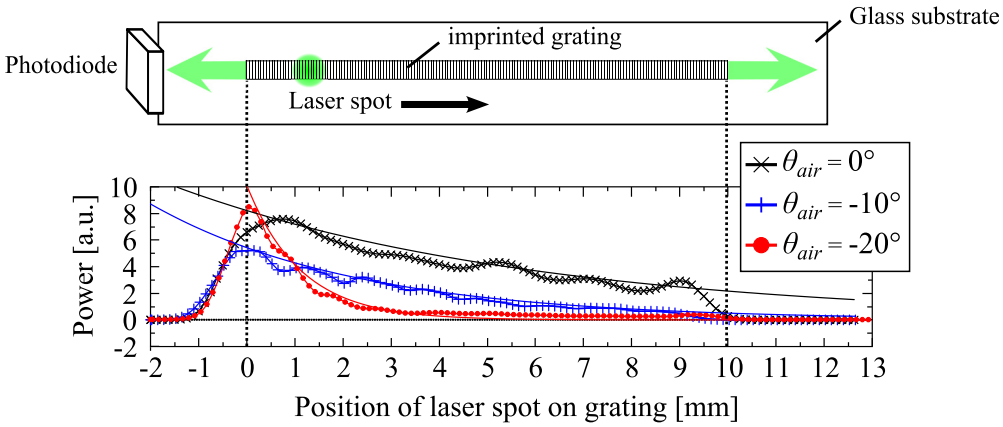

Figure 5.8: Measurement of the light intensity redirected to the side as function of position of the laser spot on a 10 mm long grating for three different angles of incidence, θ_{air}.

the angle of incidence it can not be assumed constant and a more detailed analysis would require FDTD simulations with a very large calculation domain, which is omitted here.

5.3.4 Reduction of angle-dependence

In order to reduce the angular dependence of the redirection efficiency the optical functionality of the grating coupler is enhanced by superimposing several periodicities. This photonic crystal (PhC) is constructed from many stripes of fixed gratings with 274, 355 and 441 nm period. These periods are designed for resonant incoupling at close to normal incidence. Every block of such three lines has random offset in order to reduce the regularity. An SEM image of the structure is shown in

figure 5.9.
Measurements of the redirection efficiency as a function of the angle of incidence are shown in figure 5.10. As a reference, also two samples with fixed periods of 355 nm (panel (a)) and 274 nm (panel (b)) are included additionally to the PhC sample shown in panel (c). The three samples are fabricated on the same wafer, to ensure that the film thickness, imprint depth, surface roughness etc. are comparable. The imprint layer is a 3 µm film of PMMA and the imprint depth is 120 nm. Comparing the results of the 274 nm period and 355 nm period grating,

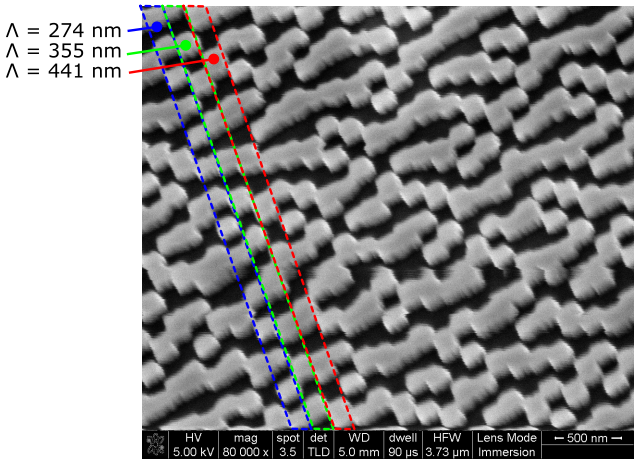

Figure 5.9: Grating with mixed periods

it is seen that 355 nm represents a good compromise between transparency (which requires small period) and efficiency. A period of 355 nm supports redirection orders for blue, green and red light within the range of -60°..60°. Although the 274 nm period grating has slightly higher efficiencies for blue and green light, the period is too small for diffraction orders for red light to exist. It was found that, in general, the peak efficiency is about twice as high for the samples in PMMA than for samples imprinted in 460 nm of Ormocore. This is expected to be caused by a better film quality of the PMMA layer which reduces scattering losses of the TIR guided modes. It is also noted that the 3 µm thick waveguide is highly multimode such that no distinct peaks due to thin-film guiding are observed.
The measurement of the PhC sample in figure 5.10(c) shows that the angular range for redirection is broadened by a factor of two (661 nm) up to three-fold (410 nm), in comparison to the limited, approximately 30° wide range seen in the fixed grating samples. This is explained by the combination of the three fixed period gratings being very closely localized at distances smaller than the optical wavelength which effectively leads to the generation of a range of superimposed periods. Compared to the 355 nm grating, the average efficiency, measured over the range from -65°..65° is comparable for blue light, reduced from 1% to 0.7% for green light and significantly lower for red light (1.1% to 0.4%). The reason is that due to the broadening of the redirection range, a part of this shifts out of the measurable range, in particular for the red light.

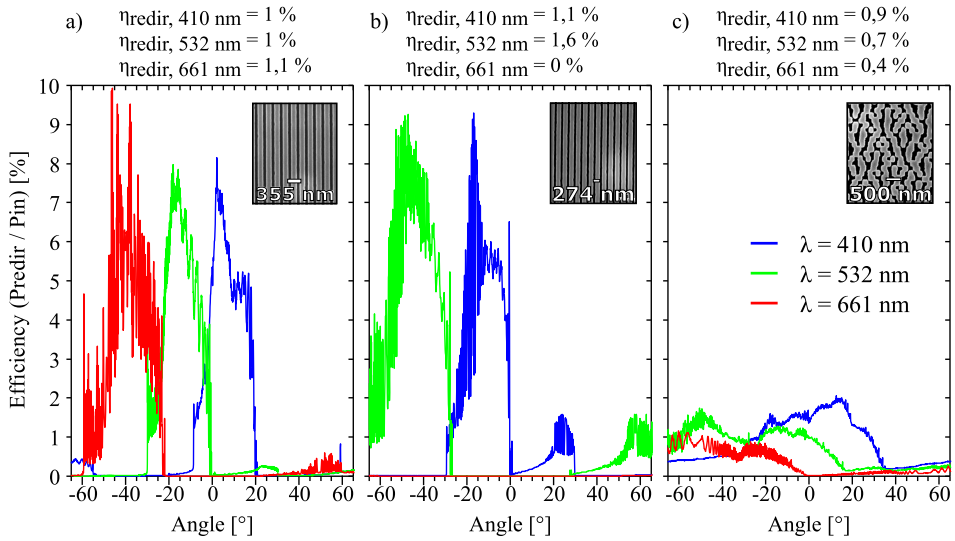

Figure 5.10: Measurement of redirection efficiency for different samples. The numbers stated as η_{redir} are the average redirection efficiencies in the range of -65°..65°. (a) 355 nm grating. (b) 274 nm grating. (c) photonic crystal

5.4 Discussion

The results show that it is indeed possible to combine the functionalities of transparency with light-coupling and guiding, because the photons guided in the waveguides do not interact with the photons transmitted through the glass. However, there is an inherent compromise between redirection efficiency and transparency. When the grating period is smaller than the optical wavelength, the mechanisms which reduce the transparency are scattering and diffraction into free-space orders, leading to both intensity loss and distortion/blurring of transmitted light. Provided that scattering is low and diffraction orders are either guided or propagate in free space at large angles, a high degree of transparency can be maintained in conjunction with average redirection efficiencies of 1% and peak efficiencies up to 10%. These figures will be reduced on large windows due to re-outcoupling of the light, when the guided light propagates on average over larger lengths of grating. However, for a beam guided by TIR, the number of reflections from the grating structured surface is reduced with increasing thickness of the glass. Considering the thickness of a typical window pane and the fact that TIR guided beams propagate under shallow angle, only few interactions with the grating occur during propagation towards the edge.
Measurements of photonic crystals, comprised of a combination of fixed period gratings, demonstrate how the redirection range can be extended in order to adjust the redirection characteristics to the local sun trajectories, direction of the building etc. When a more continuous light harvesting is required (e.g. in systems which work autonomous from the electricity grid) it may be necessary to use photonic crystals which compromises the overall efficiency but ensures constant electricity generation while the sun incidence angle changes during the course of the day.

Even though the efficiency is rather low, the cost of such a solar harvesting system may still be competitive with conventional solar cells. Considering an average efficiency of 1%, compared to the fraction of required solar cell area (4% for a 1 m^2 window, 2% for a 2 m^2 window), the cost/Watt is of the same order of magnitude compared to a solar cell covering the whole window.

5.5 Outlook

An important aspect about window-integrated solar harvesters as described above is the possibility to make the effect tunable. Various methods have been reported for tuning the efficiency of surface gratings, based on induced refractive index changes in a layer which covers the grating. This may be a key aspect in the realization of solar windows, as it could allow to switch off the redirection effect in exchange for higher transparency of the window. This functionality could be used to tune the efficiency to the level of sunlight or to use the redirection for implementation of additional functionality such as privacy windows. However, tunability is also very important for the overall energy generation of the device. Considering the situation outlined in figure 5.11, the solar harvesting window actually causes *higher* energy consumption in situations where the sunlight is not bright enough to lighten the room. This is due to the fact that the reduced lighting of the room from sunlight, due to redirection of part of the light to the solar cells, needs to be compensated by electrical lighting. Assuming an insolation of 100 W and optimistically chosen efficiencies of 20%, 50% and 50% for the redirection efficiency, light-to-electricity conversion efficiency and electricity to light generation in the light bulb respectively, additional 30 W need to be supplied from the grid, due to the presence of the solar harvesting window. Depending on the region, this may be a rather frequent situation over long periods of the year and could compromise the overall electricity generation of the device, i.e. tunability is required to be able to inhibit the redirection effect in such low-sunlight situations.

5.6 Conclusion

In summary, it is demonstrated that a transparent glass with imprinted sub-wavelength grating couplers performs dual functionality: transparency and redirection/guiding of light. Two guiding regimes in the thin-film and substrate layers are identified, both of which are explained by means of light being diffracted into modes with propagation angles below the TIR limit and are found to be in good agreement with experimental results. Up to 10% of incoming light can be redirected into guided modes at certain incident angles. Further interaction with the grating during propagation may reduce this efficiency by 80% for a typical window. Still, the high transparency of the gratings, due to sub-wavelength scale and the simplicity of the fabrication process make it feasible to use these gratings for solar harvesting. The superposition of fixed grating periods in the formation of photonic crystals may be used in order to tune the angle-dependence of the

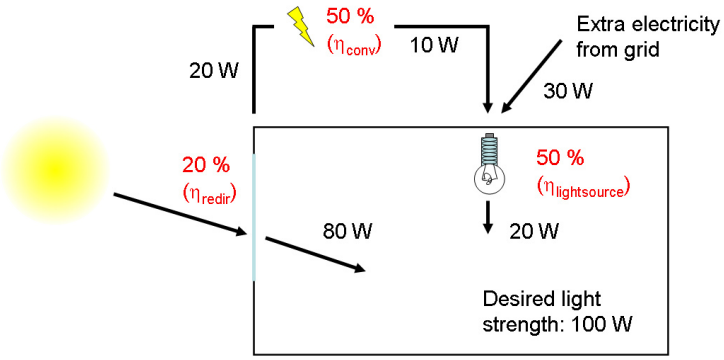

Figure 5.11: In the case that the sunlight is just as bright as it should be to light the room with a normal window, a solar window actually leads to additional electricity consumption. The values are very rough approximations, presented in order to convey the potential issue.

redirection to a specific application. Depending on the overhead of available sunlight, it may be necessary to include a tuning mechanism to the redirection effect.

6 Daylighting through nanostructured windows

In this chapter the application of disordered gratings for daylighting is discussed. Incident sunlight is redirected towards the ceiling by grating-microstructured window panes, such that a more homogeneous illumination of the room is achieved via diffuse scattering. Inevitable color dispersion due to diffraction is reduced by introduction of disorder into the periodicity of the gratings. This work was conducted in collaboration with Saint Gobain Recherche (France) where design, simulation and fabrication were done. AFM/SEM characterization and optical measurements were made at DTU and analysis of the results was done in cooperation.

6.1 Design and principle of operation

Windows with daylighting functionality facilitate interior illumination by redirecting natural sunlight through windows into the room,[85,86] thus reducing the amount of electrical lighting required. As outlined in the introduction chapter, microscopic daylighting structures, applied directly onto the glass are the preferred choice since these may retain some degree of vision through the window and do not alter the architectural design of the building.
Figure 6.1 compares the transmission of light into a room for three different types of windows. In panel (a) a standard, non-structured window pane is considered which simply transmits the incident sunlight without distraction. Panel (b) shows how the illumination can be improved by application of a regular surface diffraction gratings on the glass. In this case the zeroth order light is still transmitted, but in addition higher diffraction orders are redirected upwards, reducing glare and enhancing illumination further away from the window in the room via diffuse scattering from the ceiling. The grating period is 500 nm, corresponding to light with wavelengths of 410, 532 and 661 nm being redirected to angles of 19°, 33° and 55°, respectively. These wavelength-dependent redirection angles, inherent to any diffraction process, generate a colorful pattern when illuminated with white light, similar to a rainbow. In order suppress this color dispersion but still retain directionality of the redirection towards the ceiling a slight degree of disorder is introduced into the grating period[87–89] as shown in panel (c). The position of the peaks remains unaltered, but the angular range is broadened.

The design of such daylighting gratings is determined by the following requirements:

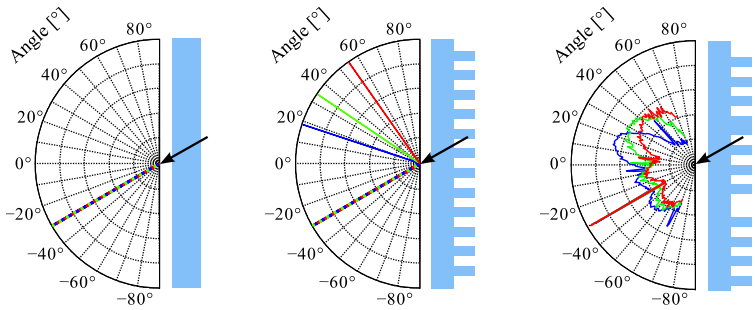

Figure 6.1: Graphs showing the angular distribution of light after passage through different types of window panes. (a) In a standard window the light passes directly through the window. (b) When gratings are applied on the window surface the light is diffracted into distinct diffraction orders. The diffraction angle is highly wavelength-dependent. (c) Gratings with added disorder broaden the diffraction angles and increase color mixing to white light, but still retain directionality of the redirected light

- High transparency of the window
- Desired daylighting efficiency
- No visible "rainbow effect"
- Feasibility for high volume fabrication
- UV light stability

In order to achieve a high transparency without distortions of vision through the window only two diffraction orders should exist, corresponding to the zeroth order, i.e. direct transmission and one additional order which contributes to daylighting. As a figure of merit for the daylighting grating performance, the efficiency is defined here as the ratio of the power diffracted above horizontal and the total transmitted power, i.e.

$$\eta_{daylighting} = \int_{0°}^{90°} I(\theta)d\theta / \int_{-90°}^{90°} I(\theta)d\theta \tag{6.1}$$

where θ is the angle of transmitted light and $I(\theta)$ the light irradiance. The efficiency depends on the incidence angle of the light and throughout this chapter a window facing directly towards the sun, with the sun having an elevation angle of 30°, is considered. In such a situation the sun's elevation is high enough such that the sun has significant intensity, yet low enough to cause glare far into the room. The daylighting efficiency should be large enough for a notable effect and the depth of the grating line is a design parameter which may be tuned to increase the efficiency.
Color divergence can be suppressed by implementation of disorder in the period,

for which the symmetry of the grating is broken and light from a particular wavelength is not diffracted into a sharp spot but distributed over a larger range, thus improving the mixing into white light.
The requirement for simple fabrication, combined with the demand to fabricate deterministic, aperiodic patterns dictates that self-assembly or interference lithography cannot be used. Therefore nanoimprint lithography is the preferred method, which however limits the possible structures to surface patterns. Another important constraint is the durability of the window coating which must sustain UV light exposure without degradation and yellowing over very long periods. This is currently not possible with organic materials, therefore fabrication is done in a sol-gel material which can be calcinated after nanoimprinting.
In the following the parameters which fulfill these requirements are derived. Figure 6.2 presents calculations of the diffraction angle of the -1^{st} and -2^{nd} order as a function of wavelength over the relevant visible range from 400 nm to 700 nm, at a 30° angle of incidence. Based on this data 400 nm period is chosen as the base period since larger periods achieve too small redirection angles. Even though a regular period 400 nm period grating does not redirect light with wavelengths larger than 600 nm, the disorder which is introduced causes redirection also for longer wavelength red light as will be seen later in simulations and measurements. Disorder is introduced by taking a fixed period grating as starting point and then

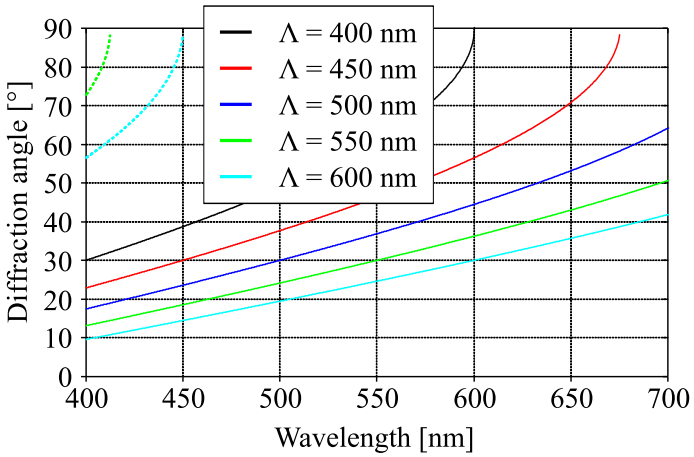

Figure 6.2: Diffraction angle as function of wavelength for gratings with fixed period Λ. Dashed lines indicate -2^{nd} order and solid lines -1^{st} order diffraction.

randomly, after M periods, inserting an offset of $-\Lambda/2$, $+\Lambda/2$ or zero as shown in figure 6.3(a). The amount of disorder is characterized by the M parameter and additionally also the disorder parameter, ξ, defined here as

$$\xi = 1/(2M)$$

The maximum disorder which can be achieved in this scheme for $M = 1$ corresponds to $\xi = 50\%$. The fact that the disorder cannot be larger is due to the fact that the duty cycle is kept constant to 50%. Furthermore the disorder

is also limited by the requirement that the diffraction should be directional and a too high disorder would approach an omnidirectional diffuser. Figure 6.3(b) shows four different realizations of disordered gratings which are investigated in detail in the following. The values of the disorder parameter are 12.5 %, 25% and 50% ($M = 4$, $M = 2$ and $M = 1$) at base periods of 400 nm. For comparison the 25% disorder is also investigated in a grating with 500 nm base period.

For calculation of the efficiency and redirection characteristics it is required to

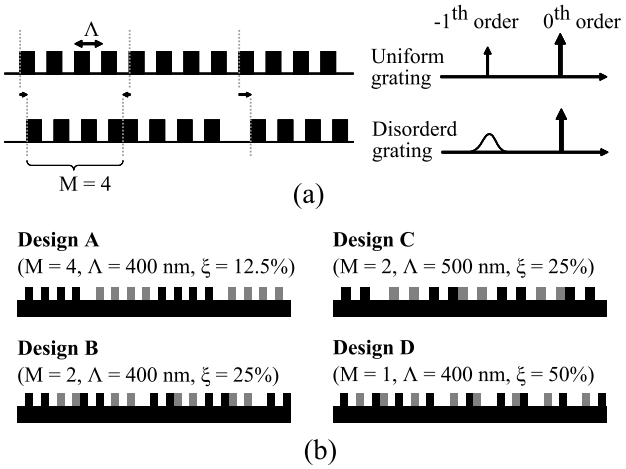

Figure 6.3: Design of disordered gratings. (a) Disorder is introduced by inserting a random shift after every M periods. (b) To-scale drawing of the four investigated samples. Blocks of M periods are drawn alternating in gray and black to illustrate the random shifts in the period.

do numerical RCWA simulations.[53,90] Since the RCWA method requires a periodic structure, a supercell of 100 periods, including the random disorder, is defined and simulated. since the disorder is random, the results vary with every simulation, therefore 20 individual simulations are averaged. Based on these simulations the data in table 6.1 is compiled, which investigates the daylighting efficiency for different values of the height of grating lines. A grating height of 350 nm results in highest efficiency and the aspect ratio of 1.75 is still manufacturable by nanoimprint lithography. If the aspect ratio was larger, there is a larger risk of grating lines collapsing.

Grating height	Daylighting efficiency
100 nm	2,40%
250 nm	14,30%
350 nm	26%

Table 6.1: Calculated daylighting efficiency of a 400 nm grating with M = 2 for different heights of the grating lines. The efficiency is averaged over the human eye spectral sensitivity.

6.2 Nanoimprint fabrication

In order to fabricate gratings with deterministic disorder, a direct-writing fabrication method is required since self-assembly or holographic approaches cannot be used to define arbitrary patterns. Therefore nanoimprint lithography is used, which also has the advantage that it can easily be up-scaled to larger areas. The dimensions necessary for daylighting applications also pose a challenge, requiring a period of 400 nm, an aspect ratio of $2 \cdot h/\Lambda = 1.75$, transparency and durability of the material. To fulfill these demands, the simple and low-cost SSGNIL[91,92] process is used to imprint nanometric patterns in a thin-film on glass. In particular, the chosen sol-gel material has a number of advantages: its optical properties are similar to glass, with a refractive index of 1.45, and it has a strong adhesion to glass substrates. Most importantly, it can be imprinted while not yet crosslinked and allows calcination, i.e. thermal decomposition of inorganic constituents after imprinting.

Though the process is similar to the description in section 3, there are some

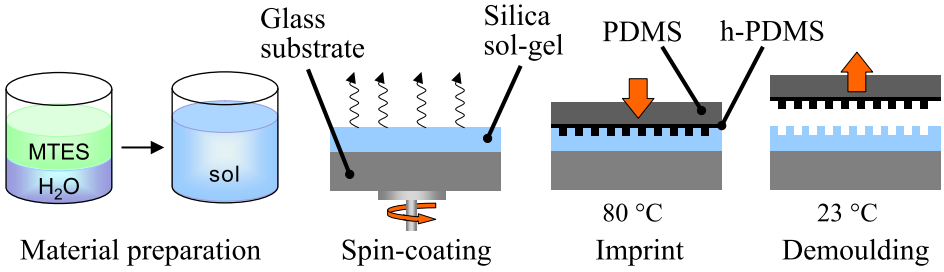

Figure 6.4: The fabrication process, consisting of sol-gel preparation, spin-coating of the thin-film, imprinting and demolding.

notable differences due to the different materials involved and requirements for high aspect ratio lines. In order to facilitate imprinting of these high aspect ratio gratings, the stamp is made as a two-layer structure:[93] The nanostructures are made in h-PDMS ("hard" PDMS) which can withstand pressure during imprinting, avoiding collapsing of the grating lines. The bulk of the stamp consists of flexible PDMS, allowing conformal contact between stamp and samples over large areas. In the following the general process sequence is outlined, detailed parameters are presented in appendix A.3.4. Further details of the SSGNIL process are described in ref.[94]

The silicon master stamp is fabricated by e-beam lithography with grating lines of 350 nm height (done at CEA-LETI, Grenoble, France). From this master the PDMS stamp is casted by pouring a thin layer of h-PDMS and vacuum degassing is used to remove possible entrapped bubbles. Then this first layer is cured at 60 °C for 15 min, followed by formation of the thick substrate layer by pouring flexible PDMS directly on the h-PDMS. Fabrication of the PDMS stamp is finalized by another thermal curing step for two hours.

The replication process of gratings (done at SVI CNRS/Saint-Gobain, Aubervilliers

Cedex, France) into silica sol-gel from the PDMS stamp consists of mixing of a sol, spin-coating, imprinting, and finally demolding, as illustrated in figure 6.5. The sol, a mixture of methyltriethoxysilane (MTES) and hydrochloric acid (HCl, pH = 2.5) is stirred for several hours and spin-coated to produce an 800 nm thin film on a smooth glass substrate. Next, the PDMS stamp is imprinted into the spin-coated film such that the cavities of the stamp are filled. Elevated temperature of 80 °C causes crosslinking until the sol-gel reaches a solid state. The temperature is then decreased to ambient temperature, the load is relaxed and the stamp is removed from the surface.
Aside from the ease of structuring silica sol-gel via nanoimprint lithography, an important, additional advantage of the material is that pure silica nanostructures can be obtained by annealing it after cross-linking at 500 °C in oxygen atmosphere.[94] This not only increases the mechanical strength of the silica layer but further promotes adhesion to the glass substrate. However, it should be noted that structural shrinkage takes place during annealing since all the organic constituents of the material are removed.[95] Consequently, the refractive index, period, and height of the grating lines are affected and must be considered during the design phase. In order to simplify the simulations of the fabricated grating structures, and to ease comparison of the optical measurements with the simulations, the annealing process has been omitted in this study such that the high fidelity between grating and master is maintained.
The replicated grating samples are characterized by atomic force microscopy (AFM) and scanning electron microscope (SEM), see fig. 6.5(a) and (b), where both the height and period of the patterns are found to be replicated with high fidelity. However, shrinkage of the gel during cross-linking introduces some edge roundness. Figure 6.6(a) shows a photograph of the final sample that was used for

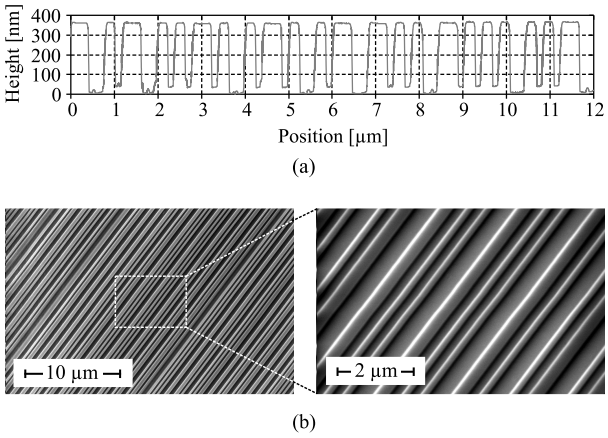

Figure 6.5: (a) AFM-generated profile of a disordered grating (M = 2). (b) Top view SEM image of a disordered grating (M = 2).

measurements. If larger areas need to be structured a step-and-repeat nanoimprint process may be used. In such a case, a pattern of approximately 1 cm^2 size is

repetitively imprinted as shown in figure 6.6(b). Upon careful observation, the lines between the individual imprints are visible, but imprinting with very accurate overlap has been demonstrated.[96]

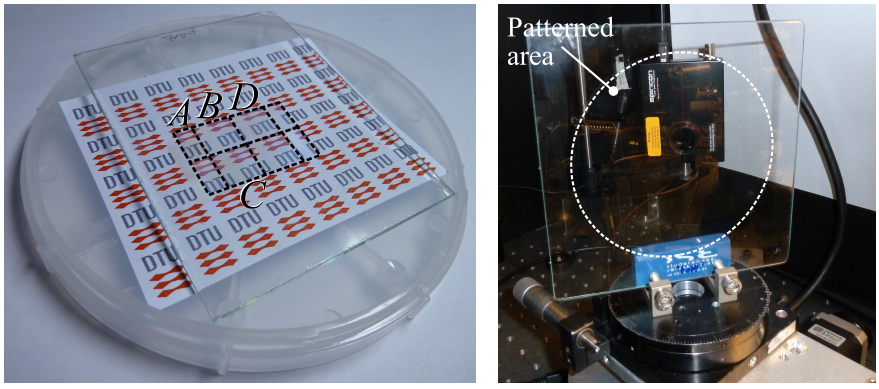

(a) (b)

Figure 6.6: (a) Photograph of the sample used for measurements.The position of the gratings is indicated by dashed lines and the different designs are labeled with letters corresponding to those in fig. 6.3. (b) Photograph of sample fabricated using step-and-repeat nanoimprint. The master was fabricated by CEA-LETI (Grenoble, France), step and repeat imprint by AMO (Aachen, Germany), nanoimprint by SVI CNRS/Saint-Gobain (Aubervilliers Cedex, France).

6.3 Measurements

In order to characterize the optical daylighting performance of the gratings, the angular resolved transmitted diffraction efficiency is measured using a setup as described in section 4 and in particular as shown in fig. 4.1(a). See fig. 6.7 for a definition of the diffraction angles with respect to the grating. The sample is probed by laser beams under 30° angle of incidence and the diffraction pattern on a half circle around the sample is recorded by a camera rotating around the sample. Even though the gratings are designed for application with incoherent, spectrally broad sunlight, the use of lasers for the measurement offer the possibility to quantify the diffraction effect for distinct wavelengths (410, 532 and 661 nm) and polarization states. Figure 6.8 shows a measurement of the transmitted diffracted light for the sample with 500 nm period and 25% disorder. The 0^{th} order, located at an angle of -30°, has been attenuated by a factor of 1000 for better visibility of the diffracted light. The intensity of the red, green and blue measurements are normalized and therefore not directly comparable, yet the figure still gives a reasonable qualitative representation of the daylighting effect for all three wavelengths. For 410 nm light the angle of maximum efficiency is close to 15°, for 532 nm light at 30° and for 661 nm light at 45°. The angular spread of the peaks is larger than 30° and therefore yields a more homogeneous daylighting effect than a fixed period grating could achieve. Since coherent laser light is used

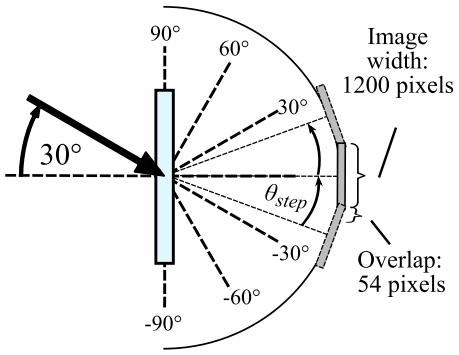

Figure 6.7: Angle definitions for the measurements of the daylighting gratings. The drawing corresponds to the measurement setup as seen from top view. 0° is defined as normal to the grating, positive angles correspond to light that would be diffracted towards the ceiling in a daylighting window. The camera rotates around the sample and captures the diffraction pattern with a small overlap between individual images, such that the total image can be reconstructed.

for the measurement, the diffraction patterns also show fringes due to thin-film interference in the silica layer, see the enlarged region in fig. 6.8. These fringes would not be visible for incoherent sunlight, where instead a continuous light distribution would be present.

For a more detailed analysis of the diffraction efficiency, line traces are extracted from the images in the angular direction. Since the efficiency depends on the polarization of the light, both TE and TM polarization are measured and then averaged in order to mimic unpolarized sunlight. The result is shown in fig. 6.9 for the four different grating geometries under 410, 532 and 661 nm light illumination, plotted together with the results obtained by the numerical RCWA simulations as described above. Again, it should be noted that the high frequency variation in the data is not caused by noise, but interference due to Fabry-Pérot resonances. Since this effect will not be present under sunlight illumination, it is not included in the simulation model. For the benefit of easier comparison between measurements and simulated data, a 0.1° wide moving average filter is used to suppress these resonances.

6.4 Discussion

The general trend of the curves shows clear qualitative agreement between simulation and experiment, in particular validating the SSGNIL process as adequately capable of replicating the nanoscale period and high aspect ratio grating structures. As expected, the sample with the lowest degree of disorder (design A, $M = 4$, $\xi = 12.5\%$) shows the most prominent peaks in the diffraction spectrum. Apart from several broad peaks, also very sharp peaks are observed (e. g.

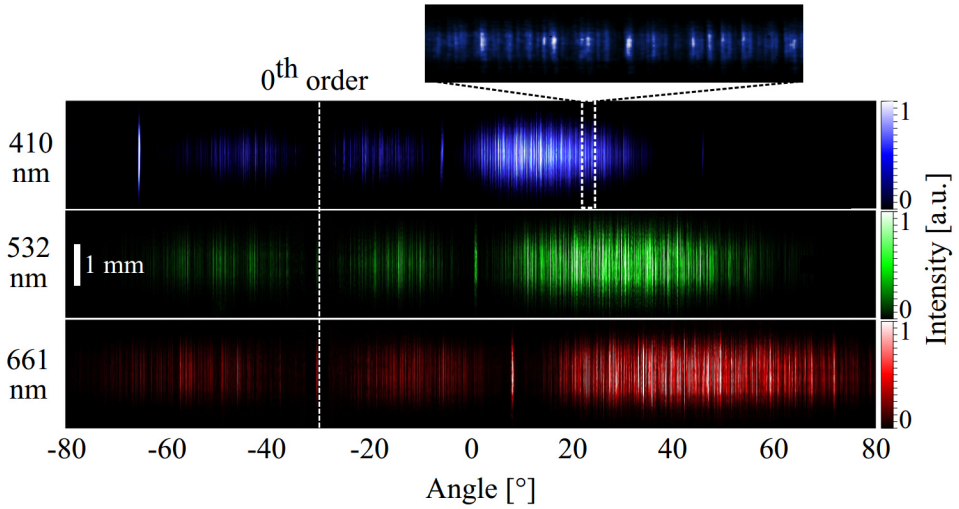

Figure 6.8: Transmitted diffraction pattern of a grating with Λ = 500 and M = 2, measured separately for 410 nm, 532 nm and 661 nm TE polarized light at 30° angle of incidence (artificial color). The zeroth order, located at -30°, has been attenuated by a factor of 1000 for better visibility of the diffracted light.

at -5°, 19° and 48°). The positions of these sharp peaks coincide with the diffraction orders of a hypothetical grating of uniform $M \cdot \Lambda = 800nm$ periodicity, indicating that the peaks are introduced by the randomization method. By increasing the disorder (design B, $M = 2$, $\xi = 25\%$), the number of peaks is reduced, such that the light is redirected into significantly smoothened, broader maxima and a single sharp peak. The comparison between the base periods of 400 nm and 500 nm shows that the longer period causes the maxima to separate less and move to smaller angles, similar to a uniform grating. When the disorder is increased further to 50% (M=1) the redirected light distributes evenly over the range of -25° to 75°, for all the three wavelengths. Since the randomization occurs after each period, no sharp peaks exist in this case. Fig. 6.9 also shows for each of the four gratings a photograph of the diffraction pattern when the grating is illuminated with white light from a xenon lamp. Here it is seen that design A shows a rainbow effect since the redirection of the different wavelengths does not overlap. In design B the maxima are broad and homogeneous, however the rainbow effect is more pronounced due to the diffraction angle of the sharp peak being wavelength dependent (located at 0.1°, 9.2° and 18.5°). The most prominent color divergence is seen in design C with its larger period of 500 nm, especially at high angles where blue light is hardly diffracted to, but a significant amount of red light is present. Finally, sample D shows broad redirection without sharp peaks and therefore yields a highly homogeneous white light diffraction pattern, making this sample most suitable for daylighting.
The daylighting efficiency $\eta_{daylighting}$ is calculated from the measurements and

summarized in Table 2. Typically for all samples, the highest efficiencies of approximately 30% are achieved with blue light. The efficiency is lower for red and green light (3% - 15%) which is, however, not a problem, since there is often a lack of short wavelength light in indoor lighting.[97] By adjusting the period from 400 nm to 500 nm, it is possible to increase the efficiency for green light up to 21% and red light up to 10%. Doing so, of course, reduces the amount of light in the zeroth order, leading to a decisional compromise between transparency and daylighting effect.

Even though the simulated shape of the curves is closely reproduced in the

Period [nm]	ξ [%]	Efficiency [%] (meas.) 410 nm	532 nm	661 nm	Mean	Efficiency [%] (simul.) 410 nm	410 nm	532 nm	Mean
400	12,5	29,5	11,6	3	11,4	48,6	29	5,7	28,0
400	25	33,4	11,9	6	11,8	46,7	26,6	10,1	26,0
500	25	31,3	20,7	10,2	20,3	43,4	32,3	18,7	31,7
400	50	28,7	15,7	8,2	15,5	42,3	26,5	14,6	26,1

Table 6.2: Measured and simulated daylighting efficiencies of the samples. The mean value is weighted with the spectral sensitivity of the human eye, assumed as 0.012, 0.925 and 0.053 for 410, 532 and 661 nm, respectively.[98]

experiments, the efficiency of the measurements is 40-60% lower than predicted by the simulations. This deviation is attributed to two factors. First, fabrication deficiencies, where incomplete replication of thin grating lines are observed, and AFM measurements reveal line roughness and variation in grating heights. The fabrication factors can be overcome by fine-tuning the imprinting parameters. Second, mechanical damage of the gratings after fabrication decreases the overall efficiency. In order to overcome this problem the mechanical stability of the silica film can be increased by the thermal annealing process as mentioned in section 6.2. For daylighting applications, the nanostructures could be protected from mechanical damage by positioning them on the inside of a double glazing.
The measurements indicate that the efficiency is mostly independent on the disorder, pointing to the use of varying the degree of disorder to tune the angular distribution of the light without affecting the efficiency. Accordingly, this enables the scheme to fulfill the requirements of specific applications, determined e.g. by room size, purpose or trajectory of the sun. As a result, two major problems that exist for daylighting applications have been solved: 1) fabrication of optical nanostructures in a UV-stable material rather than polymer films, and 2) suppression of the "rainbow effect" via the use of disordered gratings.

6.5 Conclusion

In conclusion, nanoscale disordered gratings are demonstrated to enable controlled diffraction of light into broad distributions over large angular range, thus adding new optical functionality to transparent substrates. This functionality is particularly useful for enhanced daylighting in window panes. It is shown that

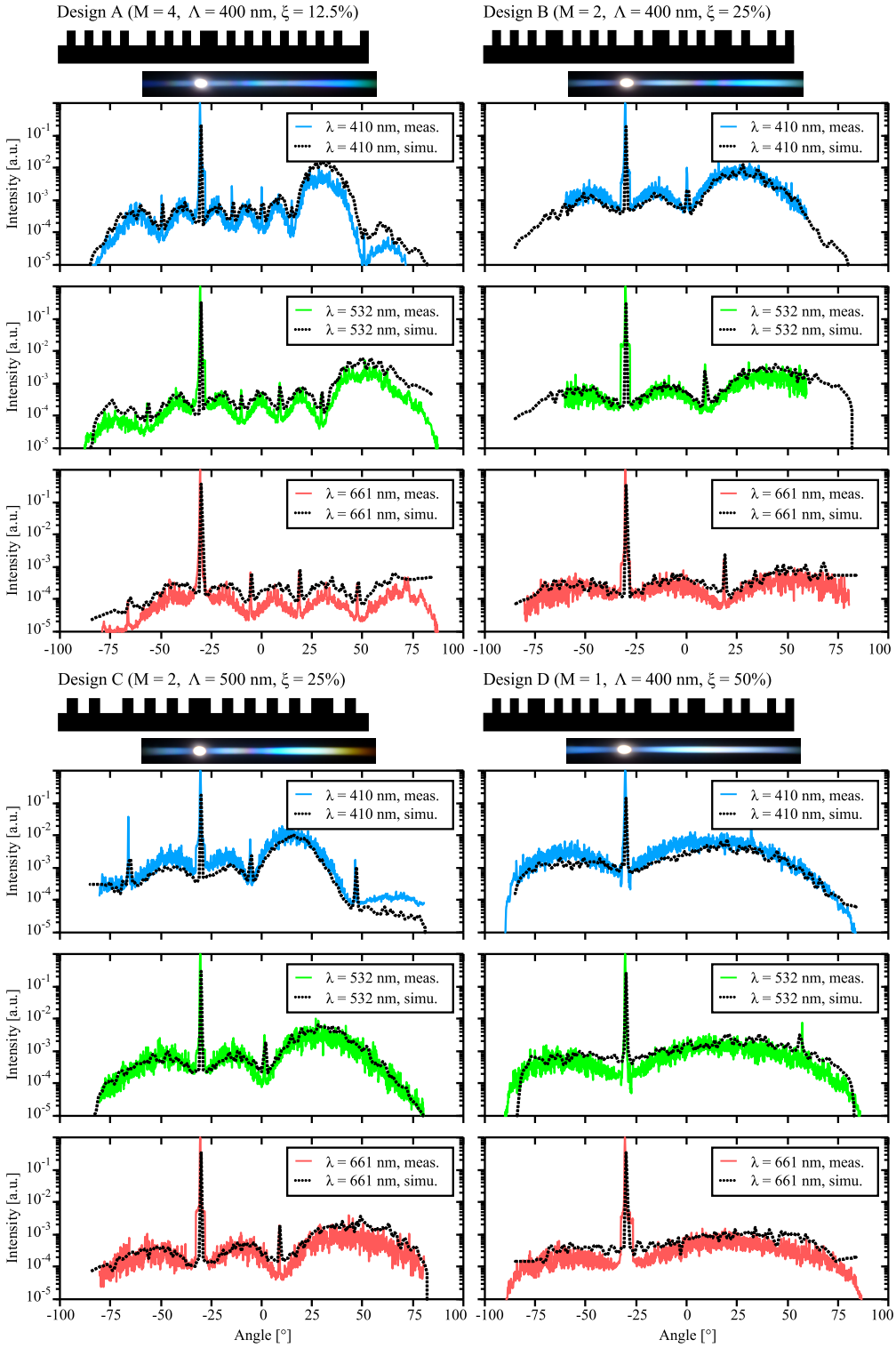

Figure 6.9: Curves showing the measured and simulated diffraction results for the four investigated samples at 410, 532 and 661 nm. For each of the four samples, a drawing of the grating and a photograph of the diffraction pattern when illuminated with white xenon light is shown above the plots.

the fabrication of these gratings is feasible by sol-gel nanoimprint lithography, which combines the advantages of low-cost, high quality and large area nanoscale patterning with favorable material properties of pure inorganic silica for long-term UV-light stability. The optimal parameters for disordered gratings applied in daylighting windows are determined by numerical RCWA simulations, namely 350 nm height and 400 nm period. Gratings with various degrees of disorder are investigated, and comparing the measurement results with simulations confirms that the diffraction characteristics of the disordered gratings can be predicted. Average measured daylighting efficiencies for 500 nm gratings are 20% and for 400 nm 11% to 16%, depending on the amount of disorder. A disorder of 50% is found to yield considerable reduction of color dispersion to yield a diffraction pattern that appears white. Since the degree of disorder has only small influence on the efficiency, the disorder can be modified to tailor the diffraction between widely distributed patterns and more directional diffraction if some color dispersion is acceptable. This feature renders the disordered gratings well suited to daylighting, but may also be an attractive feature for other applications that require customizable light redirection over broad angular range.

7 Tunable Microchip Dye lasers

In this chapter a tunable microchip dye laser is presented. The laser is based on a photonic crystal resonator, covered by a dye doped liquid crystal waveguide. Electric field induced reorientation of the liquid crystal molecules is used to tune the laser wavelength. Such lasers have dimensions of a few square millimeters and can be fabricated extremely cheap, thus they are suitable for applications in integrated lab-on-a-chip systems.

7.1 Physics and operation principle

The design of the tunable dye laser for lab-on-a-chip analysis systems is based on the following considerations: It should be cheap and simple to fabricate in large quantities, i.e. the structures must be compatible with nanoimprint lithography. Tuning of the laser wavelength should be controlled electrically over as large a wavelength range as possible, ultimately limited only by the gain spectrum of the laser dye. Finally, the laser should be pumped optically from above by a free-space beam with relaxed alignment requirements. In this way different lasers on a larger chip could be addressed by moving the position of the pump spot.
Based on these requirements, a laser design is chosen which combines the advantages of the lasers presented ref.[41] and,[39] namely low threshold, despite free-space perpendicular pumping, and electrical tunability. Low threshold is achieved by means of a multifunctional photonic crystal resonator which enhances coupling of pump light from above into the plane of the chip, thus effectively increasing the absorption length. Tunability is achieved by means of liquid crystal with electrically tunable refractive index. A drawing of the laser is shown in figure 7.1(a). The central element is the rectangular lattice photonic crystal with dual functionality: First it acts as a DFB reflector which provides feedback to the laser and locks the laser wavelength based on the optical path length between the protrusions. Second, the photonic crystal is designed such that pump light incident from above is redirected into light guided in the plane of the laser. The thickness of the gain medium is below 500 nm in order to allow only a single optical mode and based on this distance only a fraction of the pump light is absorbed. The redirected light however may be fully absorbed during propagation over several hundred micrometers.
The photonic crystal is patterned in glass and the laser gain medium is a dye-doped liquid crystal layer which covers the photonic crystal. A lid is used to contain the LC film, with the thickness being defined by SU-8 spacer blocks.
Since the resonant wavelength of the resonator depends on the optical path length,

a refractive index change in the LC layer, induced by reorientation of the LC director via an electric field, is used to tune the laser wavelength. Figure 7.1(b) illustrates two different alignment states of the molecules.
The choice of a dye-doped liquid crystal as gain medium, versus a solid state dye-doped polymer with LC cladding is motivated by the fact that liquid crystals have higher refractive indices than typical polymers. Therefore the laser mode will be localized in the liquid crystal and a large overlap between the mode area and the gain medium is preferable for low threshold lasing.

For an understanding of light propagation in multi-dimensional periodic

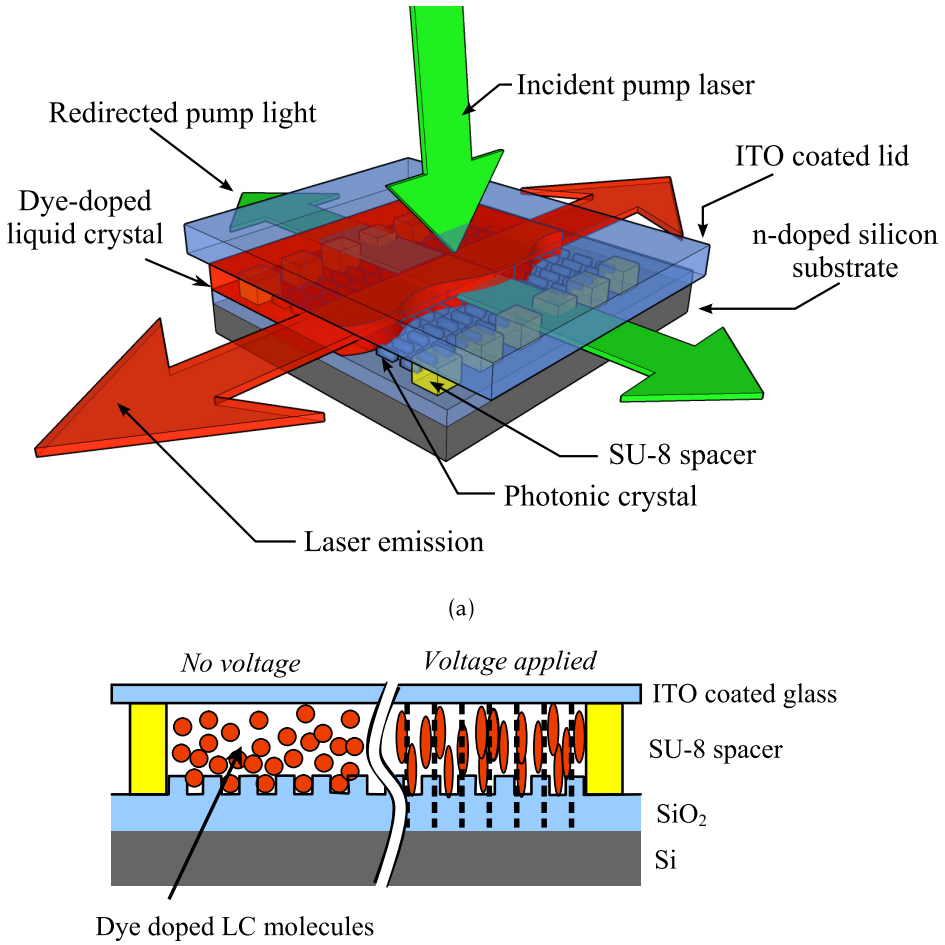

Figure 7.1: Drawing of the tunable dye laser. (a) Illustration of beam paths, pump light is redirected into the plane of the PhC resonator. Laser light is emitted in the direction of the short lattice constant of the PhC. (b) Side view drawing of LC molecule orientation with and without applied voltage. As the LC molecules change orientation the refractive index changes which tunes the optical path length and thereby the laser wavelength.

structures like photonic crystals, a useful tool is the band diagram, plotting the

frequencies which are allowed to propagate at different directions in the crystal. The band diagram of a laser with lattice constants of 360 nm and 200 nm is shown in figure 7.2. This band diagram is calculated by the effective index method

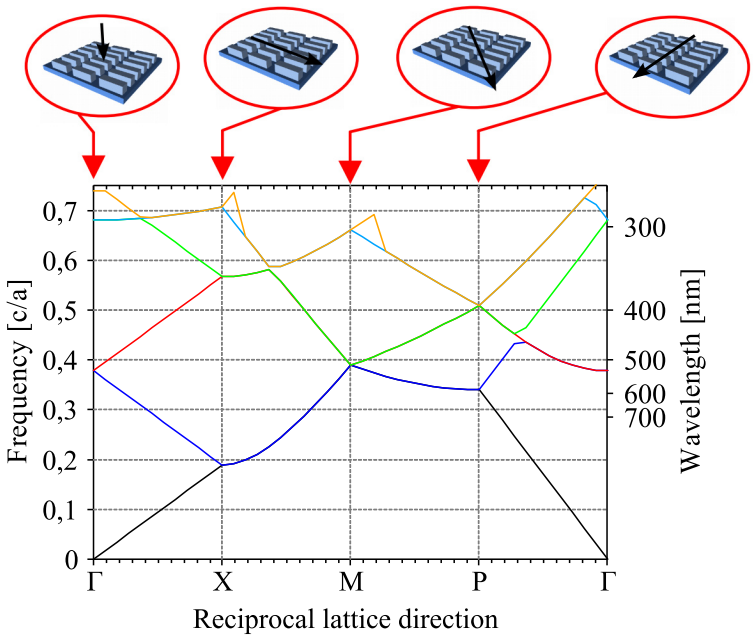

Figure 7.2: Band diagram of the PhC-LC laser. Each colored trace corresponds to an optical mode and the mode's frequency is given on the y-axis in units relative to the crystal's short lattice constant a. The corresponding wavelength, for a crystal with a = 200 nm is given on the right y-axis. The reciprocal lattice directions labeled on the x-axis correspond to the directions shown in the sketches on top.

as described in chapter 2.2.1. For the operation of the dye laser two reciprocal lattice points are of particular importance. The Γ point corresponds to light propagation perpendicular to the surface, i.e. incident pump laser light. The optimum incidence angle, which couples pump light from free-space into a guided mode in the Γ-X direction is found in the vicinity of the Γ point at the band with frequency corresponding to the pump wavelength of 532 nm. The wavelength of the dye laser wavelength is subject to two constraints: First, the wavelength must be within the gain spectrum of the laser dye such that the mode can be amplified. Second,the mode on which the laser will lase is determined by the band with the lowest group velocity, since these photons achieve more amplification during their slow propagation inside the laser cavity. A low group velocity $v_g = d\omega/dk$ corresponds to bands with vanishing slope. Such a point is located at the P-point, close to a wavelength of 600 nm and this is the region where the laser operates. Since there are two bands at the P-point with wavelengths close to 600 nm, lasing does in general occur on these two bands. If there are defects in the crystal, additional modes may start lasing. Furthermore it should be noted that, due to the crystal symmetry, lasing occurs in two opposite directions along the Γ - P reciprocal

lattice vector.
The laser wavelength is basically fixed by the photonic crystal lattice, but if the refractive index of the liquid crystal is changed, the constructive interference due to reflections from the many periods of the photonic crystal, will shift to a different wavelength, therefore the laser wavelength is modified by tuning of the refractive index via reorientation of the LC molecules. Initially, the nematic phase LC molecules align along the grooves of the PhC structure and tilt towards vertical alignment under an applied electric field. The refractive index change causes the bands to shift vertically, but the point of lowest group velocity still remains at the P-point.

7.2 Fabrication

The PhC-LC lasers are the only device described in this thesis which are not fabricated by nanoimprint lithography but instead written directly by e-beam writing in order to enable more rapid design iterations. This is feasible since the area of the nanopatterned PhC is small (1.8 mm^2 / laser). A process based on imprinting would however be possible if required, since the PhC is a simple surface structure without undercuts. The fabrication process is very similar to the process which is used for the NIL stamp fabrication as outlined in sect. 3.1. For the detailed recipe the reader is referred to appendix A.3.5.
The lasers are fabricated on n-doped silicon wafers which serves as conductive substrate. A 4.4 µm thick wet oxide is grown, acting as a cladding for the waveguide mode to prevent light from being absorbed in the silicon. The PhC pattern is written by e-beam lithography and etched 140 nm deep into the oxide by reactive ion etching. Subsequently a 330 nm thin layer of SU-8 is spincoated and the SU-8 spacers are defined by e-beam lithography. The area of the SU-8 spacers is approximately 10 mm^2 / laser, but the e-beam writing time is still very short since only low resolution is required and the clearing dose of SU-8 is as low as 12 $\mu C/cm^2$ (compared to approximately 220 $\mu C/cm^2$ for high resolution ZEP520A resist). Figure 7.3 shows SEM image of the photonic crystal etched in to the oxide and the SU-8 spacers.
For final assembly an ITO coated glass lid is placed on top of the SU-8 spacer and clamped mechanically to the laser substrate. The oxide layer has to be removed at an area away from the actual laser area such that a voltage can be applied to the conductive silicon substrate. Three methods are investigated for the removal. Etching in hydrofluoric acid (HF) reliably removes the oxide layer, but even though the PhC is protected by a tape enclosure, fumes from the HF also attack the PhC. A second method is to remove the oxide with sand paper, which quickly exposes a large area, however it does create dust particles and electrical contact may be inhomogeneous. Finally a focused Nd:YAG laser with pulse energy of approximately 400 µJ can be used to ablate the oxide. This process only removes small areas and therefore also creates little amounts of dust. In most cases the sandpaper is used due to the simplicity of the method. As a last step the dye-doped liquid crystal is mixed from 5CB and Pyrromethene 597[70] (1 wt%). A droplet of

the dye is dispensed at the lid such that it fills the resonator by capillary forces. The lid and exposed silicon substrate are connected to a voltage source (function generator) by copper tape.

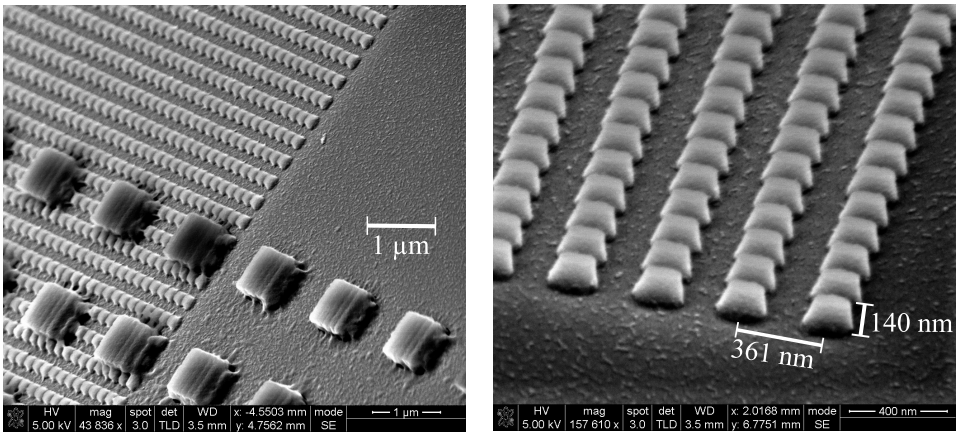

Figure 7.3: SEM images of the laser resonator. (a) Overview image, showing the photonic crystal resonator and the SU-8 spacer. (b) Detailed view of the photonic crystal resonator. The height of 140 nm is measured by AFM.

7.3 Measurement setup

Optical characterization of the lasers is done by pumping through the transparent top electrode using a frequency doubled Nd:YAG laser, emitting 10 ns pulses with an energy of 200 µJ. Figure 7.4(a) shows a drawing of the measurement setup, which allows to control the angle of the pump laser from the top and measurement of emitted laser light via an optical fiber, connected to a spectrometer. Figure

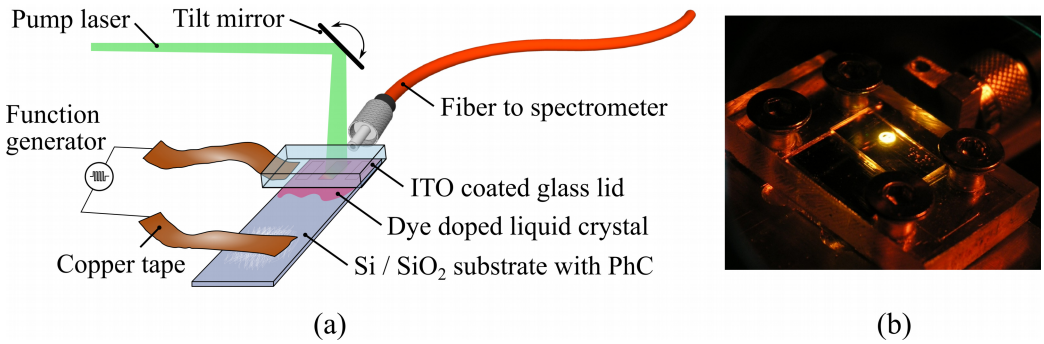

Figure 7.4: (a) Drawing of the measurement setup used for characterization of the dye lasers. (b) Photograph of dye doped liquid crystal laser in operation (without electrodes connected). The sample is photographed through an edge-pass filter which blocks the green pump laser light.

7.4(b) shows a photograph of a dye laser laser in operation, emitting orange light. Being photographed through a long-pass filter, the pump light is visible only by the intense round fluorescence spot.

7.4 Experiments

The dye laser emission spectra are observed in figure 7.5. Panel (a) shows the emission when the pump laser angle is not optimized to resonant coupling into the PhC plane. Accordingly, laser emission occurs at the fluorescence maximum. Panel (b) and (c) show laser emission with resonant pump angle, forcing the laser emission to the wavelength defined by the PhC. The lasing peaks occur 50 nm away from the dye fluorescence maximum, suggesting high lasing efficiencies and broad device flexibility. The ratio of the laser peaks to the fluorescence maximum is over 10 dB, comparing favorably with other similar 1D grating devices[39] and showing that the 2D PhC enhances the resonant pump interaction with the dye gain medium. Furthermore a clear electrically induced wavelength shift is observed when a voltage is applied. Unfortunately, due to bad electrical contact it is only partially possible to achieve electrical contact at all, so no in depth experiments of the laser wavelength as function of voltage are available.

In order to estimate the maximum tuning range in a simple way the temperature of the liquid crystal is changed and the lasing characteristics are observed. The results of this experiment are shown in figure 7.6. As the temperature is increased, the laser emission for the three oscillating modes is blueshifted. At low temperatures the liquid crystal molecules are aligned parallel to the surface, so the laser wavelength is determined by $n_\perp$. With increasing temperatures the alignment becomes more disordered, such that the light more and more sees the average refractive index of $n_\perp$ and $n_\parallel$. At 35 °C the liquid crystal changes phase to the isotropic phase and only minor change in lasing wavelength is observed above this temperature. The wavelength difference is up to 9 nm (mode 1) and considering that electrical tuning reorients the molecules such that the refractive index goes to $n_\parallel$, the maximum expected tuning range should be twice as large as the tuning range in the temperature experiment, i.e. 18 nm.

7.5 Discussion

The experiments show that a dye doped liquid crystal laser can operate with strong emission peaks, despite the scattering and random nature of the LC material. Electrical tuning is shown to be feasible, but not very controllable in the present experiment. This is attributed to technical problems: The mechanical clamping of the lid does not provide a reliable way to define a laser cavity of accurate and homogeneous thickness. If the thickness varies over the resonator area several modes could lase and upon changing of the LC refractive index the laser would hop from one set of modes to another, rather than continuous tuning. Another problem is the quality of the electrodes. In the present design the electrodes are connected

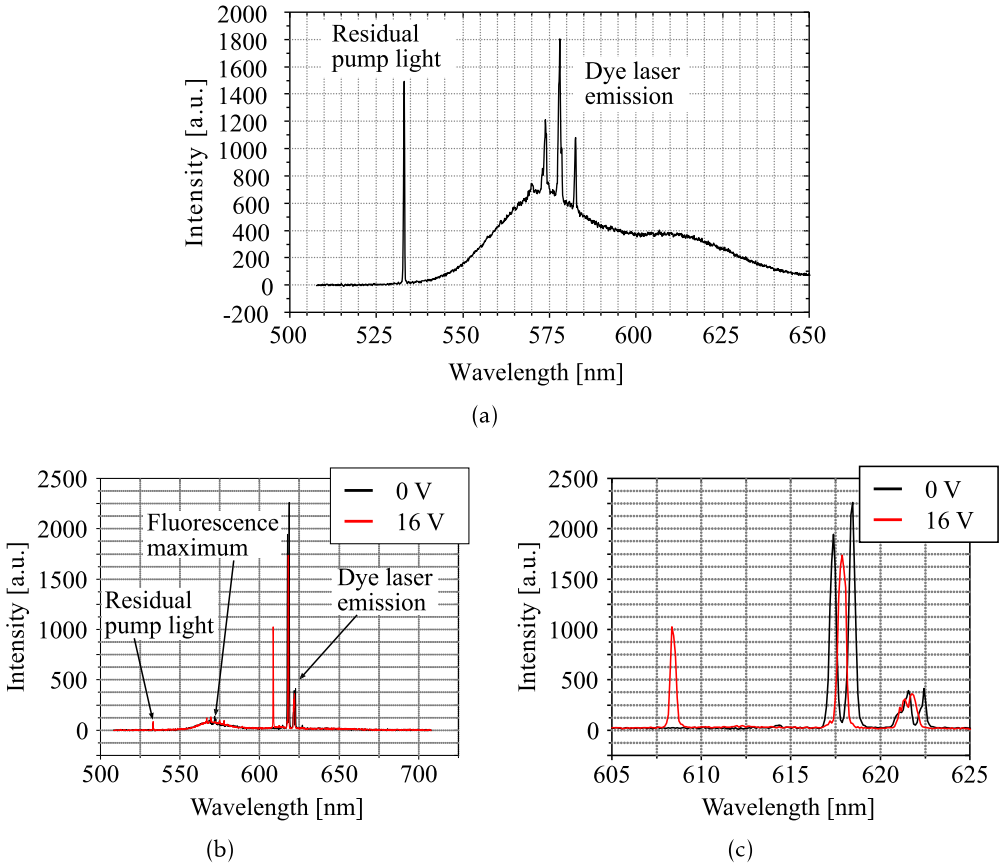

Figure 7.5: Laser emission spectra. (a) Emission without an applied voltage, including the signature of the pump source due to pumping from a de-tuned angle.. (b) Spectrum with matched pump angle. (c) Close-up of the lasing peaks. The black (dotted) trace shows the spectrum without applied voltage, the red (solid) trace the shifted spectrum while voltage is applied.

by copper tape, which provides a poor contact, in particular in combination with the sanded oxide layer. An improved design would therefore be based on a proper bonding process between substrate and lid. The oxide layer should be etched on large areas prior to fabrication of the nanostructures and a reliable electrical connection to the lid is required. These measures make the fabrication process more complex, however they appear to be required in order to accurately operate and tune a highly non-linear device such as a laser.

For a better understanding of the tuning process it would also be beneficial to investigate the alignment of the liquid crystal on the rectangular photonic crystal. Parallel alignment of the LC along the long axis is expected and supported by the experimental data, however not fully verified. A transparent substrate should be used to test the LC alignment via white light transmission with the sample between in crossed polarizers.

The tuning potential is verified by measurement of the laser wavelength as a

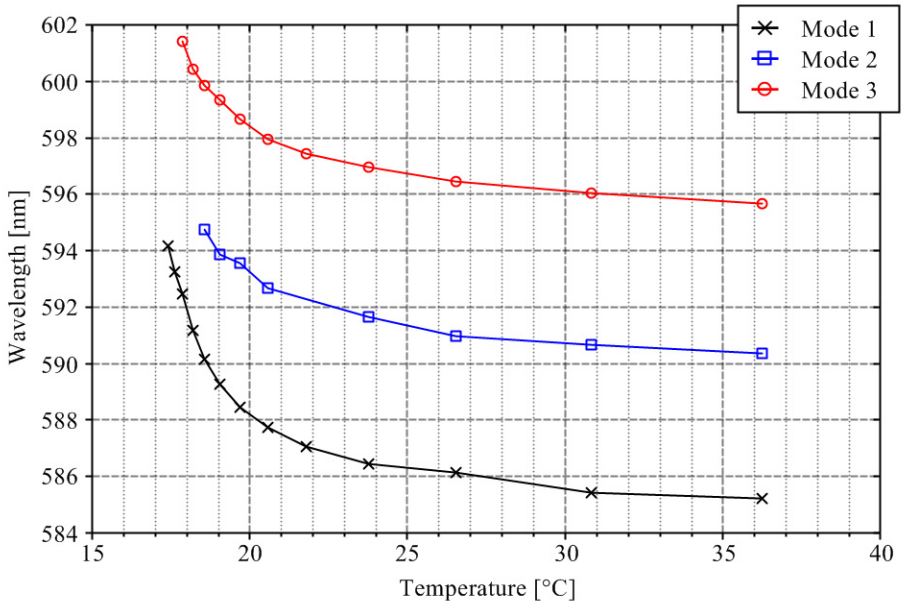

Figure 7.6: Tuning of the laser wavelength by changing the liquid crystal temperature.

function of temperature, which also affects the effective refractive index, similar to reorientation of the LC molecules by an electric field. In this way a maximum tuning range of 18 nm is predicted, however it has to be considered that the mode profile of the laser mode also depends on the refractive index. In this regard the tuning range is expected to be limited to where the laser mode has sufficient overlap with the photonic crystal and the liquid crystal layer remains a single mode waveguide. Furthermore, the refractive index change also affects the optimum pump angle, such that it may be necessary to readjust the pump angle during tuning or to pump the laser with a slightly divergent beam of higher intensity.
Opposed to the other devices discussed in this thesis the laser is not transparent. If however, a transparent laser was required, the silicon substrate could be replaced by ITO coated glass. The transparency would be limited by the absorption of the laser dye, but depending on the application, e.g. in a multi-layer lab-on-a-chip system it would be possible to observe layers below the laser by using an observation wavelength which is not absorbed by the dye.

7.6 Conclusion

In conclusion, a tunable laser with a multifunctional PhC resonator is presented. The tunability is achieved by incorporating LC to a PhC device and applying an electric field. The PhC strongly enhances pump interaction with the gain medium. The simplicity of the laser device and possibility for cost-effective fabrication make the lasers suitable for optical analysis in lab-on-a-chip systems.

8 Transparent photonic crystal projection displays

In this chapter a transparent, fully integrated and electrically modulated projection display is presented. The device is based on light guiding through a thin liquid crystal layer, and redirection of the guided light out of the chip plane by sub-wavelength gratings. In this way it is possible to integrate projection displays into transparent devices, thus enhancing the functionality beyond pure transparency.

8.1 Principle of operation

The principle of operation of the display device, consisting of a rectangular piece of glass, is shown in fig. 8.1(a). Light from an external laser source is focused onto the edge and propagates inside and along the transparent chip. At specific locations on the chip, micron-scale rectangular areas, filled with sub-wavelength gratings, are defined. These gratings act as picture elements (pixels), selectively out-coupling light at an angle perpendicular to the glass surface, and an entire projected image may then consist of many individual pixels. Here the concept is presented by considering three gratings (pixels) of 250 x 250 µm size, arranged in a row. Modulation of the outcoupling process is achieved by application of a voltage across the gratings via transparent electrodes. The electrodes are connected to a larger pad at the side to enable local addressing of the voltage.

Figure 8.1(b) illustrates the operating principle and the optical paths in greater detail. The device consists of a substrate (Borofloat glass, n = 1.48, 500 µm thick) and a thin film (n ≈ 1.6, 610 nm thick) with imprinted gratings (corrugation depth 120 nm). A liquid crystal layer of 600 nm thickness covers the gratings and the device is sealed by a Borofloat glass lid (500 µm thick). Since both the liquid crystal layer and the thin film each have higher refractive indices than the glass substrate, they form a primary optical waveguide for the guided light. However, the spot size of light focused by a microscope objective at the sample edge is much larger than the thickness of the core layers. Accordingly, the entire chip, including substrate and lid, is "flooded" with light that is guided by total internal reflection at the glass/air interfaces. This secondary waveguide continuously "refills" the lossy (due to scattering and out-coupling) primary waveguide. The direction of in-coming and out-going light is governed by equation 8.1.

$$n_{LC}\frac{2\pi}{\lambda}\cdot\sin(\theta_{in})+m\frac{2\pi}{\Lambda}=n_{SU8}\frac{2\pi}{\lambda}\cdot\sin(\theta_{out}) \tag{8.1}$$

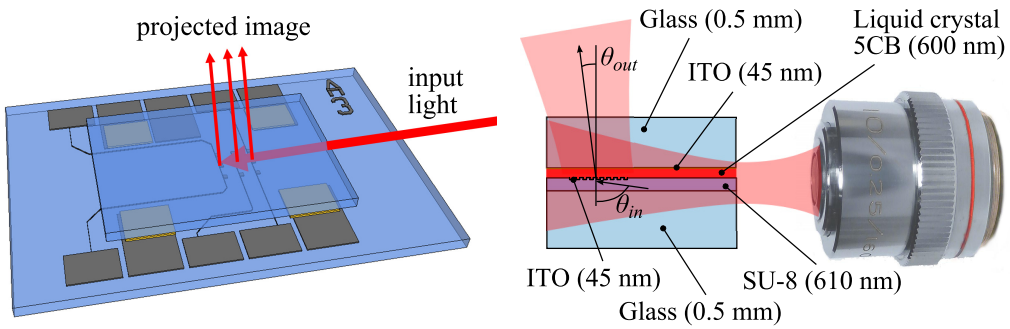

Figure 8.1: (a) Principle of operation for the projection display. Light enters from the side and is controllably out-coupled perpendicular to the device plane at specific locations. (b) Detailed side view drawing of the light propagating inside the device and out-coupled by a grating. The liquid crystal layer enables electrical modulation of individual pixels.

where n_{LC} and n_{SU8} are the refractive indices of the layers, m the diffraction order, λ the free-space wavelength of light and Λ the grating period. θ_{in} and θ_{out} are the angles of the in-coming and out-coupled light, respectively. By using the fixed values $m = -1$, $\theta_{in} = 90°$ and $\theta_{out} = 0°$, the required grating period for perpendicular out-coupling is determined.
The redirection effect is demonstrated in figure 8.2, where microscope images of gratings with different periods, illuminated by white light from the side, are shown. Redirection of narrow wavelength ranges upwards to the objective is observed, with the wavelength being determined by the grating period.

If a full-color display, operated by mixing of blue, green and red light is

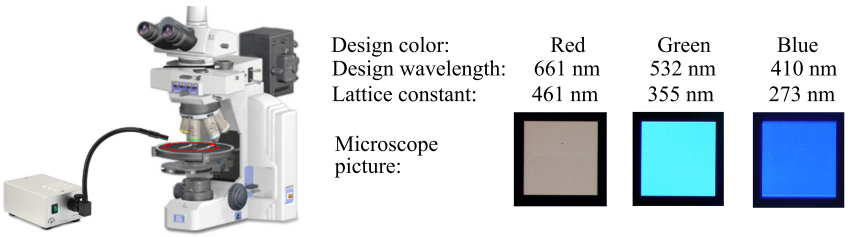

Figure 8.2: Optical microscope image of gratings with periods optimized for red, green and blue light redirection, illuminated with white light from the side. The grating redirects a narrow part of the spectrum upwards through the microscope such that the gratings appear close to the designed color.

desired, a single grating is not sufficient as it will diffract light of the "wrong" color to non-perpendicular angles, causing a significant penalty in image quality. This situation is illustrated in fig. 8.3(a). Instead, one grating for each color is required, and the illumination lasers must only be switched on if the gratings of

the corresponding color are actuated, as shown in fig. 8.3(b). This scheme has two limitations: First, a higher control frequency is required, since the color is mixed in time and color mixing must occur faster than the response time of the human eye. Furthermore, a larger fraction of the chip is covered with gratings, without benefit for the image resolution. Fig. 8.3(c) presents an alternative, where the individual gratings are stacked on top of each other. When the smallest period grating is at the top position, light outcoupled from gratings below is hardly affected by the upper gratings, since these appear with sub-wavelength period.

The tunability of the redirection effect is based on the anisotropy of the

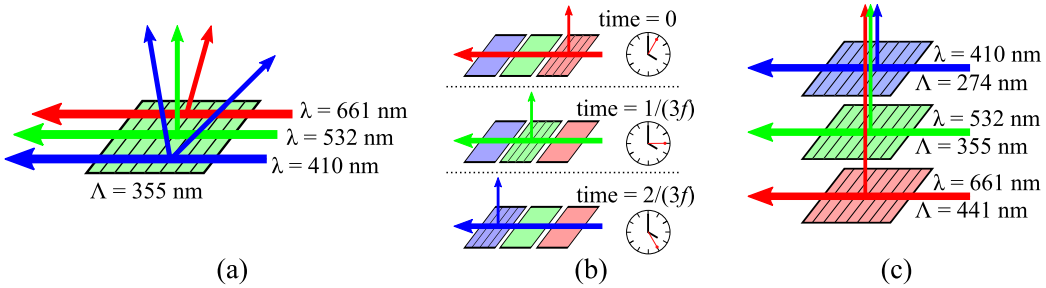

Figure 8.3: (a) A single fixed-period grating can not be used for perpendicular outcoupling of several colors. (b) Instead, a single grating for each color is required, with time-sequential switching of the gratings and the lasers. (c) A more compact approach for a full color display is realized when gratings with color-specific periods are stacked on top of each other, with the smallest period grating on top.

LC molecules. n_{LC} is not a simple scalar but a tensor and depending on the polarization of the light with respect to the orientation of the molecules (director $\vec{n}$), the refractive index varies between approximately $n_{\perp} \approx 1.5$ and $n_{\parallel} \approx 1.7$. The electric field which is applied over the electrodes is used to control the orientation of the molecules and thereby change the refractive index of the grating superstrate. If the refractive index of the LC is matched to the refractive index of the grating there is no phase-shift occurring in the grating and the diffraction efficiency goes to zero. If the refractive index contrast is increased, the diffraction efficiency also increases and enables redirection of light. In the following, two different electrode designs and their implications on the electro-optic behavior are discussed.

8.1.1 Electrode design

Two different electrode designs are investigated as shown in figure 8.4, with and without applied voltage. Panel (a) shows a design where both electrodes are located on the bottom glass which is advantageous for simple fabrication. In the off-state the director points perpendicular to the surface, this alignment is achieved by using Ormocore as imprint material and an FDTS coating for modification of the surface energy on the Ormocore film and the lid (cf. sect 2.5.1.1). Since a grating would counteract this alignment, a photonic crystal with holes is used as optical element for redirection of the light. In this case TE polarized light experiences the refractive index $n_{\perp} \approx 1.5$. The electrodes are placed next to each side of

the photonic crystal such that the electric field lines align parallel to the sample surface. Upon application of a voltage the molecules orient along the electric field and TE polarized light senses the refractive index $n_{\|} \approx 1.7$. For TM polarization, the situation is opposite ($V = 0 \rightarrow n_{LC} \approx 1.7$; $V > V_{th} \rightarrow n_{LC} \approx 1.5$).
Alternatively, the electrodes are placed above and below each pixel, see figure 8.4(b). In this case a grating instead of a photonic crystal is used and no FDTS coating is required, since the molecules align to the surface structure. When a voltage is applied, the molecules align perpendicular to the surface, i.e. the electro-optic behavior is reversed compared to the planar electrode configuration. The top/bottom electrode design achieves higher fill factor because the electrodes do not consume extra space next to the pixels and faster response times are possible since the electric field is much stronger over the short distance between lid and substrate. However, the transparency is reduced due to the double total ITO thickness and fabrication is more complicated since an electrical connection between lid and substrate is required.

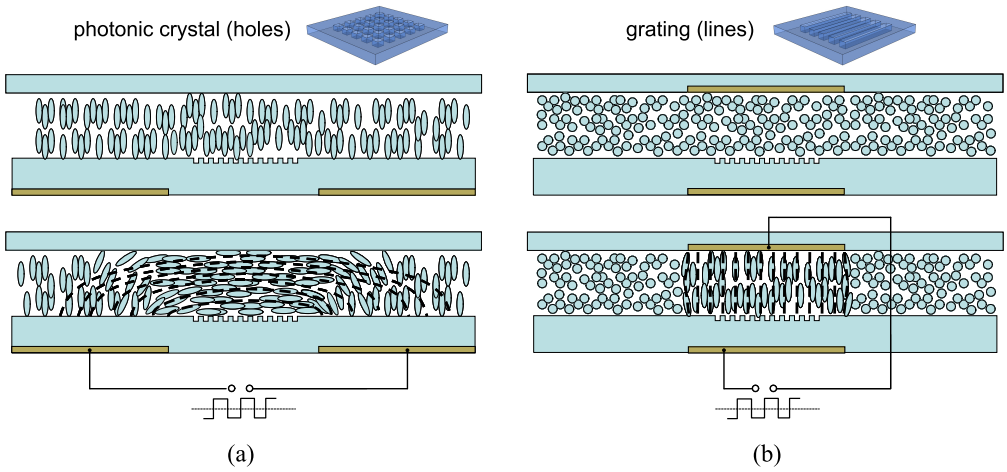

Figure 8.4: (a) Display based on planar electrodes and photonic crystals. Alignment in the off-state is achieved by chemical surface treatment. (b) Display based on top/bottom electrodes and gratings. Alignment in the off-state is achieved by the grating's surface structure.

8.2 Fabrication

The devices are fabricated on 10 cm glass wafers and the photonic crystals are imprinted into a 610 nm layer of Ormocore or SU-8. See sect. 3.1 for a description of the stamp fabrication, sect. 3.2 for a description of the imprint process and appendix A.3.6 for detailed process parameters. The stamp contains the nanostructures (photonic crystals or gratings) as etched protrusion and in some cases also waveguides as a shadow mask. The nanostructures are mechanically embossed while the larger waveguide structures are optically cured through the transparent stamp.

After imprinting, the electrodes are deposited and the display is assembled with a lid and liquid crystal as shown in fig. 8.5(a) for the case of planar electrodes and fig. 8.5(b) for top/bottom electrodes. The pattern of the electrodes and contact pads on

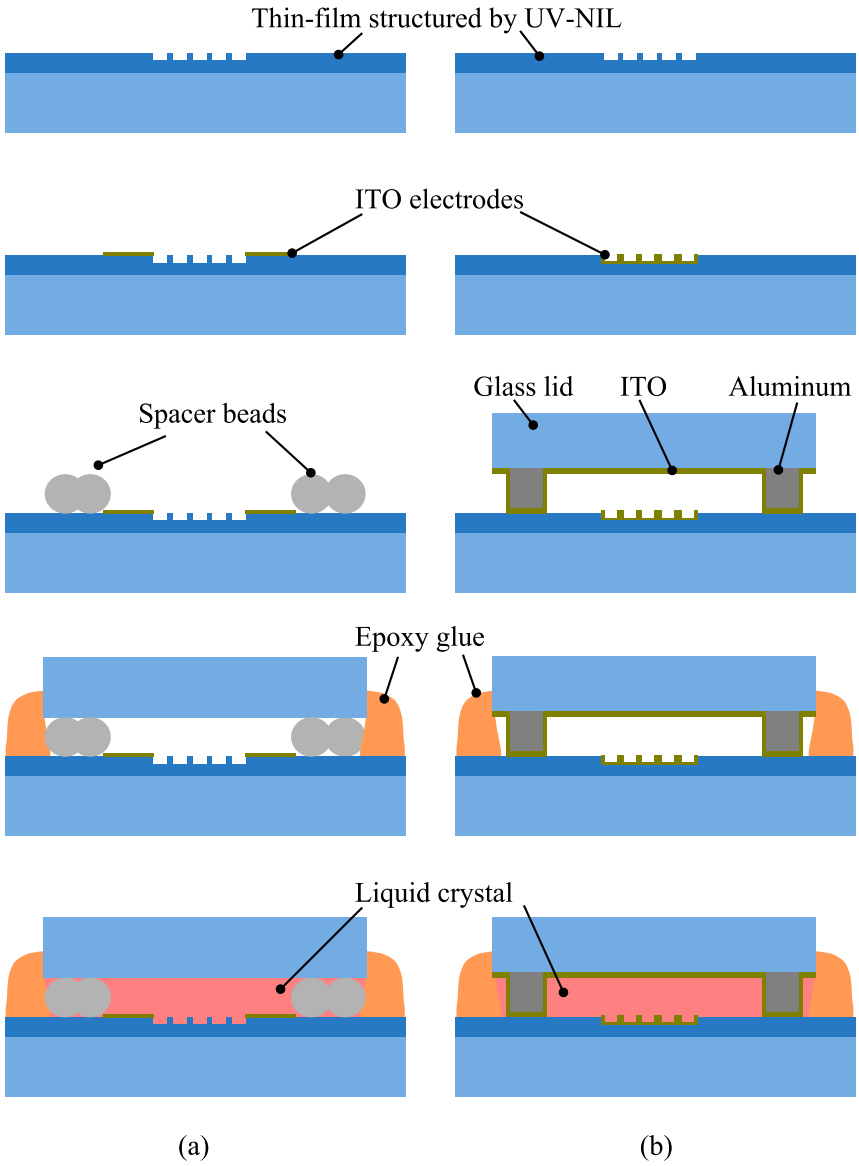

Figure 8.5: Fabrication process for projection display with (a) Planar electrodes. (b) Top/bottom electrodes.

top of the thin-film are defined by photolithography in AZ5214E photoresist. A 45 nm layer of ITO is sputter-deposited onto the resist and a lift-off step in acetone is subsequently performed to remove the resist layer together with the ITO outside the electrode regions.
For the case of the planar electrodes the samples are FDTS coated and 600 nm diameter spacer beads are applied onto the surface. The lid, also FDTS coated, is

pressed onto the bottom glass, separated by the spacer beads, and fixed together with epoxy glue. In the case of top/bottom electrodes, there are no FDTS coatings required, but 600 nm thick aluminum blocks are defined on the lid, followed by a 45 nm ITO coating. The aluminum blocks define the thickness of the LC layer and provide an electrical connection. Again, the lid is pressed onto the bottom part of the sample and fixed with epoxy glue. The epoxy contracts during cross-linking such that the contacts of lid and substrate are pressed together to form an electrical connection to contact the pads on the bottom substrate. In order to fill the cell with LC, the sample is placed on a hot plate at 60 °C while a drop of liquid crystal (5CB) is placed at the edge and fills the cell by capillary forces. When cooling to room temperature, the LC is in nematic phase.

8.3 Experiments

8.3.1 Measurement setup

For the simultaneous measurement of the various physical processes involved, in particular alignment of the LC molecules, redirection of light and their interaction, a setup with the following capabilities is required:

- Observation of white light transmission through the liquid crystal layer between crossed polarizers
- Application of a voltage to individual pixels
- Focusing laser light at the edge of the chip
- Time-resolved measurement of outcoupled light intensity,
- Computer controlled variation of input light polarization and voltage amplitude

In the beginning of the project these properties were measured in separate setups, however it turned out that this is not very efficient since the observations in the two setups could not be related to each other as light redirection and molecular reorientation could not be studied simultaneously. Focusing of light onto the sample edge and observation with a microscope necessitate a complex, yet compact construction which is realized as shown in the drawing in figure 8.6 and in the photograph in figure 8.7. In this setup the orientation of LC molecules can be studied by observation of white light transmission with the sample between crossed polarizers. Simultaneously laser light can be focused onto the chip from the side in order to investigate light guiding and redirection. A voltage can be applied to three pixels and switched on/off for individual pixels. The voltage source is a function generator, set up for a bipolar square wave output which inhibits electrolytic effects. The output of the function generator is limited to 10 V peak-to-peak voltage, therefore a 10x high voltage operational amplifier (based on a Texas Instruments OPA454) is included. Transmitted and redirected light are observed either in the microscope or alternatively the redirected light is observed

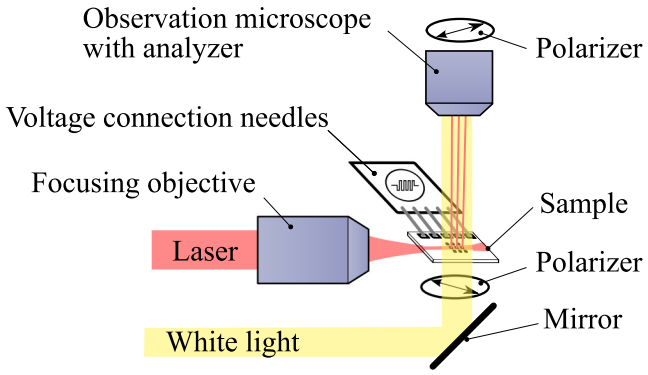

Figure 8.6: Drawing of the measurement setup which allows application of a voltage and simultaneous observation of transmitted white light and redirected laser light.

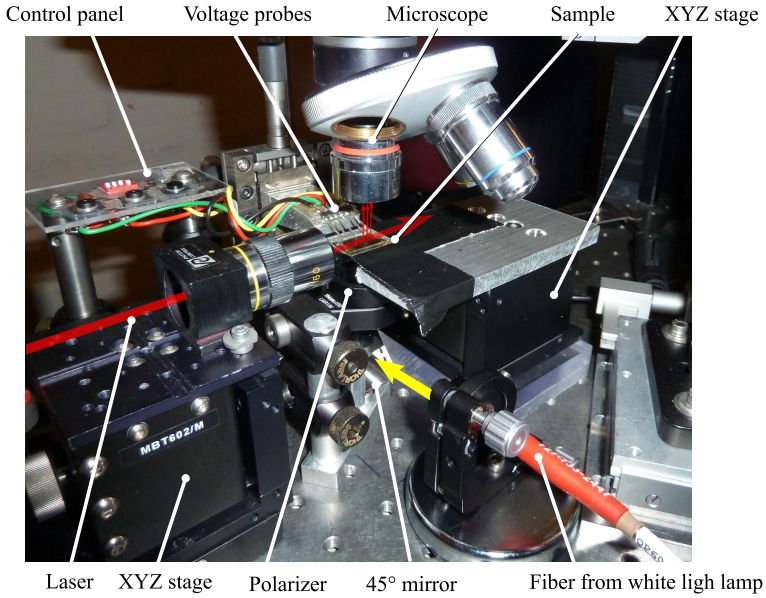

Figure 8.7: Photograph of the setup used for characterization of the displays. White light is supplied by an optical fiber, directed up by a 45° mirror through a polarizer and the sample. A second polarizer (analyzer) is located inside the microscope. Control voltage is supplied by five probes which are actuated by a manual translation stage. In this way the sample is easily exchanged with minimal alignment required. The voltage is switched on/off by buttons on the control panel. Laser light is focused onto the edge of the glass and redirected up. Here it is observed by the microscope or directed onto a screen or photodiode by a mirror (not shown).

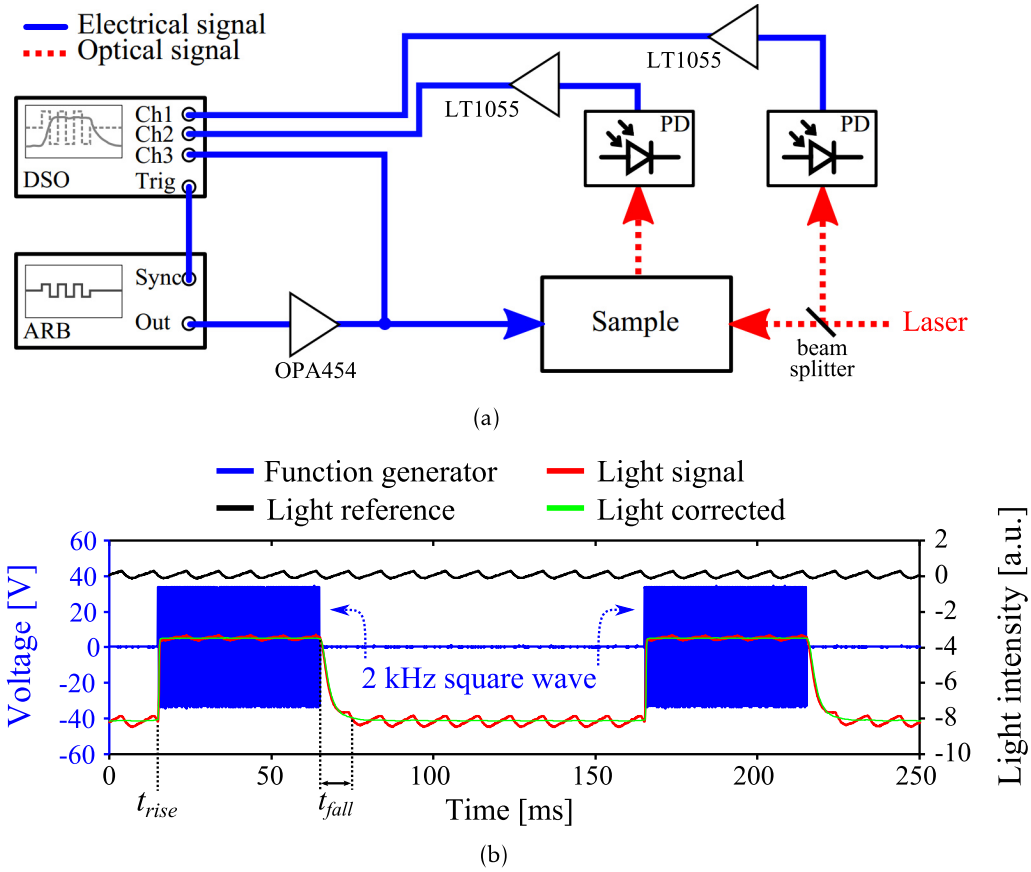

Figure 8.8: Electronics setup for characterization of LC displays. (a) Schematic of the electronics components and connections. DSO: Oscilloscope, ARB: arbitrary waveform generator, PD: photo diode. Amplifiers are depicted by triangles, power supply for amplifiers is not shown. (b) Typical waveforms. The 100 Hz modulation is only seen when a microscope lamp is used for illuminations. The lasers are more stable, such that no reference measurement is required.

directly on a screen, or measured with a CCD camera or a photodiode. The CCD camera allows measurement of the beam profile and divergence, the photodiode is used for characterization of the time response of the liquid crystals, i.e. how fast after switching of a voltage the liquid crystals align and cause an optical effect.
For this time-response measurement the photo diode current is measured by means of a transimpedance amplifier (based on Linear Technology LT1055) and an oscilloscope, while the function generator output is toggled on/off in 50/100 ms intervals. At the switching points the rise- and fall-times of the photo diode signal are measured. When measuring transmitted light from a microscope lamp, an intensity modulation of this light with a frequency of 100 Hz is observed, which originates from the electricity grid. In order to correct this artifact a reference signal is taken from the light incident on the sample and measured with a separate photo diode. A schematic of the electronics setup, consisting of arbitrary function

generator, oscilloscope, photodiodes and amplifiers is outlined in figure 8.8(a). Panel (b) shows typical waveforms measured with this setup.

8.3.2 Non-tunable samples

In a first experiment the projection display is tested without liquid crystal tunability. For demonstration of full-color projection, the sample is constructed by stacking of three glass plates with imprinted gratings of different period, as drawn in figure 8.3(c). A photograph of the sample is shown in figure 8.9(a) and figure 8.9(c) displays the sample in operation with light being focused onto the glass from the right, guided towards the gratings and, at each pixel, a fraction of the light is projected towards the screen. The microscope objective is moved to focus light onto the corresponding plane for each color. The stacked imprinted gratings allow for projection of sharp lines onto the screen and the possibility of projecting light from the lower plates through the upper plates with smaller periods is verified. As demonstrated by the DTU logo in the background, the sample appears highly transparent. Figure 8.9(b) presents a CCD camera image of the projected pixels. The vertical divergence, causing an elongated profile, is a result of focusing by the microscope objective without presence of a light guiding mechanism in the vertical direction. The horizontal divergence is determined by the grating size; here, a 250 µm wide grating results in a line broadening of 740 µm (taken at $1/e^2$), measured at 20 cm distance, corresponding to a beam half-angle divergence of 1.23 mrad.

8.3.3 Planar electrode samples

In this section the tunability of the out-coupling is discussed for the case of samples with planar electrodes and photonic crystals (compare fig. 8.5(a)). Figures 8.10(a)-(c) show optical microscope and SEM images of these samples, fabricated with waveguides across the PhCs with the intention to support light guiding across the PhCs. However, it turns out that it is not possible to couple light into the waveguides for two reasons. First, the thickness of 600 nm of the waveguides is too thin to focus light onto the facet such that the major fraction of the light is guided in the substrate. Second, the waveguide facets are damaged by the dicing process which further reduces the coupling efficiency. Nevertheless, the waveguides may have advantages of increased control and localization of the light instead of illuminating the whole chip, thus reducing scattering. If this is to be exploited it would be necessary to include grating couplers into the waveguides.[99] For now however, it is sufficient to have light guided under shallow angle due to TIR in the substrate, which continuously supplies light for the higher index core waveguide layers. Another problem which is discovered with these samples is that after filling of LC into the cell, an air bobble remains on all photonic crystals, while the cell is otherwise homogeneously filled, as shown in figure 8.11. The dark appearance in the periphery of the gratings indicates homeotropic alignment of the molecules. The area over the photonic crystals also appears dark, but due to absence of liquid crystal. The two are distinguished in the microscope by

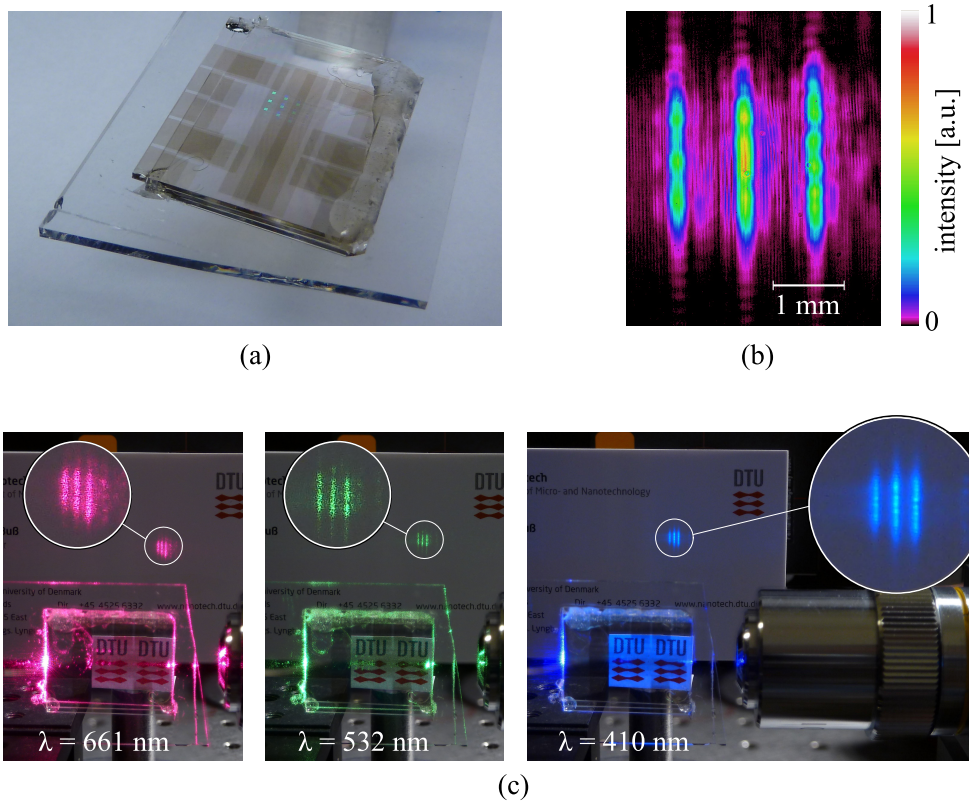

Figure 8.9: (a) Photograph of the sample, consisting of three imprinted glass plates, each plate containing gratings of a different frequency (top to bottom: 274 nm, 355 nm, 441 nm). The sample is glued onto a microscope slide. At the photographed angle the ITO electrodes and diffraction from the gratings are particularly visible. (b) CCD camera image of the projected light (λ = 532 nm). (c) Three-color operation of the transparent projection display, light is focused onto the sample by the microscope objective from the right side and projected onto a screen at 10 cm distance. A logo is placed behind the sample just below the out-coupled beam in order to display the transparency.

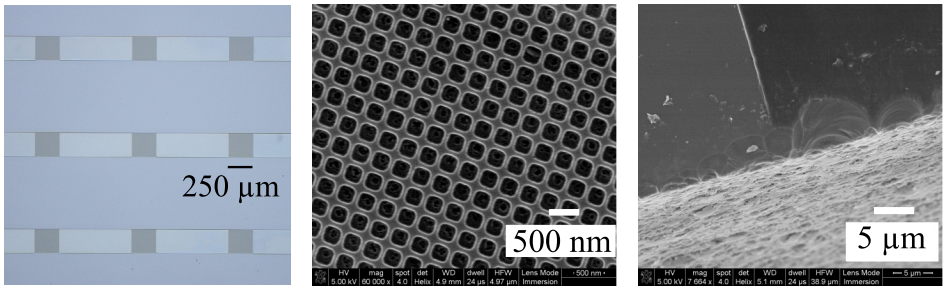

(a) (b) (c)

Figure 8.10: Display samples with waveguides and photonic crystal gratings. (a) Microscope image of gratings and waveguides defined by UV-NIL, prior to definition of electrodes. (b) SEM image of the rectangular lattice photonic crystal. (c) SEM image of the damaged waveguide at the edge of the chip facet after dicing.

observation of fibrillation in the LC filled areas, caused by Brownian motion. A

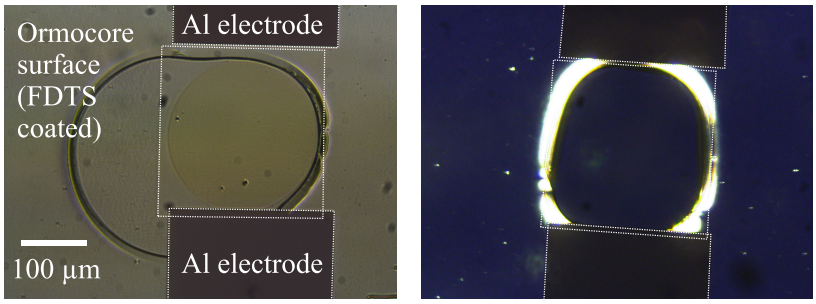

(a) (b)

Figure 8.11: Incomplete infiltration of the cells in the region on top of the imprinted rectangular lattice photonic crystal holes. (a) No polarizers used. (b) A different location on the chip, observed through crossed polarizers.

likely explanation for this effect it that the surface pattern presents an unpreferred energy state to the LC molecules, such that an air bubble is trapped during filling. By manually exerting strong mechanical pressure, it is possible to move the liquid crystal inside the cell and in a few cases it would remain in this state, covering also the photonic crystals. This treatment causes a large amount of disorder and domain boundaries in the cell, such that excessive scattering results and it is hardly possible to guide light and observe a clear spot of the redirected light. For a test of the basic principle however, light is directed onto the grating from free-space through the lid under an angle of approximately 20°. The reflected diffraction order is observed in a CCD camera and by application of a voltage it is observed that the spot is extinguished, see figure 8.12. However, it is not clear whether this effect is based on reduced diffraction efficiency due to phase matching of the liquid crystal with the grating, or simple scatting. The reorientation process of the molecules is studied more detailed in a test sample, where no photonic crystal is present. In figure 8.13

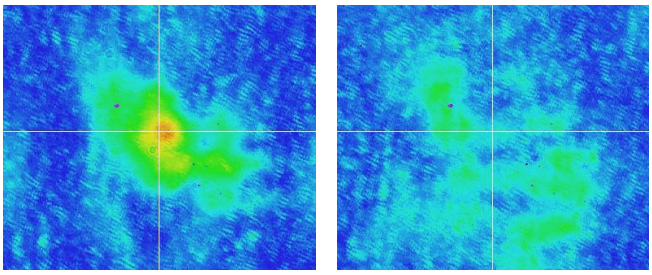

(a) (b)

Figure 8.12: Tuning of a free-space diffraction order, reflected off a liquid crystal tuned grating. Applied voltage of (a) 0 V. (b) 60 V.

the sample is observed in white light transmission between crossed polarizers. For this test the electrodes are made from aluminum and therefore opaque. In the case of zero applied voltage the liquid crystal, surrounding and covering the electrodes also appears black since the LC molecules are aligned homeotropically and light is fully blocked by the crossed polarizers. If the voltage is increased the molecules align with the electric field lines, but the strong anchoring at the surfaces where the molecules pertain their alignment leads to an overall inhomogeneous alignment. This disorder causes re-polarization of the light that has passed the polarizer and therefore transmission of light through the analyzer. With higher voltage applied, the region of reoriented molecules proceeds further and bridges the gap between the electrodes. Since the approach of electrodes on top and bottom sample appears more viable, no further investigations are made on the planar electrode geometry.

8.3.4 Top/bottom electrode samples

In this section the operation of the display samples with electrodes on the bottom substrate directly covering the gratings and the lid are presented. The sample consists of a single glass plate with imprinted gratings, electrodes, LC filling and a lid (compare fig. 8.5(b)). A photograph of the LC filled sample is shown in figure 8.14(a), along with an SEM image of the ITO covered grating in fig. 8.14(b). The sample The operation of the samples is investigated in two ways. In the first experiment, the sample is observed in an optical microscope using a white light transmission mode in order to study the physical processes (i.e. not how the display device is intended to operate). The sample is placed between crossed polarizers, serving as polarizer and analyzer, as shown in figure 8.15(a). Outside the grating area the molecules are ordered over short ranges only and disclinations in the orientational order are seen as bright lines. The regions with gratings show only minor disclinations and the area in general appears darker, indicating that the grating dictates parallel alignment of the molecules. However, the effect may decrease further away from the grating (close to the lid) such that crystal defects occur and can be observed as lines in the lower left and right corners of the grating area. Under an applied voltage between grating and lid, above the threshold for the Frederiks transition,[100] the liquid crystals re-orient towards homeotropic

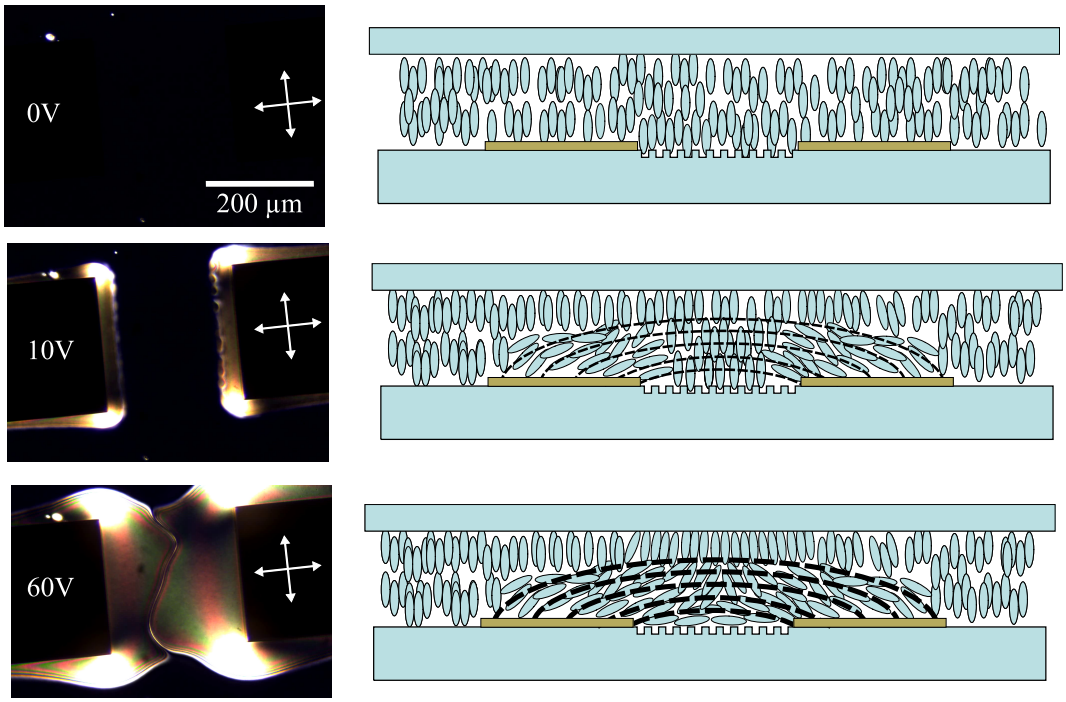

Figure 8.13: LC molecule reorientation for planar electrode samples.

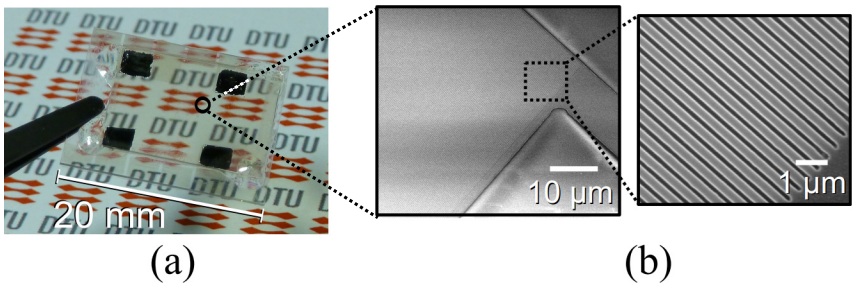

Figure 8.14: (a) Photograph of an assembled device, filled with liquid crystals. The device is essentially transparent, except for the aluminum spacers, which provide electrical connection between lid and substrate. (b) Scanning electron microscope (SEM) image of the imprinted gratings covered with an ITO electrode.

alignment (perpendicular to the surface). With a voltage of 36 V applied, as shown in the upper right image of figure 8.15(a), the molecules align parallel to the electric field such that the light path is along the optic axis and no birefringence is present. The polarization of transmitted light remains unaltered during passage through the cell and light is absorbed by the analyzer, causing a completely black appearance of the grating.

In the second experiment, shown in figure 8.15(b), the samples are characterized

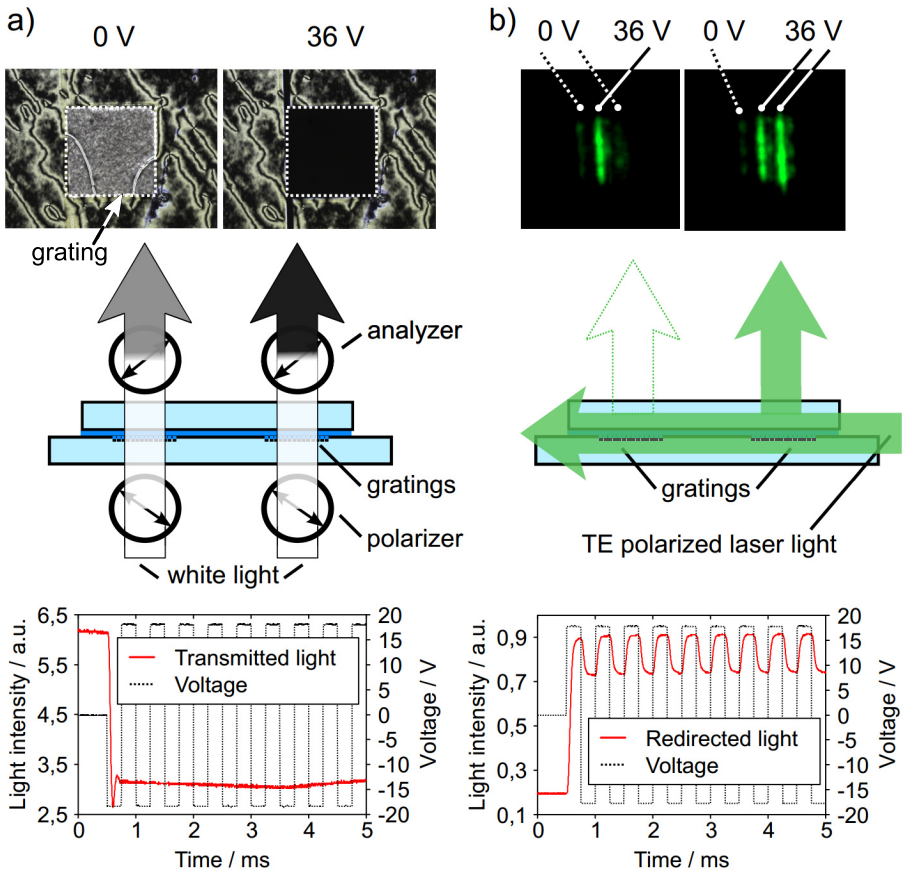

Figure 8.15: (a) Characterization of the sample in a transmission optical microscope with crossed polarizers. For the case of zero applied voltage, the grating appears darker than the surrounding but not completely opaque due to topographical LC orientation with the grating. With an applied voltage, the LC molecules align parallel to the E-field throughout the cell such that the crossed polarizers block all of the light and the grating area appears completely black. (b) Measurement of the redirected light. The right-most pixel of three is switched between the off-state (left) and the on-state (right) when the applied voltage induces a change in the refractive index of the LC, covering the grating.

in a configuration as a projection display, with light being coupled in from the side and a fraction of the light is out-coupled. When the voltage is applied, the

reorientation of the anisotropic LC molecules results in a change in the refractive index perceived by the light, and thereby modifies the diffraction efficiency of the grating. In order to suppress electrolytic effects, the electrical signal is a bipolar square waveform at 2 kHz, as shown in the lower part of fig. 8.15, together with the response of the transmitted and redirected light.
A notable difference between the two configurations is observed in the temporal response. The transmitted light intensity is constant after the voltage is switched on, but the redirected light intensity has response times fast enough to partly follow the switchover of the driving voltage with rise and fall times in the microsecond range. This discrepancy is explained by the different physical processes: during the on-switch state the LC molecule orientation is induced by the electric field, while for the off-switch state the reorientation is due to relaxation caused by the anchoring force at the grating. This restoring force is larger close to the grating surface and the process occurs on quicker timescales than further away from the surfaces.[101] In transmission mode the light intensity is affected by the alignment of LC molecules throughout the entire cell from grating to lid. For the redirection scheme instead, only the molecules in close proximity to the grating have an influence on the diffraction efficiency; hence fast reorientation into the unperturbed state after switching-off the voltage is possible in this case.
In figure 8.16 the optical behavior is analyzed in more detail at a number of

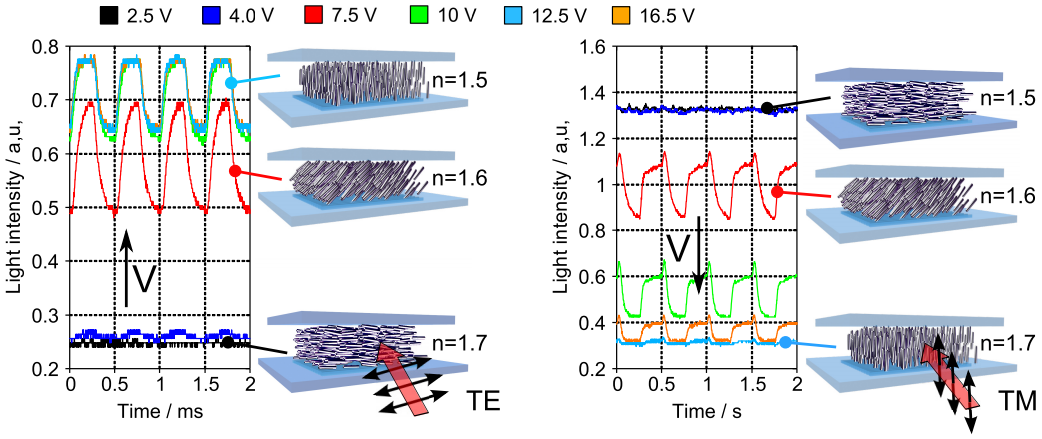

Figure 8.16: Time-resolved measurement of out-coupled light intensity for TE and TM polarized light. With increasing voltage, the molecules tilt from parallel to perpendicular alignment and depending on the polarization, different refractive indices are perceived by the light. This results in the opposite voltage-intensity relation for TE/TM polarization.

applied voltages and for incident light using both TE and TM polarization. In the case of TE polarization, zero applied voltage corresponds to the minimum of out-coupled light. The molecules are aligned parallel to the grating and as the light wave oscillates along the long (slow) axis of the LC molecules, the perceived refractive index in the LC is 1.7. When the voltage is increased and the molecules tilt towards homeotropic orientation, the perceived refractive index is

decreased, reaching 1.5 in the final state. This decrease in perceived LC refractive index corresponds to an increase in refractive index contrast between the LC and the grating (refractive index of ITO, 2.3), causing an increase in the diffraction efficiency, i.e. increase of the diffracted light intensity. The opposite case is seen when TM polarization is used: at zero applied voltage the light polarization is perpendicular to the long axis of the LCs, sensing a low refractive index, i.e. a large index contrast to the grating and high intensity of the out-coupled light. Increasing of the voltage consequently reduces the out-coupled light intensity.
These measurements verify that the intensity of redirected light is indeed controlled by adjustments of the refractive index which the light perceives when impinging on the grating. Ideally it should be possible to completely suppress the out-coupled light (apart from scattering) when the refractive index of the grating and the liquid crystal are exactly matched. This could not be achieved with the devices presented here due to the high refractive index ITO layer which is deposited on top of the grating. Since higher refractive index liquid crystal materials are not commonly available, an alternative may be to bury the ITO electrodes below the polymer grating.
Considering the contrast of the projection display, i.e. the difference between the light intensity in the on- and off-state, it is noted that TM polarized light is more suitable. This effect is assumed to originate from the complex interplay between the optical mode profile in the waveguide layers and the grating efficiency, both as function of LC orientation and light polarization. Complex numerical simulations, involving alignment of the LC, confinement and guiding of optical modes in the LC with anisotropic refractive and reorientation of LC under an applied electric field would be required for further investigation.
The response times are measured with rise-times well below 1 ms and fall-times of 4.5 ms, as shown in figure 8.17(a). Switching times are measured between 5% and 95% light intensity upon switching the 2 kHz signal on/off. An investigation of the threshold voltage is presented in figure 8.17(b) and the value is measured to be approximately 6 V for both TE and TM polarization.

8.4 Discussion

The time-resolved intensity measurements have demonstrated that switching times in the sub 100 microsecond regions are feasible with standard LC material in the presented device geometry. In particular, this is observed not only for switching-on, but also for switching-off, which is usually the limiting factor in LC devices. This is possible because the strong surface anchoring with fast relaxation is exploited by using an optical effect which is localized very close to the surface, in this case inside the 120 nm thin grating lines. Additional experiments, especially with different LC layer thicknesses, shall reveal whether this fast µs-scale modulation may be used practically. Already now, the switching speed of less than 5 ms is comparable to existing display devices.
Due to the strong anchoring on the surface, the threshold voltage of 6 V is somewhat larger than typical LC displays which have a threshold around 2.5 V,[102]

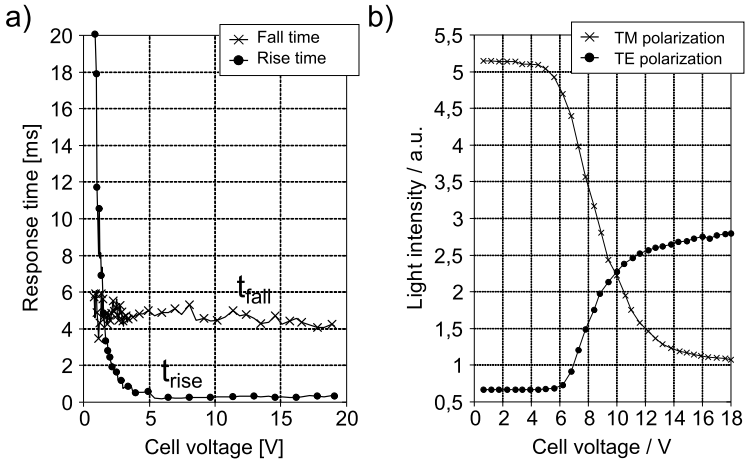

Figure 8.17: (a) Measurement of the response times for TM polarized light as a function of the applied voltage. (b) Measurement of the voltage threshold for TE and TM polarization.

but still accessible to voltages used in consumer electronics and significantly below the high voltages reported in some other LC-actuated optical devices.[37,103–105] It should also be noted that the threshold is rather "soft", with linear tuning of the light intensity via voltage switching possible from 6 V to 10 V.
For integration of high resolution displays into small devices, the grating size may need to be reduced below the dimensions presented in this work. However, this will correspondingly increase the divergence and limit the maximum projection distance, pointing to a design compromise between resolution and depth of focus to be made. Additional optical elements such as microlenses could be applied to the outside of the device to enhance the projection distance, although this will come at the cost of distorting the image viewed through the otherwise planar transparent materials.

8.5 Outlook

The investigations in this chapter have shown very rich physics of the device with many different and interacting effects. For a better understanding, a complex multiphysics simulation should be carried out in a software like e.g. COMSOL. Currently the projected image quality is limited by a low contrast. This is caused by residual light redirection in the off-state because accurate index matching between the liquid crystal layer and the grating material is not achieved when the grating is covered with ITO. This can be circumvented if the electrode is buried below the gratings, which is however more complicated in terms of fabrication. Furthermore, the variation of the LC layer thickness should yield interesting insight into the behavior of the molecular alignment in even more confined cells and the influence on response time. Another issue which needs to be solved is the vertical divergence

of pixels into lines when a microscope objective is used for focusing. Instead a cylindrical lens could be used which only focuses the light to the thickness of the glass, but not in the vertical direction where no focusing is required. Initial promising experiments with a cylindrical lens are shown in figure 8.18.

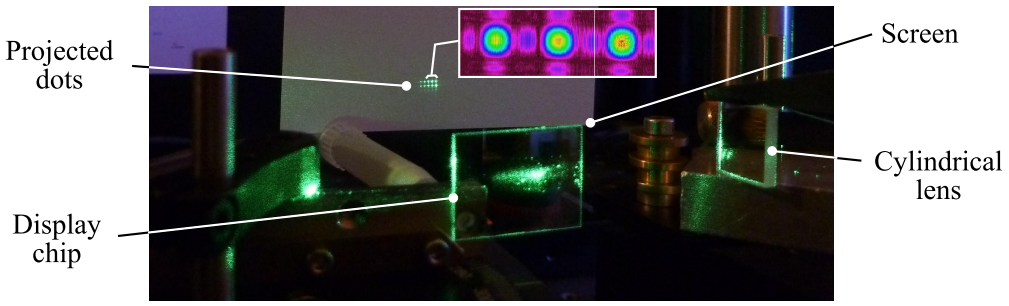

Figure 8.18: Operation of the display device with a cylindrical lens instead of focusing with a microscope objective. The square pixels do not divergence to a line shape in this case. The inset shows a CCD camera image of the projected spots, at 13.5 cm distance from the sample. The sample has no LC or lid attached.

8.6 Conclusion

To conclude, a transparent and fully integrated electronically modulated color projector display is demonstrated, based on optical gratings with a thin liquid crystal layer. The device operates at 10 V with a fall-off response time of less than 5 ms. The underlying physics of the liquid crystal director reorientation with respect to the grating enables 90 µs response times due to the localization of the optical effect in the proximity of the grating surface. The results denote a key step towards a new generation of compact and transparent projection display technology, with possible applications in head-up displays or other technologies where controlled redirection of guided light is required at specific locations from a transparent substrate.

9 Discussion and outlook

In the preceding chapters various applications of transparent photonic systems in both static and tunable schemes are investigated. In particular, these investigations are based on a combination of waveguiding and conversion between free-space and guided modes via grating couplers. Even though the design freedom is limited under the constraint of using transparent materials and two-dimensional surface indentations, convincing results are demonstrated in the context of solar harvesting, daylighting through windows, photonic crystal dye lasers and projection displays. One-dimensional photonic crystals, i.e. gratings are used for solar harvesting in transparent surfaces. The diffraction efficiency of free-space light into guided modes is less than 10%, such that only a small fraction of the incident light is used for electricity generation while maintaining the requirement for transparency. Despite the low efficiency, the technology is identified to be useful in two cases. The first case is found when excessive unused areas are available which make up for the low efficiency. Due to the simplicity of the method and the reduced demand on costly high-efficiency solar cells by locating them only at the sides, the gratings are shown to be a viable method for electricity generation from large windowpanes. The other application is found at much smaller dimensions in hand-held electronic devices, such as watches, mobile phones and cameras. For the case of mobile phones and cameras, the amount of generated electricity will most likely not be enough to sustain operation, but could be used for recharging of the battery over longer periods. Electronic devices often have strict requirements for a distinct design, which must not be obstructed by the presence of solar cells. This can be avoided by integrating the solar harvesting into the display glass, which often covers a significant fraction of the device surface area. Of course, vision quality onto the display must not be compromised by the presence of solar harvesting gratings. One possible compromise scenario could be achieved by the integration of bi-stable liquid crystals[106] that switch the display between solar-harvesting mode and display mode, where energy is only consumed for the LC during the instant of switching. However, degradation of the LC during prolonged exposure to sunlight may be a critical issue even though standard glass absorbs a significant amount of UV light. A solution could be to apply a UV light filter as a first layer onto the glass, which may be feasible by low cost nanoimprinted PhC with band-gaps in the UV light region. Aside from LCs also other, inorganic, materials are available for tunability, as presented in ref.[107]
Another alternative to reduce energy consumption is demonstrated in the studies of improved daylighting via disordered gratings. A clear improvement of the daylighting effect is achieved by optimization of the degree of disorder and, despite

the use of diffractive gratings, the rainbow effect is efficiently suppressed. Other reported daylighting systems, such as prisms of micron to millimeter scale or large reflective blinds achieve similar or even better daylighting performance, however, these systems have the disadvantage that they affect the façade architecture and inhibit vision through the window. Therefore the diffractive disordered daylighting windows present a favorable compromise between efficiency and transparency. In addition to the optical design, there are further considerations which affect the fabrication process. The fabrication scheme must not only be capable of producing the required high aspect ratio gratings, but also it must be able to do so by a replication-based process to enable high volume production. Moreover, since there must not be any degradation over many years, a material that provides high mechanical and optical stability is required. The SSGNIL process delivers on both accounts, although mechanical stability may still be an issue and the nanostructures must e.g. sustain cleaning of the window. On the other hand, nanostructures may also be used for the creation of self-cleaning surfaces and it may be interesting to investigate whether the effect of self-cleaning can be combined with optical daylighting. Windows also present the possibility to embed the optically functional layer on the inside of a double-glazing to mitigate the likelihood of mechanical damage.

Furthermore, lasers based on tunable photonic crystal resonators are discussed, with potential applications in lab-on-a-chip systems. Tunable lasers enhance the capabilities of such systems by enabling probing of the analytes at different wavelengths in optical detection methods. However, a trade-off has to be made between tuning range and response time. While existing technologies for tunable microchip dye lasers, based on mechanical stretching of the laser resonator or mixing of different dyes, offer tunability over 70 nm,[36] the response times of these systems are very slow. In contrast, the response time of the liquid crystal effect is at least an order of magnitude faster, with the downside of the tuning range being limited to less than 18 nm. Another limitation of mechanical resonator stretching is that this is only practical for application to single lasers, but not for more complex devices that comprise several lasers. Furthermore mixing of different dyes requires complex support systems such as pumps and mixing meanders; Here, the PhC-LC laser has a clear advantage since the direct electrically controlled tuning is much easier to use and integrate with existing systems. The footprint of the laser is not increased by the addition of tunability because electrodes are only required above and below the resonator. However, electrode connections on substrate and lid are required which do increase the system complexity in relation to non-tunable lasers. In this respect it has to be considered whether or not, depending on the application, it may be preferable to fabricate an array of fixed-period lasers with slightly different wavelengths. Since the wavelength of a non-tunable laser is simply controlled by the PhC lattice constant, several lasers of different emission wavelength can easily be fabricated in parallel without additional cost, except for the required wafer area. Nevertheless, if minimal footprint and continuous tunability over a limited range are required, the LC-PhC laser represents a beneficial solution compared to other techniques. Even though continuous electrically controlled tuning is not demonstrated, the results from

temperature tuning and results from the related experiments with projection displays strongly support the point that this is feasible.
A transparent projection display consisting of a complex electro-optic system is presented, combining waveguiding, light redirection and liquid crystal tunability in a transparent chip. The system demonstrates that the performance of typical LC displays such as those used in screens or traditional projectors can be transferred into transparent unobtrusive device. In particular, three-color projection, low voltage and fast response times are shown here. An aspect that needs additional investigation is the image resolution and quality. This might be limited by the achievable homogeneity of the light distribution across large areas of gratings. At the moment the relationship between the grating size and the beam divergence is not fully investigated but it is expected that the outcoupled light diverges as a Gaussian beam, with the waist located at the grating. This means that a reduction of the grating size increases the divergence and if the beams of neighboring pixels overlap, the image becomes blurred. This imposes a trade-off between the size of the projection aperture on the device in relation to the illuminated area. A few other transparent projection displays are reported in the literature, where these systems generate an image is generated by an external display. The display image is focused with a lens onto a grating that couples the light into the glass where it is guided and then outcoupled at another position. Such an approach is clearly less compact and the source display obstructs part of the surface. Another advantage of the system presented here is that it operates with coherent laser light, facilitating projection without focusing onto curved surfaces such as a car windscreen. For simple applications it is also possible to limit the display to the projection of a number of fixed symbols, for example in automotive driver assistance systems. These can be simply defined by changing the shape of the gratings from rectangular to any other desired contour.
It is noted that one limitation of the present device is the fact that the complete chip is illuminated with light. Therefore any scattering source, such as particles on the surface, unordered domains of LC molecules or roughness at the diced edges reduces the signal to noise ratio on the screen. This may be improved by using waveguides to guide the light across the pixels only. Scattering in the LC layer could be reduced by achieving homogeneous LC alignment not only in the grating regions, but throughout the chip. This can be done in two ways. Either very low amplitude directional surface roughness can be generated by oblique angle ion beam sputter deposition of SiO_2[108] on the substrate and the lid. If the amplitude of the roughness is small enough there is a negligible optical effect while still alignment of the LC molecules still occurs. Another alternative is the use of an FDTS coating such as the one applied on the planar electrode samples. The homeotropic alignment is essentially defect free, but prevents the use of gratings, since these counteract the homeotropic alignment due to the topography. Instead, patterns with less pronounced directionality are required, such as 2D photonic crystals. Such patterns have been reported to support homeotropic alignment[109] and furthermore photonic crystals could also allow using more advanced PhC structures with beam shaping capability[110] for light redirection. Further work is required on incoupling optics to reduce the divergence of light in the vertical

direction, and first experiments with a cylindrical lens show promising results. With the progress of research on direct green laser diodes it may even be possible to assemble three red, green and blue laser diodes directly onto the chip and butt-couple the laser diode facets to waveguides which distribute the light across the chip, thus significantly reducing the total size of the system. A remaining challenge is the fabrication of a three-layer LC stack with electrical connections to each layer for full color projection, but this is more a technical, rather than a scientific, problem.

In general, the technology of photonic crystal-adaptive light guiding and redirection could also be applied to a number of other fields than those presented already. The electronics industry is managing well to keep up with Moore?s law and electronic processors double their speed every 18 months. In order to use this potential, also the exchange of data at the same speed is desired, e.g. between the CPU, graphics unit, memory, etc.[111] Optical communication links can provide these high data rates but are expensive. LC covered gratings, as presented in the context of projection displays, even with the fast µs switching times observed, are by far too slow to modulate signals directly for optical communication purposes. Yet, this technology may be used as a reconfigurable coupler, receiving data from one source, and distributing it to one or several other selected recipients, such that the total required number of optical links is reduced. Also in the rapidly advancing field of multilayer photonic circuits[112] it may be desirable to selectively redirect optical signals from one device layer into another. IN addition, transparent lab-on-a-chip (LOC) systems could benefit not only from tunable lasers, but also from reconfigurable couplers, which allow light direction to specific locations on the chip. In this way reconfigurable light patterns for optical sensing or cell manipulation can be generated directly inside a chip for precise control of localized spectroscopy[113] or optical forces[114,115] at multiple points. However, despite all the enthusiasm for the successful integration of adaptive photonic crystal devices in transparent substrates, it should be noted that there will always be a compromise between device performance and visibility. The human eye is an incredible optical detector with the ability to see individual photons and an outstanding dynamic range, meaning that minute diffraction and scattering effects by optically functional nanostructures will always be visible, at least under certain angles of incidence.

10 Conclusion

In this thesis it is shown that the functionality of transparent devices can be enhanced by the application of optically functional nanostructures, combined with electrical tunability. This is demonstrated in four example systems, where each of the systems has a specific focus.
Solar harvesting gratings demonstrate incoupling and guiding of light over a wide range of wavelengths (410 nm, 532 nm and 661 nm), and incidence angles from ?60° to +60°. Furthermore it is demonstrated that transparency is well maintained for gratings with 355 nm period.
Disordered gratings are used to demonstrate the engineering of diffraction patterns from highly peaked ordering into much broader distributions, covering 95° of angular range. Optimum parameters for the disorder of 50% and 400 nm period are determined for daylighting applications, verified quantitatively by measurements of 410, 532 and 661 nm diffracted light and qualitatively by observation of transmitted white light where a homogeneous light distribution with strongly reduced rainbow-like coloration is observed.
Tunable photonic crystal effects are demonstrated for dye-doped liquid crystal lasers. In these lasers multiple functionalities are integrated in a single photonic crystal. The 360 x 200 nm rectangular lattice PhC determines lasing wavelength, while simultaneously pump light redirection reduces the laser threshold. The tunability is achieved by means of liquid crystals, and if required, the system can be fabricated in transparent materials. Lasing is demonstrated in a 300 nm thin layer of 5CB, doped with 1wt% of Pyrromethene 597 and it is shown that an applied voltage of 16 V is able to reorient the LC molecules to reconfigure the lasing properties. Experiments with temperature variation have shown a potential for a tuning range of 18 nm.
Finally the tunability of gratings for light redirection is investigated in a transparent projection display configuration that operates without polarizers. It is shown that device transparency is maintained for the complex integrated opto-electronic system, with imprinted human-invisible, still optically functional, sub-wavelength gratings, transparent electrodes and liquid crystal layers. Due to the localization of the optical effect close to the grating surface low switch-off response times of 4.5 ms are achieved, with a potential for operation in the sub-100 µs regime. A low threshold voltage of 6 V is observed.
These examples demonstrate that photonic systems, based on light guiding, redirection and tunable in- and outcoupling are feasible in transparent devices. This offers possibilities to enhance the functionality of many transparent every-day objects. Together with advancements in other fields such as transparent batteries

and solar cells, it can be expected that future research will result in the creation of a large variety of transparent integrated electro-optic systems related to window-pane integrated energy-saving solutions, projection displays, heads-up displays, photonic integrated circuits and optical manipulation and sensing platforms.

Bibliography

[1] U.S. Energy Information Administration, "Annual electricity generation," http://www.eia.gov/countries/data.cfm. Accessed October 29th, 2012. 10

[2] A. V. Shah, H. Schade, M. Vanecek, J. Meier, E. Vallat-Sauvain, N. Wyrsch, U. Kroll, C. Droz, and J. Bailat, "Thin-film silicon solar cell technology," Progress in Photovoltaics **12**, 113–142 (2004). 11

[3] S. Guenes, H. Neugebauer, and N. S. Sariciftci, "Conjugated polymer-based organic solar cells," Chemical Reviews **107**, 1324–1338 (2007). 11, 12

[4] V. D. Rumyantsev, "Solar concentrator modules with silicone-on-glass Fresnel lens panels and multijunction cells," Opt. Express **18**, A17—-A24 (2010). 11, 58

[5] Senatsverwaltung für Stadtentwicklung und Umwelt, "Daten zum Berliner Hauptbahnhof," http://www.stadtentwicklung.berlin.de/umwelt/klimaschutz/aktiv/solarenergie/projekte/de/hauptbahnhof.shtml. Accessed October 1st, 2012. 12

[6] Solar Century, London, UK, "Case study CIS 'Solar Tower'," http://web.archive.org/web/20070905124144/http://www.solarcentury.com/projects/commercial/cis_solar_tower. Accessed August 4th, 2011. 12

[7] U. Polysolar, Cambridge, "Commercial transluscent solar cells." http://www.polysolar.co.uk/. Accessed October 24rd, 2012. 12

[8] BSW-Solar/Sharp, "Photograph of CIS Tower," http://www.cleanthinking.de/wp-content/uploads/BSW-Solar-Bundesverband-Solarwirtschaft.htm. Accessed October 20th, 2012. 12

[9] Pythagoras Solar, Petach Tikva, Israel, "Commercial window integrated solar cells by Pythagoras Solar." http://www.solarchoice.net.au/blog/solar-pv-windows-bipv-building-integrated-photovoltaics -technology -by- pythagoras-solar. Accessed October 24rd, 2012. 13

[10] J. Wiegman and E. van der Kolk, "Building integrated thin film luminescent solar concentrators: Detailed efficiency characterization and light transport modelling," Solar Energy Materials and Solar Cells **103**, 41–47 (2012). 13

[11] M. G. Debije, "Solar Energy Collectors with Tunable Transmission," Advanced Functional Materials **20**, 1498–1502 (2010). 13

[12] M. G. Debije and P. P. C. Verbunt, "Thirty Years of Luminescent Solar Concentrator Research: Solar Energy for the Built Environment," Advanced Energy Materials **2**, 12–35 (2012). 13

[13] C.-c. Chen, L. Dou, R. Zhu, C.-h. Chung, T.-b. Song, Y. B. Zheng, S. Hawks, G. Li, P. S. Weiss, and Y. Yang, "Visibly Transparent Polymer Solar Cells Produced by Solution Processing," Nano letters **6**, 7185–7190 (2012). 13

[14] Uhrenfabrik Junghans GmbH & Co. KG, "Wrist watch with solar cells integrated into the dial," http://www.junghans.de/tl_files/04-product_image/Image_big/018-1120-44-big.jpg. Accessed October 21st, 2012. 14

[15] LG, "Mobile phone with solar cell battery cover," http://www.lg.com/uk/mobile-phone-accessories/lg-PCB-100. Accessed October 21st, 2012. 14

[16] Samsung, "Notebook computer with solar cell on the backside of the cover," http://www.samsung.com/us/business/laptops/NP-NC215-A01US. Accessed October 21st, 2012. 14

[17] digitalreview.ca, "Digital camera without solar cells." http://www.digitalreview.ca/pics/Panasonic_2010/Panasonic_ZS7_TZ10_top_slant.jpg. Accessed October 21st, 2012. 14

[18] T. M. de Jong, D. K. G. de Boer, and C. W. M. Bastiaansen, "Surface-relief and polarization gratings for solar concentrators," Optics Express **19**, 15127–15142 (2011). 14, 15

[19] M. Frondel and S. Lohmann, "The European Commission's light bulb decree: Another costly regulation?" Energy Policy **39**, 3177–3181 (2011). 15

[20] Wikipedia, "Phase-out of incandescent light bulbs." http://en.wikipedia.org/wiki/Phase-out_of_incandescent_light_bulbs. Accessed October 23rd, 2012. 15

[21] B. F. Mills and J. Schleich, "Why donâ€™t households see the light? Explaining the diffusion of compact fluorescent lamps," Resource and Energy Economics **32**, 363–378 (2010). 15

[22] B. Bläsi, A. Gombert, and M. Niggemann, "Microstructured Polymer Surfaces with Complex Optical Functions for Solar Applications," in "Polymers - Opportunities and Risks II SE - 14," , vol. 12 of *The Handbook of Environmental Chemistry*, P. Eyerer, M. Weller, and C. Hübner, eds. (Springer Berlin Heidelberg, 2009), pp. 263–279. 15

[23] N. Wang and M. Boubekri, "Investigation of declared seating preference and measured cognitive performance in a sunlit room," Journal of Environmental Psychology **30**, 226–238 (2010). 15, 17

[24] S. W. Lockley, G. C. Brainard, and C. A. Czeisler, "High Sensitivity of the Human Circadian Melatonin Rhythm to Resetting by Short Wavelength Light," J. Clin. Endocr. Metab. **88**, 4502 (2003). 15

[25] J. T. Kim, "Prediction of Discomfort Glares from Windows: Influence of the Subjective Evaluation of Window Views," Indoor Built Environ **21**, 92–97 (2012). 16

[26] M. Kischkoweit-Lopin, "An overview of daylighting systems," Solar Energy **73**, 77–82 (2002). 16, 17

[27] K. Papamichael, C. Ehrlich, and G. Ward, "Design and evaluation of daylighting applications of holographic glazings," Final Report prepared for Physical Optics Corporation under Contract Agreement Number BG-95037 (1996). 16

[28] S. Klammt, A. Neyer, and H. F. O. Müller, "Microoptics for efficient redirection of sunlight," Appl. Opt. **51**, 2051–2056 (2012). 17

[29] J. Ludman, J. Riccobono, G. Savant, J. Jannson, G. Campbell, and R. Hall, "Holographic daylighting," in "Proc. SPIE 2532, Application and Theory of Periodic Structures," , vol. 2532, T. Jannson, ed. (1995), vol. 2532, pp. 436–446. 17

[30] H. J. Gerritsen, "Diffractive daylighting: ways to obtain wide-angular-range, large-efficiency, near-achromatic operation," in "Optical Materials Technology for Energy Efficiency and Solar Energy Conversion XII," , vol. 2017, C. M. Lampert, ed. (SPIE, 1993), vol. 2017, pp. 377–388. 17

[31] D. Janasek, J. Franzke, and A. Manz, "Scaling and the design of miniaturized chemical-analysis systems." Nature **442**, 374–80 (2006). 17

[32] X. Wei and S. M. Weiss, "Guided mode biosensor based on grating coupled porous silicon waveguide." Optics Express **19**, 11330–9 (2011). 17

[33] B. Helbo, A. Kristensen, and A. Menon, "A micro-cavity fluidic dye laser," J. Micromech. Microeng. **13**, 307–311 (2003). 18

[34] C. Monat, P. Domachuk, and B. J. Eggleton, "Integrated optofluidics: A new river of light," Nat Photon **1**, 106–114 (2007). 18

[35] B. Bilenberg, T. Rasmussen, S. Balslev, and A. Kristensen, "Real-time tunability of chip-based light source enabled by microfluidic mixing," Journal of Applied Physics **99**, 23102 (2005). 18

[36] Z. Li, S. Member, D. Psaltis, I. Paper, and A. L. C. Design, "Optofluidic Distributed Feedback Dye Lasers," IEEE Journal of Selected Topics in Quantum Electronics **13**, 185–193 (2007). 18, 110

[37] T.-H. Chao, T. T. Lu, S. R. Davis, S. D. Rommel, G. Farca, B. Luey, A. Martin, and M. H. Anderson, "Compact liquid crystal waveguide based Fourier transform spectrometer for in-situ and remote gas and chemical sensing," Proc. SPIE **6977**, 69770P–69770P–11 (2008). 18, 107

[38] T. Matsui, O. Masanori, and Y. Katsumi, "Tunable laser action in a dye-doped nematic liquid-crystal waveguide under holographic excitation based on electric-field-induced TM guided-mode modulation," J. Opt. Soc. Am. B **21**, 1651–1658 (2004). 18, 19

[39] R. Ozaki, T. Shinpo, K. Yoshino, M. Ozaki, and H. Moritake, "Tunable Liquid Crystal Laser Using Distributed Feedback Cavity Fabricated by Nanoimprint Lithography," Applied Physics Express **1**, 12003 (2008). 18, 19, 83, 88

[40] J. D. Joannopoulos, R. D. Meade, and J. N. Winn, *PhotonicCrystals: Molding the Flow of Light* (Princeton University Press, 1995). 18, 24

[41] M. B. k. Christiansen, A. Kristensen, S. Xiao, Mortensen, and N. Asger, "Photonic integration in k-space: Enhancing the performance of photonic crystal dye lasers," Applied Physics Letters **93**, 1101–1103 (2008). 19, 83

[42] K. Gupta, D.-H. Kim, D. Ellison, C. Smith, and A. Levchenko, "Using Lab-on-a-Chip Technologies for Stem Cell Biology," in "Stem Cells & Regenerative Medicine," , K. Appasani, R. K. Appasani, and K. Turksen, eds. (Humana Press, 2011), Stem Cell Biology and Regenerative Medicine, pp. 483–498. 19

[43] J. F. Wager, "Applied physics. Transparent electronics." Science **300**, 1245–1246 (2003). 19

[44] Y. Yang, S. Jeong, L. Hu, H. Wu, S. W. Lee, and Y. Cui, "Transparent lithium-ion batteries." Proceedings of the National Academy of Sciences of the United States of America **108**, 13013–8 (2011). 19, 20

[45] L. Xiao, Z. Chen, C. Feng, L. Liu, Z.-Q. Bai, Y. Wang, L. Qian, Y. Zhang, Q. Li, K. Jiang, and S. Fan, "Flexible, stretchable, transparent carbon nanotube thin film loudspeakers." Nano letters **8**, 4539–45 (2008). 19, 20

[46] T. S. Kim, J. S. Park, K. S. Son, J. S. Jung, K.-H. Lee, W. J. Maeng, H.-S. Kim, J.-Y. Kwon, B. Koo, and S. Lee, "Transparent AMOLED display driven by hafnium-indium-zinc oxide thin film transistor array," Curr. Appl. Phys. **11**, 1253–1256 (2011). 20

[47] Y.-H. Cheng and G.-D. J. Su, "Waveguide display using polymer-dispersed liquid crystal," in "Proc. SPIE 8114, Liquid Crystals XV," , vol. 8114 (2011), vol. 8114, pp. 811414–1 – 811414–18. 20

[48] L. Eisen, M. Meyklyar, M. Golub, A. A. Friesem, I. Gurwich, and V. Weiss, "Planar configuration for image projection." Appl. Opt. **45**, 4005–11 (2006). 20, 21

[49] Z. Yan, W. Li, Y. Zhou, M. Kang, and Z. Zheng, "Virtual display design using waveguide hologram in conical mounting configuration," Optical Engineering **50**, 094001 (2011). 20

[50] J. Verdeyen, *Laser Engineering* (Prentice Hall, 2000), 3rd ed. 22, 37

[51] S. Johnson and J. Joannopoulos, "Block-iterative frequency-domain methods for Maxwell's equations in a planewave basis," Optics Express **8**, 173–190 (2001). 25, 27

[52] M. Qiu, "Effective index method for heterostructure-slab-waveguide-based two-dimensional photonic crystals," Applied Physics Letters **81**, 1163 (2002). 27

[53] M. G. Moharam, E. B. Grann, D. A. Pommet, and T. K. Gaylord, "Formulation for stable and efficient implementation of the rigorous coupled-wave analysis of binary gratings," J. Opt. Soc. Am. A **12**, 1068–1076 (1995). 27, 74

[54] A. Taflove and S. C. Hagness, *Computational Electrodynamics: The Finite-Difference Time-Domain Method* (Artech House, 2005). 28

[55] A. F. Oskooi, D. Roundy, M. Ibanescu, P. Bermel, J. D. Joannopoulos, and S. G. Johnson, "MEEP: A flexible free-software package for electromagnetic simulations by the FDTD method," Computer Physics Communications **181**, 687–702 (2010). 28

[56] a. J. Leadbetter, R. M. Richardson, and C. N. Colling, "The Structure of a Number of Nematogens," Le Journal de Physique Colloques **36**, C1–37–C1–43 (1975). 29

[57] D. W. Berreman, "Solid surface shape and the alignment of an adjacent nematic liquid crystal," Physical Review Letters **28**, 1683–1686 (1972). 31

[58] D. C. Flanders, D. C. Shaver, and H. I. Smith, "Alignment of liquid crystals using submicrometer periodicity gratings," Applied Physics Letters **32**, 597–598 (1978). 31

[59] W. Schenck, D.-H. Ko, and E. Samulski, "Liquid crystal alignment on polymer line gratings," J. Appl. Phys. **109**, 064301 (2011). 31

[60] Y. Yi, M. Nakata, A. R. Martin, and N. A. Clark, "Alignment of liquid crystals by topographically patterned polymer films prepared by nanoimprint lithography," Applied Physics Letters **90**, 163510+ (2007). 31

[61] C. H. Chiu, H. L. Kuo, P. C. Chen, C. H. Wen, Y. C. Liu, and H. M. P. Chen, "Nanoimprinting-lithography-induced self-aligned liquid crystals for novel multifunctional optical films," Applied Physics Letters **88**, 073509+ (2006). 31

[62] H. Jansen, M. de Boer, R. Legtenberg, and M. Elwenspoek, "The black silicon method: a universal method for determining the parameter setting of a fluorine-based reactive ion etcher in deep silicon trench etching with profile control," Journal of Micromechanics and Microengineering **5**, 115–120 (1995). 32

[63] J. Goodman, *Introduction to Fourier Optics* (Prentice Hall, 2005), 3rd ed. 32, 33

[64] E. B. Priestley, P. J. Wojtowicz, and P. Sheng, *Introduction to liquid crystals* (Plenum press, 1974), 1st ed. 33

[65] G. Mertens, "PhD thesis Anwendung von Flüssigkristallen für abstimmbare photonische Kristalle," Ph.D. thesis, Universität Paderborn (2004). 34

[66] J. Li, C.-H. Wen, S. Gauza, R. Lu, and S.-T. Wu, "Refractive Indices of Liquid Crystals for Display Applications," Journal of Display Technology **1**, 51–61 (2005). 34

[67] Exciton, Ohio, USA, "Pyrromethene 597 datasheet," http://www.exciton.com/pdfs/p597.pdf. Accessed October 31th, 2012. 37

[68] E. Yariv, S. Schultheiss, T. Saraidarov, and R. Reisfeld, "Efficiency and photostability of dye-doped solid-state lasers in different hosts," Optical Materials **16**, 29–38 (2001). 37

[69] S. r. Balslev, "Polymer dye lasers," Ph.D. thesis, DTU Nanotech (2006). 37

[70] J. Bañuelos Prieto, F. López Arbeloa, V. Martínez Martínez, T. Arbeloa López, and I. López Arbeloa, "Photophysical Properties of the Pyrromethene 597 Dye:Â Solvent Effect," The Journal of Physical Chemistry A **108**, 5503–5508 (2004). 37, 86

[71] A. S. for Testing and M. (ASTM), "Terrestrial Reference Spectra for Photovoltaic Performance Evaluation," \url{http://rredc.nrel.gov/solar/spectra/am1.5} (2011). 38

[72] F. KASTEN and A. T. YOUNG, "Revised optical air-mass tables and approximation formula," Appl. Opt. **28**, 4735–4738 (1989). 38

[73] A. B. Meinel and M. P. Meinel, *Applied Solar Energy* (Addison Wesley Publishing Co., 1976). 39

[74] R. Foster, M. Ghassemi, and A. Cota, *Solar energy: renewable energy and the environment*, Energy and the environment (CRC Press, 2009). 39

[75] L. J. Guo, "Recent progress in nanoimprint technology and its applications," J. Phys. D: Appl. Phys. **37**, R123–R141 (2004). 44

[76] S. Keller, G. Blagoi, M. Lillemose, D. Haefliger, and A. Boisen, "Processing of thin SU-8 films," Journal of Micromechanics and Microengineering **18**, 125020 (10pp) (2008). 44

[77] K.-h. Haas and H. Wolter, "Synthesis , properties and applications of inorganic â€" organic copolymers," Current Opinion in Solid State and Materials Science **4**, 571–580 (2000). 44

[78] L. G. Brown, "A Survey of Image Registration," ACM Computing Surveys **24**, 325–376 (1992). 54

[79] R. Maurer, F. Schneider, C. Vogt, M. Schinhaerl, P. Sperber, and R. Rascher, "Physical marker based stitching process of circular and non-circular interferograms," Proc. of SPIE **8083**, 80830Q (2011). 54

[80] J. P. Lewis, "Fast Normalized Cross-Correlation," http://www.idiom.com/~zilla/Papers/nvisionInterface/nip.html. Accessed October 4th, 2012. 54

[81] I. The MathWorks, "Matlab documentation, normxcorr2 function," . 54

[82] S.-J. Liu and C.-T. Liao, "Fast fabrication of nano-structured anti-reflection layers for enhancement of solar cells performance using plasma sputtering and infrared assisted roller embossing techniques." Optics express **20**, 5143–50 (2012). 58

[83] Rosenblatt, Sharon, and Friesem, "Resonant grating waveguide structures," IEEE Journal of Quantum Electronics **33**, 2038–2059 (1997). 59

[84] M. J. Adams, *An Introduction to Optical Waveguides* (Wiley, New York, 1981). 61

[85] H. D. Tholl, C. G. Stojanoff, R. Kubiza, and G. Willbold-Lohr, "Design optimization and manufacturing of holographic windows for daylighting applications in buildings," in "Proceedings of SPIE," , vol. 2017 (1993), vol. 2017, pp. 35–45. 71

[86] C. L. Robbins, *Daylighting: Design and Analysis* (Van Nostrand Reinhold, 1986). 71

[87] P. Licinio, M. Lerotic, and M. S. S. Dantas, "Diffraction by disordered gratings and the Debye-Waller effect," American Journal of Physics **67**, 1013–1016 (1999). 71

[88] J. M. Rico-García and L. M. Sanchez-Brea, "Binary gratings with random heights," Appl. Opt. **48**, 3062–3069 (2009). 71

[89] A. Oskooi, P. A. Favuzzi, Y. Tanaka, H. Shigeta, Y. Kawakami, and S. Noda, "Partially disordered photonic-crystal thin films for enhanced and robust photovoltaics," Applied Physics Letters **100**, 181110–181114 (2012). 71

[90] P. Lalanne and G. M. Morris, "Highly improved convergence of the coupled-wave method for TM polarization," J. Opt. Soc. Am. A **13**, 779–784 (1996). 74

[91] C. Peroz, V. Chauveau, E. Barthel, and E. Sø ndergård, "Nanoimprint Lithography on Silica Sol-Gels: A Simple Route to Sequential Patterning," Adv. Mater. **21**, 555–558 (2009). 75

[92] A. Letailleur, J. Teisseire, N. Chemin, E. Barthel, and E. Sø ndergård, "Chemorheology of Solâ^'Gel Silica for the Patterning of High Aspect Ratio Structures by Nanoimprint," Chem. Mater. **22**, 3143–3151 (2010). 75

[93] H. Schmid and B. Michel, "Siloxane Polymers for High-Resolution, High-Accuracy Soft Lithography," Macromolecules **33**, 3042–3049 (2000). 75

[94] C. Peroz, C. Heitz, E. Barthel, E. Sø ndergård, and V. Goletto, "Glass nanostructures fabricated by soft thermal nanoimprint," J. Vac. Sci. Technol. B **25**, L27 –L30 (2007). 75, 76, 132

[95] M. B. Mikkelsen, A. A. Letailleur, E. Sø ndergård, E. Barthel, J. Teisseire, R. Marie, and A. Kristensen, "All-silica nanofluidic devices for DNA-analysis fabricated by imprint of sol-gel silica with silicon stamp," Lab on a Chip **12**, 262–267 (2012). 76, 132

[96] C. Gourgon, A. K. Ferchichi, D. Pietroy, T. Haatainen, and J. Tesseire, "Scatterometry analysis of sequentially imprinted patterns: Influence of thermal parameters," Microelectron. Eng. **98**, 270–274 (2012). 77

[97] M. G. Figueiro and M. S. Rea, "Lack of short-wavelength light during the school day delays dim light melatonin onset (DLMO) in middle school students," Neuroendocrinol. Lett. **31**, 92–96 (2010). 80

[98] L. T. Sharpe, A. Stockman, W. Jagla, and H. Jägle, "A luminous efficiency function, VD65* (λ), for daylight adaptation: A correction," Color Res. Appl. **36**, 42–46 (2011). 80

[99] T. Tamir and S. T. Peng, "Analysis and design of grating couplers," Appl. Phys. **14**, 235–254 (1977). 99

[100] J. P. Lagerwall and G. Scalia, "A new era for liquid crystal research: Applications of liquid crystals in soft matter nano-, bio- and microtechnology," Curr. Appl. Phys. **12**, 1387–1412 (2012). 102

[101] K. Miyoshi, S. Yamada, and S. Miyahara, "Conoscopic study of liquid crystal after application and removal of the external electric field." Jpn. J. Appl. Phys. **22**, 1754–1765 (1983). 105

[102] Y. Lin, S. Feng, and T. Chen, "Temperature effect on threshold voltage and optical property of twisted nematic liquid crystal with applied different voltages," Optik - International Journal for Light and Electron Optics **121**, 1693–1697 (2010). 106

[103] S. Klinkhammer, N. Heussner, K. Huska, T. Bocksrocker, F. Geislhöringer, C. Vannahme, T. Mappes, and U. Lemmer, "Voltage-controlled tuning of an organic semiconductor distributed feedback laser using liquid crystals," Applied Physics Letters **99**, 023307 (2011). 107

[104] K. Kato, T. Hisaki, and M. Date, "In-Plane Operation of Alignment-Controlled Holographic Polymer-Dispersed Liquid Crystal," Jpn. J. Appl. Phys. **38**, 1466–1469 (1999). 107

[105] A. K. Pitilakis, D. C. Zografopoulos, and E. E. Kriezis, "In-Line Polarization Controller Based on Liquid-Crystal Photonic Crystal Fibers," J. Lightwave Tech. **29**, 2560–2569 (2011). 107

[106] G. Abbatec and G. C. Righini, "Electro-optical switch based on a Bragg grating in a liquid crystal," Proc. of SPIE **4829**, 522–524 (2003). 109

[107] E. Feigenbaum, K. Diest, and H. a. Atwater, "Unity-order index change in transparent conducting oxides at visible frequencies." Nano letters **10**, 2111–6 (2010). 109

[108] T. Motohiro and Y. Taga, "Sputter-deposited SiOx films for liquid crystal alignment," Thin Solid Films **185**, 137–144 (1990). 111

[109] T. Kagajyo, K. Fujibayashi, T. Shimamura, H. Okada, and H. Onnagawa, "Alignment of Nematic Liquid Crystal Molecules Using Nanometer-Sized Ultrafine Patterns By Electron Beam Exposure Method," Japanese Journal of Applied Physics **44**, 578–581 (2005). 111

[110] E. Miyai, K. Sakai, T. Okano, W. Kunishi, D. Ohnishi, and S. Noda, "Lasers producing tailored beams," Nature **441**, 946 (2006). 111

[111] M. Aljada, K. E. Alameh, Y.-T. Lee, and I.-S. Chung, "High-speed (2.5 Gbps) reconfigurable inter-chip optical interconnects using opto-VLSI processors," Opt. Express **14** (2006). 112

[112] D. D. John, M. J. R. Heck, J. F. Bauters, R. Moreira, J. S. Barton, J. E. Bowers, and D. J. Blumenthal, "Multilayer Platform for Ultra-Low-Loss Waveguide Applications," IEEE Photonics Technology Letters **24**, 876–878 (2012). 112

[113] S. Dochow, C. Krafft, U. Neugebauer, T. Bocklitz, T. Henkel, G. Mayer, J. Albert, and J. Popp, "Tumour cell identification by means of Raman spectroscopy in combination with optical traps and microfluidic environments." Lab on a chip **11**, 1484–90 (2011). 112

[114] B. Landenberger, H. Höfemann, S. Wadle, and A. Rohrbach, "Microfluidic sorting of arbitrary cells with dynamic optical tweezers." Lab on a chip **12**, 3177–83 (2012). 112

[115] A. R. Faustov, M. R. Webb, and D. R. Walt, "Note: Toward multiple addressable optical trapping." Rev. Sci. Instrum. **81**, 026109 (2010). 112

A Appendix

A.1 List of publications related to PhD thesis

Journal papers

- **T. Buß**, C. L.C. Smith, and A. Kristensen, "Electrically modulated transparent optical grating projection display," submitted.

- **T. Buß**, J. Teisseire, S. Mazoyer, C. L.C. Smith, M. B. Mikkelsen, A. Kristensen, and E. Søndergård, "Controlled angular redirection of light via nanoimprinted disordered gratings," Applied Optics, Accepted for publication.

- **T. Buß**, C. L. C. Smith, M. Brøkner Christiansen, R. Marie, and A. Kristensen, "Sub-wavelength surface gratings for light redirection in transparent substrates," Applied Physics Letters 101, 043109 (2012).

Proceedings

- **T. Buß**, M. B. Christiansen, C. L. C. Smith, and A. Kristensen, "Liquid crystal tunable photonic crystal dye laser," in Conference on Lasers and Electro-Optics (CLEO) (2010).

Conference presentations

- A. Kristensen, **T. Buß**, M. B. Christiansen, C. L. C. Smith, and N. A. Mortensen, "Optofluidic tuning of photonic crystal lasers," Invited talk at SPIE Photononics West 2012 (2012).

- **T. Buß**, C. L. C. Smith, and A. Kristensen, "A transparent Projection Display based on Photonic Crystals," oral presentation at the 1st EOS Topical Meeting on Micro- and Nano-Optoelectronic Systems (2011).

- **T. Buß**, C. L. C. Smith, M. B. Christiansen, R. Marie, and A. Kristensen, "Grating couplers for solar harvesting in window panes," poster presentation at the 37th International Conference on Micro and Nano Engineering (MNE) (2011).

A.2 List of additional publications

Journal papers

- M. M. Jørgensen, S. R. Petersen, M. B. Christiansen, **T. Buß**, C. L. C. Smith, and A. Kristensen, "Influence of index contrast in 2D photonic crystal lasers," Applied Physics Letters 96, 231115 (2010).

- C. L. C. Smith, J. U. Lind, C. H. Nielsen, M. B. Christiansen, **T. Buß**, N. B. Larsen, and A. Kristensen, "Enhanced transduction of photonic crystal dye lasers for gas sensing via swelling polymer film," Opt. Lett. 36, 1392?1394 (2011).

- M. B. Christiansen, **T. Buß**, C. L. C. Smith, S. R. Petersen, M. M. Jørgensen, and A. Kristensen, "Single mode dye-doped polymer photonic crystal lasers," Journal of Micromechanics and Microengineering 20, 115025 (2010).

Proceedings

- C. L. C. Smith, J. U. Lind, C. H. Nielsen, M. B. Christiansen, **T. Buß**, N. B. Larsen, and A. Kristensen, "Selective gas sensing for photonic crystal lasers," in 2010 Conference on Lasers and Electro-Optics (CLEO) (2011).

- M. B. Christiansen, C. L. C. Smith, **T. Buß**, S. Xiao, N. A. Mortensen, and A. Kristensen, "Nanoimprinted polymer photonic crystal dye lasers," in Micro-Optics 2010, H. Thienpont, P. V. Daele, J. Mohr, and H. Zappe, eds. (SPIE, 2010), Vol. 7716, p. 77160Q.

- C. L. C. Smith, M. B. Christiansen, **T. Buß**, and A. Kristensen, "Enhanced transduction of polymer photonic crystal band-edge lasers via additional layer deposition," in Conference on Lasers and Electro-Optics (CLEO) (2010).

- M. B. Christiansen, **T. Buß**, C. L. C. Smith, and A. Kristensen, "Improved emission properties of polymer photonic crystal lasers by introducing a phase-shift," in Conference on Lasers and Electro-Optics (CLEO) (2010).

Conference presentations

- **T. Buß**, M. B. Mikkelsen, D. A. Mendels, and A. Kristensen, "Investigation of Cross-talk in Nanoimprint Lithography," oral presentation at the 10th International Conference on Nanoimprint and Nanoprint Technology (NNT) (2011).

- D. A. Mendels, F. Mendels, M. Mikkelsen, **T. Buß**, and A. Kristensen, "Mechanical proximity correction using the NIL Simulation Suite," oral presentation at the 10th International Conference on Nanoimprint and Nanoprint Technology (NNT) (2010).

- M. B. Christiansen, M. M. Jørgensen, S. R. Petersen, C. L. C. Smith, **T. Buß**, and A. Kristensen, "Properties and reproducibility of photonic crystal dye lasers," at SPIE Optics+Photonics (SPIE, 2010).

A.3 Micro- and nanofabrication recipes

A.3.1 Materials and chemical suppliers

Type	*Name*	*Details*	*Supplier*
Wafer	Borofloat	Standard glass wafer	Jinsol, Seoul, Korea
Wafer	Fused silica	UV-transparent imprint stamps	Jinsol, Seoul, Korea
Wafer	Silicon	n-doped, Cz grown, 1-20 Ohm-cm	Okmetic, Vantaa, Finland
Developer	MF-322	Used for aluminum etch	Dow / Shipley Company, USA
Adhesion promoter	HMDS	Hexamethyldisilazan, $C_6H_{19}NSi_2$	?
Resist	ZEP520A	e-beam resist	Zeon Corporation, Tokyo, Japan
Developer	ZED-N50	Developer for ZEP resist	Zeon Corporation, Tokyo, Japan
Developer	PGMEA	Propylene glycol monomethyl ether acetate	?
Resist	AZ5214B	UV photoresist	AZ Electronic Materials, Tokyo, Japan
Resist	SU-8	UV and e-beam resist	Microchem, USA
Resist	Ormocore	UV photoresist	Micro resist technology, Berlin, Germany
Resist	PMMA	Polymethylmethacrylat, $[C_5H_8O_2]n$	?
Laser dye	Pyrromethene 597	$C_{30}H_{49}N_2BF_2$	Exciton, USA
Liquid crystal	5CB	4'-Pentyl- 4-biphenyl-carbonitrile	Sigma Aldrich, Germany

A.3.2 CNP stamp fabrication

Wafer selection
Jinsol fused silica, 10 cm diameter, 1 mm thickness

E-beam lithography

Process	*Machine*	*Parameters*	*Comment / Purpose*
Plasma cleaning	Plasma asher	70 sccm N_2, 70 sccm O_2, 1000 W, 30 min	Wafer cleaning
E-beam resist spinning	III-V spinner	5.5% ZEP520A, 2000 rpm, 500 rpm/s, 60 s	Thickness: 160 nm
Pre-exposure bake	III-V hotplate	5 min, 180 °C	Evaporate solvent
Aluminum deposition	Wordentec	15 nm thermal Al	Charge compensation layer
E-beam exposure	E-beam writer	180-240 µC/cm^2, 100 keV, 0.85 nA, 10 nm grid, Ap. 7	Gratings: 180 µC/cm^2, PhC: 240 µC/cm^2
Aluminum etch	Fumehood	50 s MF-322, 120 s DI water rinse, N_2 blow dry	Remove charge compensation layer
E-beam development	Fumehood	120 s N50, 60 s IPA rinse, N_2 blow dry	Develop e-beam pattern

Lift-off

Process	*Machine*	*Parameters*	*Comment / Purpose*
RIE descum	RIE2	MBCDSCUM, 4 s	Remove residual resist
Aluminum deposition	Wordentec	20 nm, 10 Å/s, e-beam evaporation	Etch mask
Lift-off	Ultrasonic bath	30 min in 1165 microposit remover	Exchange 1165 in between, keep sample wetted
Cleaning	Fumehood	30s IPA rinse, 30 s DI water rinse	
Drying	Single wafer dryer		

Nanostructures etch

Process	*Machine*	*Parameters*	*Comment / Purpose*
RIE descum	RIE2	MBCDSCUM, 30 s	Clean wafer
RIE SiO_2 etch	RIE2	MBC_SIO2, 3 min	Grating etch (120 nm)
Aluminum etch	Wet bench	H_2O:H_3PO_4 1:2 at 50 °C	Remove etch mask
DI-water rinse	Fumehood		
Drying	Single wafer dryer		

Shadow mask

Process	*Machine*	*Parameters*	*Comment / Purpose*
Preparation	HMDS oven	Recipe 4, 30 min	Adhesion promoter
Spinning photoresist	SSE spinner	1,5 µm AZ5214B, Recipe 4inch 1.5	baking step included
Exposure	KS Aligner	3.6 s, Constant Intensity 2	Mask "Waveguides"
Inversion bake	Hotplate	100 s, 120 °C	Crosslink exposed areas
Flood exposure	KS Aligner	30 s, Constant Intensity 2	Make exposed areas soluble
Development	AZ 351B/water (1/5) bath	60 s, manually moving carrier during development	Remove exposed areas
DI-water rinse	Water bath	3 min	
Drying	Spin dryer		
Reactive Ion Etch	RIE 2	MBC_SIO2, 3 min	100 nm etch around the laser windows
Chromium deposition	Wordentec	e-beam evaporation, 100 nm	Shadow mask
Lift-off	Wet bench	2 min in acetone with ultrasound	Rotation of wafer after 1 min
DI-water rinse	Water bath	5 min	
Drying	Single wafer dryer		

Anti-stiction coating

Process	*Machine*	*Parameters*	*Comment / Purpose*
Cleaning	7-Up bath	80 °C, 20 min	Sulfuric acid and ammonium peroxodisulfate
Cleaning	Wet bench	DI water rinse, 5 min	
Cleaning	MVD	plasma cleaning: 250W, 200 sccm, O_2, 5 min	Recipe "Stamp"
Molecular vapor deposition	MVD	FDTS coating: 4x (500 mTorr FDTS, 6 Torr H_2O, 15 minutes)	Recipe "Stamp"

A.3.3 Solar harvesting samples

Wafer selection
Jinsol Borofloat, 10 cm diameter, 0.5 mm thickness

Imprint substrate preparation

Process	*Machine*	*Parameters*	*Comment / Purpose*
Baking	Oven	250 °C, 24 hours	Dehydrate wafer
Spin Imprint resist	III/V Spinner	Ormocore: 4000 rpm, 500 rpm/s, 60s PMMA: 6000 rpm, 600 rpm/s, 60 s	Ormocore 20 wt% in mt-T 1050 thinner, thickness: 460 nm PMMA 75k 25 wt% in Anisole, thickness: 3 µm
Baking	Hotplate	Ormocore: 100 °C, 5 min PMMA: 150 °C, 10 min	Evaporate solvent Evaporate solvent

Nanoimprint

Process	*Machine*	*Parameters*	*Comment / Purpose*
Prepare imprint	Yellow room	Al foil, 0.5 mm graphite, substrate, stamp, 0.5 mm graphite, Al foil	Graphite sheets: homogenize pressure, Al foil: prevent contamination
Imprint	EVG NIL	Ormocore: 10 kN, 5 min, room temperature PMMA: 15 kN, 10 min, 190 °C	Fused silica stamp Skip to stamp separation
UV flood exposure	KS aligner	Flood exposure 30s, CI2	Exposure through stamp
Post exposure bake	Hotplate	90 °C, 3 min	Crosslinking
Stamp separation	Fumehood	Separation using a scalpel	PMMA: stop here
Development	Fumehood	Ormodev, 3 min	
Cleaning	Fumehood	IPA, 30 s	
Drying	Fumehood	N2 blow dry	

A.3.4 Daylighting samples

Fabrication of the daylighting samples was done at CEA-LETI and St. Gobain Recherche. For details about the process see ref.[94]

Silicon master fabrication (at CEA-LETI, Grenoble, France)

Process	*Parameters*	*Comment / Purpose*
Electron beam writing		Structure definition
Etching	350 nm	Etching structures into substrate

PDMS stamp fabrication (using silicon master)

Process	*Parameters*	*Comment / Purpose*
PDMS casting, nanostructures	h-PDMS (ABCR, Germany), pour thin layer on master	PDMS casted from silicon master
Degasing	Vacuum, 1 hour	Remove air bubbles
Baking	60 °C, 15 min	Curing PDMS
PDMS casting, support	PDMS (Sylgard 184)	Flexible support for h-PDMS
Baking	60 °C, 2 hours	Curing PDMS

Nanoimprint (using PDMS stamp)

Process	*Parameters*	*Comment / Purpose*
Mixing sol-gel precursors	3.6 g methyltriethoxysilane (MTES, 0.1 mol), 5.1 g HCl (pH = 2.5)	Mixing sol-gel precursors
Spin coating	2500 rpm, 30 s	Thickness: 800 nm
Imprinting	50 N, 80 °C, 60 min	PDMS stamp (area: 12 cm^2)
Demolding	Room temperature	
Annealing	500 °C, oxygen atmosphere, 4 h	Optional, for details see[95]

A.3.5 Dyelaser samples

Wafer selection
Silicon, n-doped, 4.4 µm wet oxide, 10 cm diameter, 0.35 um thickness

E-beam lithography

Process	*Machine*	*Parameters*	*Comment / Purpose*
Plasma cleaning	Plasma asher	70 sccm N_2, 70 sccm O_2, 1000 W, 30 min	Wafer cleaning
E-beam resist spinning	III-V spinner	5.5% ZEP520A, 2000 rpm, 500 rpm/s, 60 s	Thickness: 160 nm
Pre-exposure bake	III-V hotplate	5 min, 180 °C	Evaporate solvent
Aluminum deposition	Wordentec	15 nm thermal Al	Charge compensation layer
E-beam exposure	E-beam writer	220 µC/cm^2, 100 keV, 2 nA, 6 nm grid, Ap. 7	Photonic crystal pattern
Aluminum etch	Fumehood	50 s MF-322, 120 s DI water rinse, N_2 blow dry	Remove charge compensation layer
E-beam development	Fumehood	120 s N50, 60 s IPA rinse, N_2 blow dry	Develop e-beam pattern

Lift-off

Process	*Machine*	*Parameters*	*Comment / Purpose*
RIE descum	RIE2	MBCDSCUM, 4 s	Remove residual resist
Aluminum deposition	Wordentec	30 nm, 10 Å/s, e-beam evaporation	Etch mask
Lift-off	Ultrasonic bath	30 min in 1165 microposit remover	Exchange 1165 in between, keep sample wetted
Cleaning	Fumehood	30s IPA rinse, 30 s DI water rinse	
Drying	Single wafer dryer		

Nanostructures etch

Process	*Machine*	*Parameters*	*Comment / Purpose*
RIE descum RIE SiO_2 etch	RIE2 RIE2	MBCDSCUM, 30 s MBC_SIO2, 5 min	Clean wafer Grating etch (140 nm)
Aluminum etch	Wet bench	H_2O:H_3PO_4 1:2 at 50 °C	Remove etch mask
DI-water rinse	Fumehood		
Drying	Single wafer dryer		

SU-8 spacer

Process	*Machine*	*Parameters*	*Comment / Purpose*
Baking	oven	250 °C, 4 hours	Deydrate wafer
Spin coating	III/V spinner	SU-8, 3000 rpm, 300 rpm/s, 60 s	SU-8 33 wt% in cyclopentanone , thickness: 326 nm
Baking	SU-8 hotplate	65 °C, ramp 4 min, hold 1 min, 95 °C, ramp 4 min, hold 2 min	Evaporate solvent
E-beam exposure	E-beam writer	13 µC/cm^2, 2 nA, 20 nm grid, Ap. 6	
Baking	SU-8 hotplate	65 °C, ramp 4 min, hold 1 min, 95 °C, ramp 4 min, hold 1 min	Crosslink exposed areas
Development	SU-8 developer (PGMEA)	2 min rough, 2 min fine	Remove unexposed areas
Cleaning	fumehood	IPA rinse, 30 s	
Drying	Single wafer dryer		

A.3.6 Projection display samples

Bottom wafer fabrication
Jinsol Borofloat, 10 cm diameter, 0.5 mm thickness

Imprint substrate preparation

Process	*Machine*	*Parameters*	*Comment / Purpose*
Baking	Oven	250 °C, 24 hours	Dehydrate wafer
Spin Imprint resist	III/V Spinner	SU-8, 5000 rpm, 500 rpm/s, 60 s	SU-8 43 wt% in cyclopentanone, 610 nm
Baking	SU-8 hotplate	90 °C, 2 min	Evaporate solvent

Nanoimprint

Process	*Machine*	*Parameters*	*Comment / Purpose*
Prepare imprint	Yellow room	Al foil, 0.5 mm graphite, substrate, stamp, 0.5 mm graphite, Al foil	Graphite sheets: homogenize pressure, Al foil: prevent contamination
Imprint	EVG NIL	Ormocore: 10 kN, 10 min, room temperature	Stamp with gratings/PhC (protrusions) and waveguides (Cr mask)
UV flood exposure	KS aligner	Flood exposure 4x30s, 15 s pause	Exposure through stamp
Post exposure bake	Hotplate	90 °C, 3 min	Crosslinking
Stamp separation	Fumehood	Separation using a scalpel	
Development	SU-8 developer	PGMEA, 2 min rough, 2 min fine	remove non-crosslinked residual resist
Cleaning	Fumehood	IPA, 30 s	
Drying	Single wafer dryer	N2 blow dry	

Electrodes

Process	*Machine*	*Parameters*	*Comment / Purpose*
Preparation	HMDS oven	Recipe 4, 30 min	Adhesion promoter
Spin coating	SSE spinner	1.5 µm AZ5214B, recipe 4inch 1.5_more resist	includes baking
UV exposure	KS aligner	3.6 s, Constant intensity 2	Mask "ITO electrodes"
Inversion bake	Hotplate	100 s, 120 °C	Crosslink exposed areas
Flood exposure	KS Aligner	30 s, Constant Intensity 2	Make exposed areas soluble
Development	AZ 351B/water (1/5) bath	60 s, manually moving carrier during development	Remove exposed areas
DI-water rinse	Water bath	3 min	
Drying	Spin dryer		
ITO deposition	Lesker sputter system	100 W, 6 mTorr, 1800 s	Thickness: 45 nm
Lift-off	Fumehood	5 min in acetone with ultrasound	
DI-water rinse	Water bath	5 min	
Drying	Single wafer dryer		
Dicing	Dicing saw	blade height 0.1 mm, speed 1.5 mm/s	20 x 15 mm chips

Lid wafer fabrication

Jinsol Borofloat, 10 cm diameter, 0.5 mm thickness

Al spacers and ITO coating

Process	*Machine*	*Parameters*	*Comment / Purpose*
Masking		Cover wafer with blue tape, cut spacers with scalpel	Use laminated print as template
Al deposition	Wordentec	e-beam evaporation, 600 nm	Permission from Danchip required. Monitor pressure during process, deposit in two steps
Tape removal		peel-off blue tape	
ITO deposition	Lesker sputter system	100 W, 6 mTorr, 1800 s	Thickness: 45 nm
Dicing	Dicing saw	blade height 0.1 mm, speed 1.5 mm/s	10 x 8 mm chips

Assembly of bottom and lid

Process	*Parameters*	*Comment / Purpose*
Lid placement	Push lid onto substrate, as much force as manually possible	Use hot-glue stick
Lid glueing	4 dots of epoxy glue	Make sure light path and electrodes not covered
Curing	Hotplate, 4 hours, 50 °C	Temperature accelerates curing
Liquid crystal filling	Apply single drop of liquid crystal at open edge, ramp temperature down from 60 °C to 25 °C over 4 hours	Formation of ordered LC pattern

A.3.7 Machine recipes

RIE 2				
mbc_sio2	RF-Power	60 W		+/- 25 %
	Gas 1	CF4	14 sccm	+/- 20 %
	Gas 2	CHF3	26 sccm	+/- 20 %
	Pressure	100 mT		+/- 25%
	Pump down	30 s		
	Gas stabilization	30 s		
	Process			
	Pump out	30 s		
mbc_descum	RF-Power	30 W		+/- 25 %
	Gas 1	O2	20 sccm	+/- 25 %
	Gas 2	N2	99 sccm	+/- 25 %
	APC Mode 74 Deg.			
	Pump down	20 s		
	Gas stabilization	60 s		
	Process			
	Pump out	30 s		

A.4 Optical measurement setup

A.4.1 Labview program flowchart

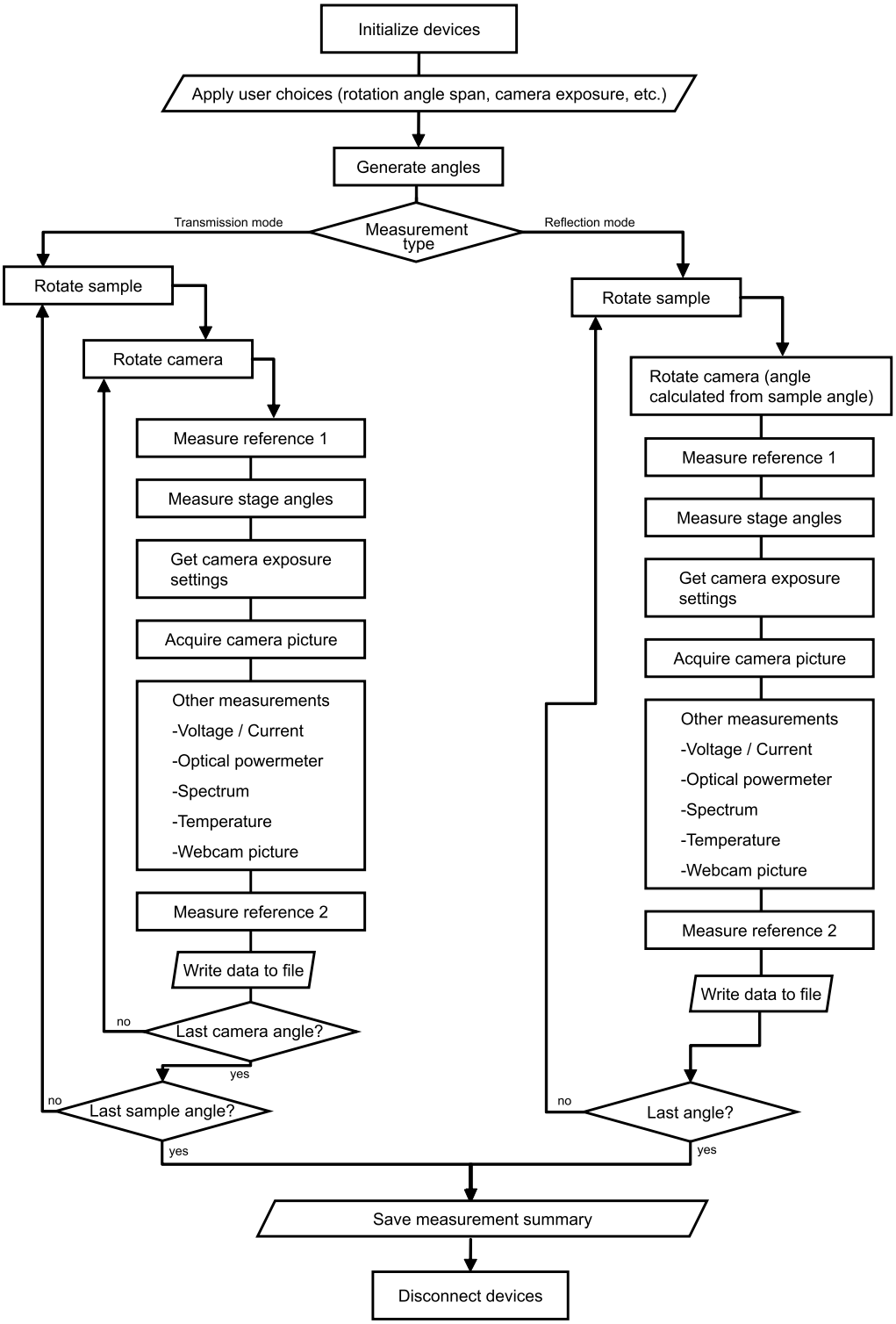

A.4.2 Matlab post-processing flowchart

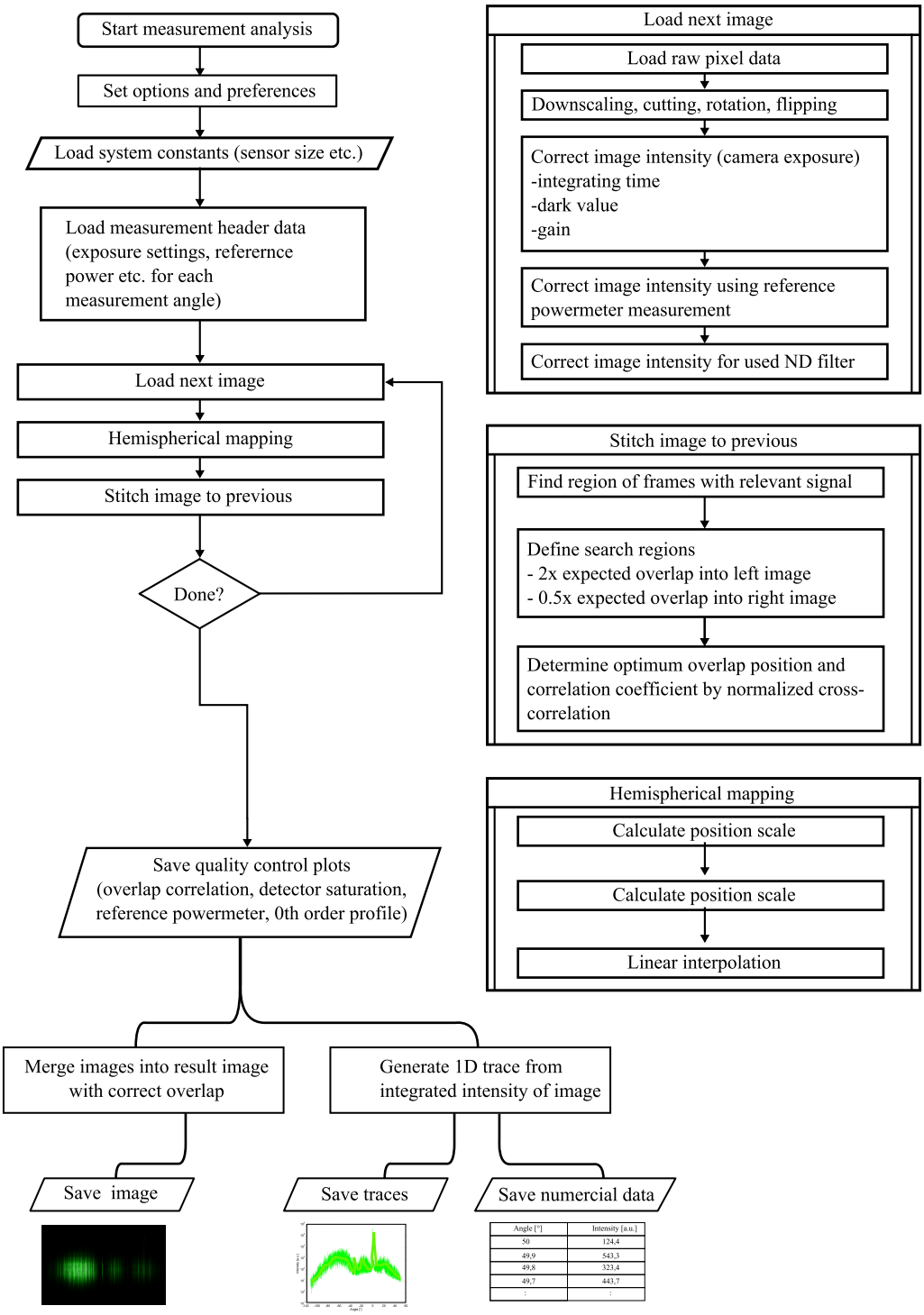

A.4.3 Projection display setup details

Figure A.1 shows a photograph of the required electronics equipment used to characterize the projection display samples.

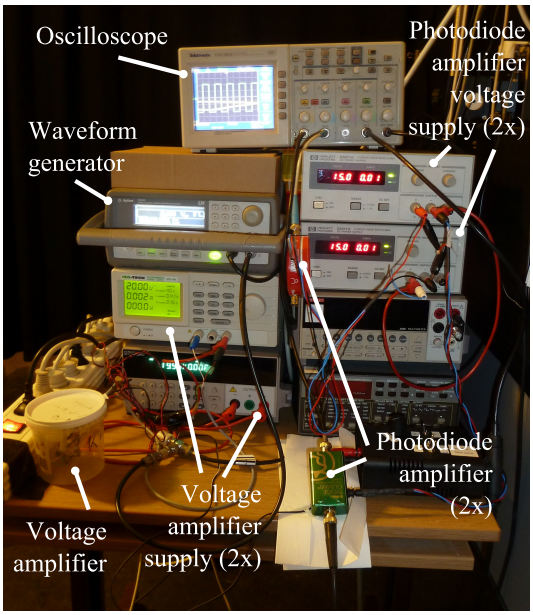

Figure A.1: Electronics equipment used for characterization of the LC display samples.

Figure A.2 shows a schematic of the transimpedance amplifier used to measure the photo current of the photo diodes.

A.5 Photographs

Figure A.3 displays the transparency of complex micro- and nanoscale structures, consisting of waveguides and photonic crystals defined by UV-NIL in a 600 nm thin film of Ormocore and 60 nm thin ITO electrodes.

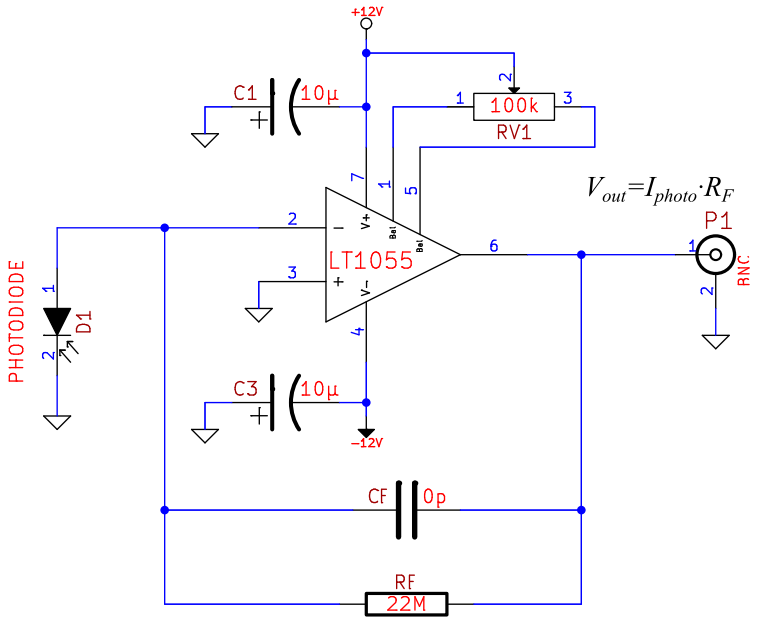

Figure A.2: Electronics equipment used for characterization of the LC display samples.

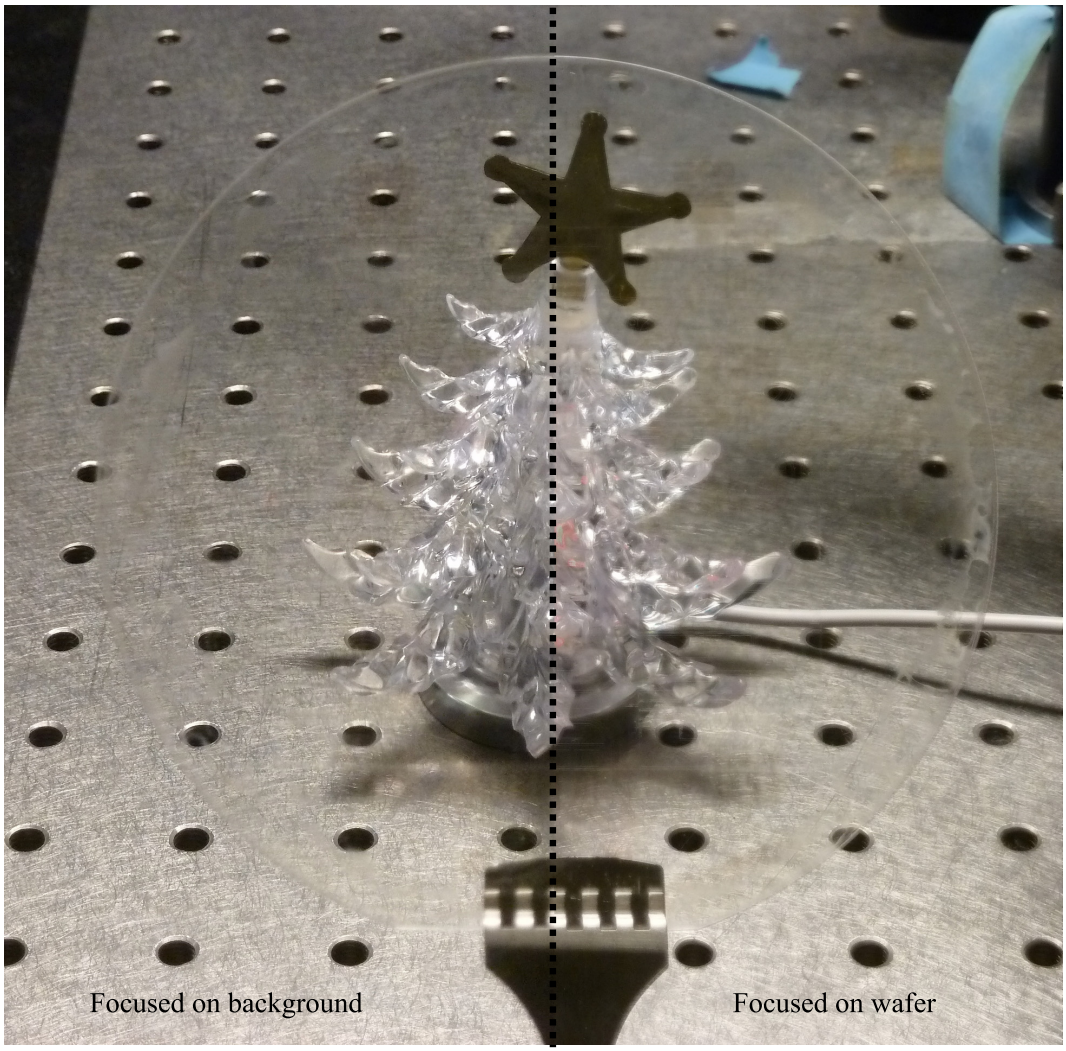

Figure A.3: Photograph of a glass wafer ITO electrodes and photonic crystals and waveguides defined by UV-NIL in a 600 nm thin film of Ormocore. The image is composed from two individual photographs, the left half focused on the background and the right half focused on the wafer in the foreground. A high degree of transparency is preserved.